Design and application of high performance Acousto-Optic Tunable Filters

Stefano Valle

Submitted in fulfilment of the requirements for the degree of
Doctor of Engineering

School of Engineering

College of Science and Engineering
University of Glasgow

November 2016

Abstract

The design and application of high performance Acousto-Optic Tunable Filters (AOTFs) is the topic of this thesis. The most common material commercially used to build AOTFs is Tellurium Dioxide because of its extended wavelength range from 380 nm up 4.5 μm, a good acousto-optic figure of merit, and the availability in crystal of large dimension with good optical quality. The performance of an AOTF can be summarized by passband versus wavelength, RF power to achieve peak diffraction efficiency and tuning range. One of the most relevant parameters which limits AOTF performance is the RF power versus diffraction efficiency, which increases with 2. A practical limitation has been imposed to 50mW /mm2 , above these level thermal gradient affects the performance. This level is easy reached for conventional AOTF for wavelength above 2.5 μm. The reduction of RF power requirement is achieved by means of acoustic resonant cavities. The theoretical development and subsequent design of the first resonant AOTF developed inside Gooch and Housego is carried out, and the experimental results are in good agreement with the predicted performances. The results obtained from the experience with resonant AOTFs lead to extending the wavelength range from 180 nm up to 10 μm using different acousto-optic materials with limited performance with conventional configuration. Crystal quartz is investigated to extend the wavelength range down to 180 nm, this material is well known in acousto-optic applications. The resonant configuration is particularly suitable for this crystal since the advantage factor is particularly high thanks to the low acoustic attenuation. The experimental results show good agreement with the predicted performances, leading to a large aperture AOTF operating between 180 nm and 380 nm with RF power for peak diffraction efficiency below 8 W. This is the first time that a resonant imaging AOTF made of crystal quartz is reported in literature, to the best of the authors knowledge. Calomel single crystal is investigated to realise an AOTF operating between 4.5 μm and 10 μm. Due to its physical properties which are incompatible with conventional manufacturing processes, different challenges (such as bonding the ultrasonic transducer) are solved by the author in order to build a high performance AOTF. Despite

the preliminary results showing promise, the acousto-optic properties of the material are limiting the achievable performance, at least for acousto-optic tunable filters, a fact that does not seem to have been widely appreciated , and which cannot solved by just pecialize the design. From the application point of view an optical spectrum analyser based on AOTF technology is investigated, where a dual polarization AOTF is developed in order to realize a spectrometer with a competitive price operating in the wavelength range between 2.5 μm and 4.5 μm. The effects of the acoustic attenuation on a large aperture AOTF is investigated theoretically and experimentally since the performance is affected in the UV range leading to non-ideal operating condition, and a solution is proposed to overcome this issue The results obtained will allow the design of high performance AOTFs in the industrial environment leading to a new types of devices with enhanced performance.

Dedicated to Maria Chiara
Miriam and Cecilia.

Table of Contents

List of Tables

List of Figures

Acknowledgements

The EngD has been a truly life-changing experience for me, and I managed to reach the end of it thanks to the support received from many people.

I would like to thank the EngD centre, which partially sponsored the research activities of the last four years through EPSRC (grant number EP/G037523/1), and Gooch and Housego ltd.(UK).

The many people met in Gooch and Housego made the EngD experience the most important of my life. I would like to thank my academic supervisor Dr. Nigel Johnson for the support and help given in theses years. I would like to express my sincere gratitude to my industrial supervisors: Dr. Chris Pannell and Jon Ward for the continuous support of my EngD study and related research, for their patience, motivation, and immense knowledge.Their guidance helped me in all the time of research and writing of this thesis.

I would like to thank Graham Glenn for the help and the training on the RF matching, which was a vital skill for my research. Many thanks go to: Dr. Ian Lindsay, Dr. Mark Farries, Gary Stevens, Laurent Kling, Mark English, Marlene Hendrick, Linda Bruce, Alison Low.

I would like to thanks my parents and my sister to be always available when I was in need.

A great thanks of gratitude goes to my wife, Maria Chiara, without her I would not have started and completed my EngD. The help and support received from her is incredible, and I will be always in debt. This thesis is also dedicated to my daughters, Miriam and Cecilia, who light the darkest day.

Chapter 1

Introduction

The study and development of Acousto-Optics (AO) devices started several decades ago and their prevalent application was in lasers systems to perform different operations such: Q-switching in laser, light modulation, mode locking, pulse picking and several other applications. It is possible to classify AO devices by the types of AO interaction, which are identified by the acoustic mode selected and by the characteristic of the material.

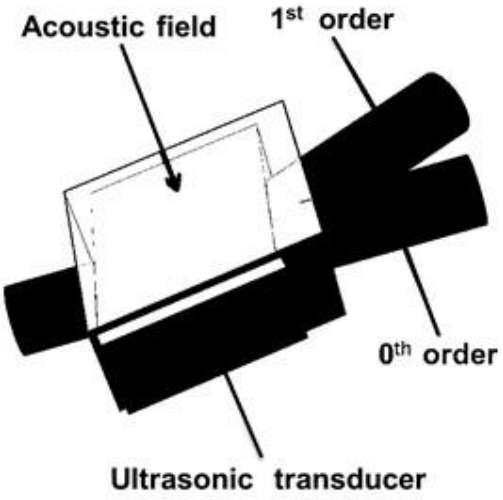

Figure 1.1: Acousto-Optic device.

Acousto-Optic devices are realized by bonding an ultrasonic transducer to an AO material, the former generates acoustic waves when an RF signal is applied. The ultrasonic transducer when excited with an RF signal will generate acoustic waves propagating inside the crystal generating a travelling grating.
The acoustic optic interaction could be studied by considering the strain generated

For short wavelengths below 380 nm, crystal quartz and KDP [3] may be used, both crystals have challenges which are required to be solved before being able to build AOTF. The crystal has small M_2 leading to elevated RF power versus diffraction efficiency. KDP crystals have a modest M_2 but physical properties requires development of special processes for polishing and bonding.

1.3 Acousto-Optic devices: Overview

There are several acousto-optic devices commercially available, which are used for different applications. A short list of the most common AO devices is reported below.

- **Acousto-optic modulators** (AOM) are used to control and modulate the intensity of light at high frequency. The modulation frequency is up to 70 MHz and can have a rise time as low as 4 ns.

- **Acousto-optic beam deflectors** allow an accurate spatial control of an optical beam, where the deflection angle is dependent to the RF frequency applied.

- An **acousto-optic frequency shifter** (AOFS) increase or reduce the frequency of the optical beam due to the Doppler shift. The sign of the frequency shift is determined by the phase matching condition Eq.1.1

- An **acousto-optic mode locker** is a modulator used inside the laser cavity to actively control the loss and induce a fixed-phase relationship between multiple longitudinal modes of the laser cavity.

- An **acousto-optic Q-switch** (AOQS) is placed inside a laser cavity to control the amount of light circulating inside the resonator. An AOQS in turned on diffracts light out of the optical beam path within the cavity, increasing losses and reducing the Q-factor in order to build up the population inversion in the gain medium. When the acousto-optic Q-switch is turned off, the losses within the cavity are reduced very quickly, increasing the Q-factor and allows rapid amplification to create a very high intensity, short pulse.

- An **acousto-optic tunable filter** (AOTF)where the RF drive frequency determine the center wavelength of the narrow passband changes. These devices have the capability of fast random access tunable filters

1.4 Design procedure and industrial process to develop AOTF

The AOTF prototype development was dictated by the hosting company which is Gooch & Housego Ltd. Where the manufacturing process is done on site. The first step is a feasibility study and optimization in order to determine the best performance achievable minimizing the crystal dimension. The feasibility study is carried over by different design routines developed by the author in Matlab and reported in the appendix, which gives the information required to design the AO cell and the predicted performances. The AO cell is processed in production after three technical drawings are prepared and the Bill Of Materials with the described process is prepared and approved by the different area manager. Job cards are prepared and added to the queue. The process is described in details in appendix D.

1.5 Motivation of the study on high performance AOTFs.

The performance of an AOTF could be defined as acoustic power required to achieve peak diffraction efficiency. One of the limitations is dictated by the availability of a tunable RF sources which is able to deliver power level above 50 W. Acoustic waves in the crystal are attenuated generating thermal gradient inside the AO material [6], affecting the performances and in some case damaging irreversibly the device.

High performance AOTFs can be built by careful design of the acousto-optic interaction, which is done by mathematical models introduced in design routines. Several design routines were prepared by the author to predict the AOTF performances and to compare the experimental results against the predicted performance.

The practical limitation applied on TeO_2 is 25 mW/mm^2 of RF power, above this the performance of the AOTF is affected and is difficult to predict with mathematical models. This limit is easily reached for wavelength above 2 μm in the case of imaging AOTF, in order to extend the range in the Infra-red (IR) up to edge of the transmission range, a special device was investigated working with acoustic resonant cavities (Chapter 5).

One of the reason to investigate the enhancement achieved by the acoustic resonant cavities, was the development of an AOTF working up to 10 μm well above the transmission range of TeO_2. In literature are reported different birefringent materials which can be use to realize AOTFs, such as Mercurous halide [7], single crystal tellurium [4]. Calomel single crystal was investigated in order to extend the operational wavelength

range of AOTFs up to 10 μm to develop an AOTF for a system under development in the MINERVA project FP-7 (Chapter 6), with some promising results.
Crystal Quartz is an AO material typically used in high optical power application such as the AO Q-switch, where the AO interaction is peciali by the longitudinal acoustic mode. This AO material can also be used for the slow shear interaction therefore an AOTF can be built filtering wavelengths in the UV range down to 180nm. In the literature, other AO materials have been reported that can be used in similar wavelength range, such as KDP, which has a better M_2 compared to Crystal Quartz. KDP crystal requires special process during the polishing and bonding processes due to its physical properties. Crystal Quartz was investigated to realise AOTF for UV applications, because all the processes involving the crystal quartz are well established in Gooch & Housego Ltd., in order to improve the performance an AOTF in resonant configuration has been designed and built and experimental results are reported in chapter **??**.

1.6 Thesis structure

Approaching the study of acousto-optic is quite challenging because the AO interaction relies on the interaction of the acoustic field with the optical field. The author decided to follow the step of [6] introducing first the optical properties of the crystals (chapter 2) and then the acoustic wave in anisotropic materials (chapter 3). The theory of the AO interaction is introduced in chapter 4. The study of the resonant AOTF made of TeO_2 is reported in chapter 5. The study carried over for the AOTF based on Calomel is reported in chapter 6, extending the wavelength range above 4.5 μm. The Quartz AOTF has been investigated in chapter **??**. A special case of an imaging AOTF designed to work with dual polarization AOTF is reported in chapter 7. The effect of acoustic attenuation in very large aperture AOTFs has been investigated in chapter 8.

Chapter 2

Optical properties of anisotropic crystals for Acousto-Optic applications

2.1 Introduction

Acousto-Optic (AO) devices rely on the interaction between acoustic and incident electromagnetic waves, the optical properties of AO materials are summarized in this chapter; the acoustic wave properties in AO crystals are the topic of chapter 2.
The choice of the AO medium is dictated by the transmission range and by the AO properties, such as the acousto-optic figure of merit (M_2), birefringence, and other physical and manufacturing aspects. An analysis is necessary to verify that all the aspects required to build a functional devices are satisfied.
The wavelength range studied starts from deep-UV up to Long Wave Infra-Red (LWIR) up to 10μm, therefore different materials are required to cover this range. In practice three different intervals can be identified [6]:

- **180 nm** $< \lambda <$ **450 nm**: Crystal Quartz [32] and KDP [$\bar{4}2m$]
- **450 nm** $< \lambda <$ **4500 nm**: Tellurium Dioxide (TeO_2) [422]
- $\lambda >$ **4500 nm**: Mercurous halides and Single Crystal Tellurium [$32m$]

The transmission windows of Quartz and KDP extend well above 450 nm but the poor acousto-optic figure of merit compared to tellurium dioxide limits the use only in the UV range [3], where the transmission of other AO materials is not efficient. The same limit is applied to the IR material such mercurous halide (e.g. mercurous

chloride transmits from 450 nm up to 20 μm) and single crystal tellurium (3.5 μm – 36 μm). Hence for the wavelength range between 450 nm and 4.5 μm Tellurium Dioxide is the common material of choice to build AOTF due to its high AO figure of merit and availability of crystal of large dimension with good optical quality; in addition the manufacturing process is well established in Gooch and Housego Ltd. (UK).
The next section is dedicated to the optical properties of the crystals listed above, where the data available in literature are examined to identify the best data set to be introduced in the developed design routine.

2.2 Optical properties of Acousto-Optic crystals

The wavelength dependency of the refractive index can be described empirically by the Sellmeier equation or in some case by curve fitting of experimental data.
The acousto-optic crystals investigated are all positive uniaxial birefringent crystals, which are characterized by two refractive indexes surfaces identified by the polarization state. The ordinary and extraordinary refractive index surfaces are related by the vertical and horizontal polarizations, respectively.
In non optical active material the refractive index surfaces for birefringent materials are defined for the ordinary polarization as a sphere of radius n_O and by an ellipsoid rotated about the optical axis with the minor axis equal to n_O along Z and the major axis perpendicular to Z equal to n_E. The values of the refractive index in a plane rotated about the Z axis for the ordinary refractive index is defined by:

$$n_o(\lambda, \theta) = n_O(\lambda) \tag{2.1}$$

and for the refractive index of the extraordinary ray is:

$$n_e(\lambda, \theta) = \sqrt{\frac{n_O(\lambda) n_E(\lambda)}{n_O^2(\lambda)\sin^2(\theta) + n_E(\lambda)^2\cos^2(\theta)}} \tag{2.2}$$

where n_E is the extraordinary refractive index for perpendicular propagation direction to the optical axis. The refractive index surfaces in the k-space diagram are shown in Fig.(2.1(a)) in absence of optical activity.
The refractive indexes of Crystal Quartz, Tellurium Dioxide (TeO_2), and Calomel are studied in the wavelength range of interest for the AO applications of interest.

2.3 Optical activity in crystals

Among the AO crystals examined tellurium dioxide and crystal quartz are also characterized by optical activity. If the optical activity is introduced then the two surfaces are separated by a quantity δ at the optical axis, which affects the shape of the refractive index surfaces.

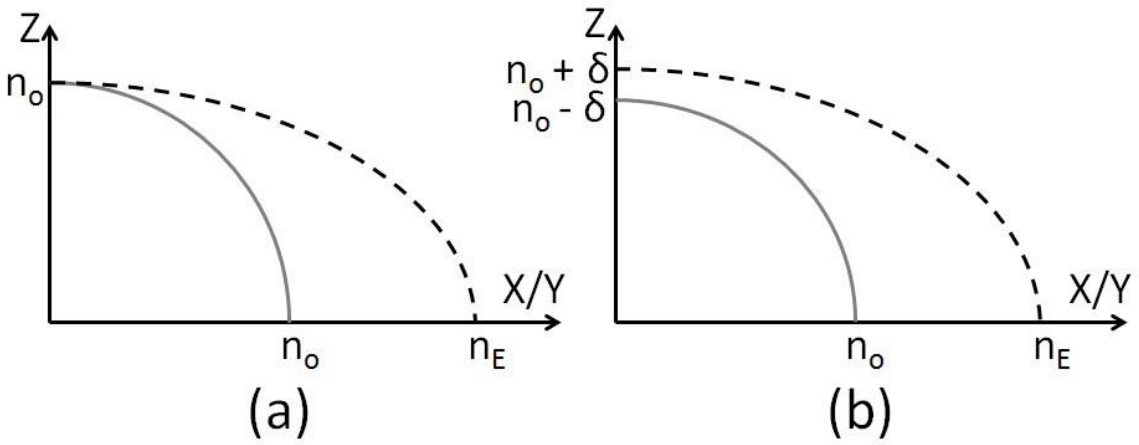

Figure 2.1: Refractive index surfaces for non-opitcal active crystal(a) and for an optical active crystal(b).

The magnitude of δ is wavelength dependent because the optical activity is related to the optical rotatory power, which is dispersive with wavelength. The effect of the optical rotatory power is to rotate the polarization of plane wave propagating along the optical axis. This effect has been studied for long time and in literature are reported the values for different optical active crystals [8][9][10] and it is used to realize rotators. In general, the rotatory power is defined by ρ [deg/mm] and its sign is defined by the handiness of the crystal. In this thesis the sign convention used is described by Nye [8], where for left handed quartz the rotatory power is considered negative, and for right handed quartz is positive.

The handiness will affect only the rotation direction, and has to be taken in account for devices with input direction close to the optical axis (such as acousto optic pecialtor), in other AO devices the handiness is relevant only during the orientation of the crystal, because we deliberately choose to operate away from the optic axis to keep the eigenstates of polarization approximately linear.

The perturbation (δ) of the refractive index surfaces along the optical axis for an arbitrary wavelength is defined by:

$$\delta = \frac{n_o^2 \Gamma(0)}{2} \tag{2.3}$$

where Γ(0) is the activity tensor along the optical axis. A simplified model is introduced by Xu and Stroud [6] where δ is a constant deformation of the refractive index surfaces only at the optical axis, hence both surfaces become ellipses and the new ordinary and extraordinary index surfaces are defined by:

$$n_o(\theta) = \sqrt{\frac{n_o^2(1-\delta)}{n_o^2(1-\delta)^2 \sin^2(\theta) + n_o^2 \cos^2(\theta)}} \tag{2.4}$$

$$n_E(\theta) = \sqrt{\frac{n_o(1+\delta)n_E}{n_o^2(1+\delta)^2 \sin^2(\theta) + n_E^2 \cos^2(\theta)}} \tag{2.5}$$

with δ defined in Eq.2.3. This approximation is only applicable for small angle of propagation from Z axis; if extended to the whole plane this model leads to a wrong estimation of the optical activity magnitude, because the perturbation of the refractive index surfaces is still present for propagation far from the optical axis and disappear only for direction perpendicular to the optical axis, this model is also reported by Simons et al.[11], where the polarization of the light travel unchanged only for direction perpendicular to the optical axis. The perturbation created by optical activity in an

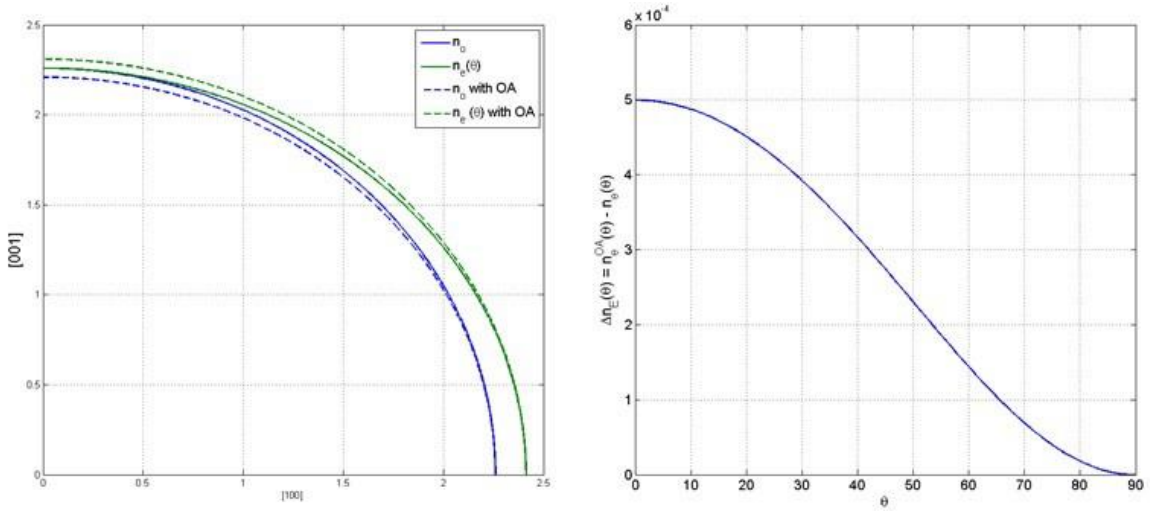

Figure 2.2: Refractive index surfaces of the extraordinary and ordinary polarizations with optical activity, dotted line, and without optical activity, solid line (left). Difference of the refractive indexes due to the optical activity (right).

Ideal crystal applying the model described by Xu and Stroud [6] is shown in Fig.2.2(a), as expected the effect of the optical activity disappears only at a direction perpendicular to the optical axis (Fig.2.2(b)). Experimentally it has been seen that the optical activity effects become negligible after a critical angle, which is material dependent, hence the previous model shows its limited validity for direction far from the optical axis.

Nye [8] describes the optical activity effects for an arbitrary propagation direction from the optical axis introducing the gyration tensors (G)[8] for two directions one parallel

and one perpendicular to the optical axis. This model allows to extend the validity of the optical activity effect for any propagation direction, because the gyration scalar is defined as:

$$G = g_{ij} l_i l_j \tag{2.6}$$

where g_{ij} are the components of the gyration tensor, and l_i and l_j are the cosine direction. The rotatory power is equal to:

$$\rho = \frac{\pi G}{\lambda \bar{n}} \tag{2.7}$$

where $\bar{n} = \sqrt{n_o n_E}$ stands for the geometric mean refractive index. The optical activity is introduced using the activity tensor Γ in [6], which is related to the gyration tensors by:

$$\Gamma_{ij} = n_i n_j G \tag{2.8}$$

The components of the gyration tensor depends on the crystal symmetry and in case of tetragonal and trigonal crystals is represented in matrix notation as:

$$g_{ij} = \begin{bmatrix} g_{11} & 0 & 0 \\ 0 & g_{11} & 0 \\ 0 & 0 & g_{33} \end{bmatrix} \tag{2.9}$$

therefore introducing Eq.2.9 in to Eq.2.3 using Eq.2.8 and Eq.2.6 then

$$\delta(\theta) = \frac{g_{11} \cos^2\theta + g_{33} \sin^2\theta}{2n_o^2} \tag{2.10}$$

then for a propagation angle perpendicular to the optical axis ($\theta = 0^\circ$) the optical activity creates a perturbation proportional to $\delta = g_{11}/(2n_o^2)$, and for a propagation direction parallel to the optical axis becomes $\delta = g_{33}/(2n_o^2)$.
The optical activity is introduced to investigate the different aspect related to the AO material used such as handiness and birefringence and its magnitude for different materials is reported in the next section.

2.4 Optical Properties of Crystal Quartz

The refractive indexes of crystal quartz is reported by Ghosh [12] and extensive study has been done to fully characterize the wavelength dependency of the material. The dispersion of the refractive index is described by the Sellmeier equation with two oscil-

lators:

$$n = \sqrt{A + \frac{B\lambda^2}{\lambda^2 - C} + \frac{D\lambda^2}{\lambda^2 - E}} \tag{2.11}$$

where λ in micrometer and the constant values for both polarizations are reported in Tab.A.1. The ordinary and extraordinary refractive indexes of crystal quartz were considered only in the region of interest for specific AO applications; they are shown in Fig.2.3(a); the variation of the birefringence with wavelength is shown in Fig.2.3(b). Crystal Quartz is an optical active material, therefore the polarization of the light

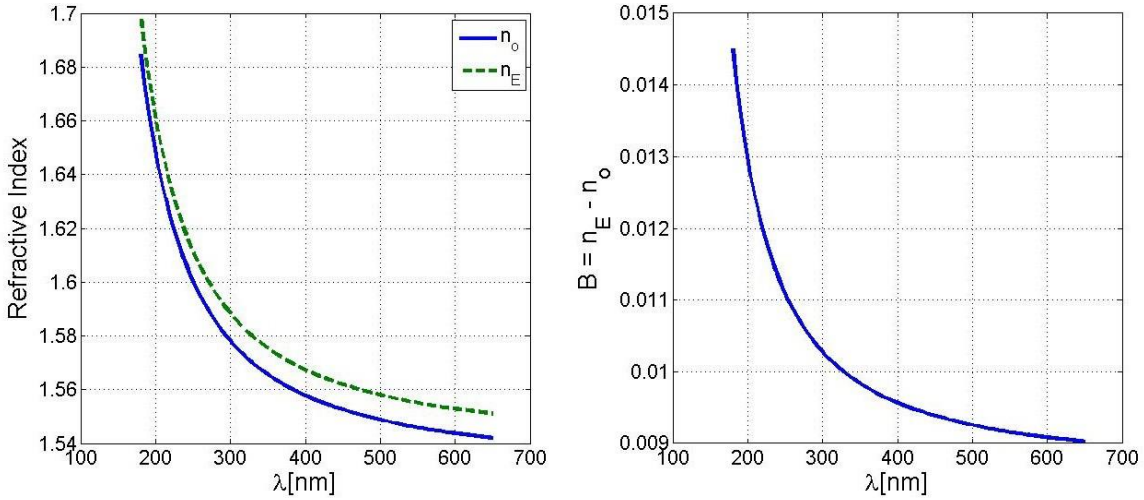

Figure 2.3: Refractive index of ordinary, solid line, and extraordinary ray, dotted line, for the wavelength range of interest (left). Birefringence versus wavelength (right).

Undergoes to a rotation while propagating inside the crystal, and the perturbation of the refractive index surface is described in the next section.

2.4.1 Optical Activity in Crystal Quartz

The gyration tensors for crystal quartz are reported in literature for $\lambda = 510$ nm by Nye [8] and are equal to $g_{11} = \mp 5.82 \times 10^{-5}$ and $g_{33} = \pm 12.96 \times 10^{-5}$, where the right-handed quartz is for the upper sign and the left-handed quartz is the lower sign. The value of δ is estimated introducing Eq.2.10 for a given wavelength. The dispersive nature of the gyration tensor has been investigated by Arteaga[13]:

$$g_{ii} = \frac{A_i \lambda^3}{(\lambda^2 - B_i^2)^2} \tag{2.12}$$

with λ expressed in meter and the constants A_i and B_i reported in Tab.2.1 for a wavelength range between 200 nm and 800 nm. From the values of g_{ii} obtained from

g_{ii}	Handiness	A_i	B_i
g_{11}	LH	27.7E-3± 1.7E-3	105.6±5.7
g_{11}	RH	-29.8E-3± 1.5E-3	91.1±4.2
g_{33}	LH	-60.9E-3± 0.2E-3	97.54±0.05
g_{33}	RH	60.4E-3± 0.5E-3	97.33±0.05

Table 2.1: Constants for the dispersion equation of the gyration components in crystal quartz.

2.12 is possible to estimate the rotatory power of crystal quartz for an electromagnetic wave propagating along the optical axis introducing Eq.2.12 into Eq.2.8 obtaining:

$$\rho(\lambda) = \frac{\pi g_{33}}{\lambda n_o} \tag{2.13}$$

which has been compared with the values reported by Bagan et al.[9]. The rotary power has been measured for a wavelength range between 0.408 μm and 1.565 μm propagating along the optical axis and a best-fit relation is reported:

$$\rho(\lambda) = a_1 + a_2 e^{-\frac{\lambda}{a_3}} + a_4 e^{-\frac{\lambda}{a_5}} + a_6 e^{-\frac{\lambda}{a_7}} \tag{2.14}$$

where $a_1 = 1.65569432$, $a_2 = 1104.28722386$, $a_3 = 0.09862624$, $a_4 = 181.71620197$, $a_5 = 0.05857032$, $a_6 = 88.56794745$, $a_7 = 0.35912872$.

There are no values reported for the other gyration tensor g_{11} for a broad wavelength range, but only for $\lambda = 510$ nm, which is confirmed by [13]. The validity of the results reported by Arteaga et al. [13] and by Bagan et al. [9] in the wavelength range within 200 nm and 800 nm is shown in Fig.2.4(a), and the related error with the Bagan values is shown Fig.2.4(b).

The best-fit curve accuracy drops for wavelengths below 400 nm, and cannot be used in case of AOTF design. An angle where the optical activity is absent could be determined from Eq.2.10, solving

$$f(\theta) = g_{11}\cos^2\theta + g_{33}\sin^2\theta \tag{2.15}$$

in the wavelength range from 200 nm up to 800 nm the critical angle where the optical activity is zero changes with wavelength as shown in Fig.2.5.

In conclusion two different set of values has been found in literature, for $\lambda > 400$ nm both sets are in good agreement with the experimental results. For $\lambda < 400$ nm only

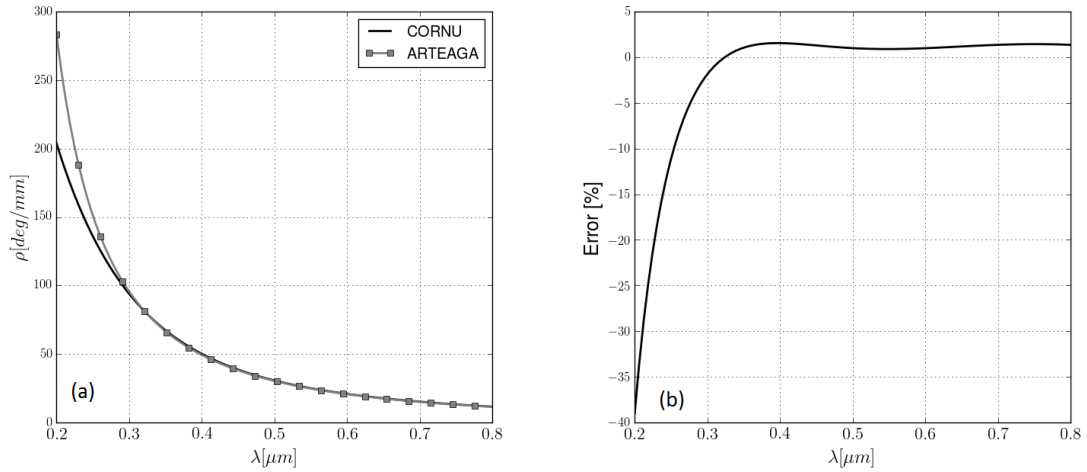

Figure 2.4: Optical activity versus wavelength using Arteaga and Cornu formula(a). Error between the two models (b).

the values reported in [13] seems to give a better estimation of the optical activity in crystal quartz.

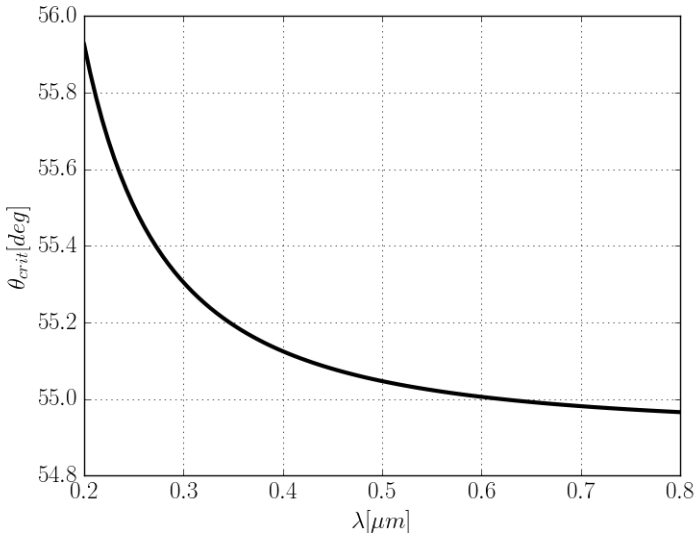

Figure 2.5: Variation of the critical angle with wavelength.

2.5 Tellurium Dioxide

Tellurium Dioxide has a transmission range from 380 nm to 4.5μm. In the literature are reported different values of the refractive indexes obtained from experimental results, Uchida [14] measured the refractive indexes for the wavelength range up to 1 μm using the Sellmeier's formula with two oscillators. In order to extend the refractive index

values to the whole transmission range of TeO_2, new values have been searched in literature. Berny et al.[15] published a later study on refractive index of TeO_2 extending the measurement up to 4.5 μm, and proposing the following dispersion formula:

$$n = \sqrt{A + \frac{B}{\lambda^2 - C} - D\lambda^2} \tag{2.16}$$

where the constant are reported in Tab.A.2 and in Tab.A.3 for the ordinary and extraordinary refractive index, and λ is expressed in micrometers .

A later study has been reported by Georgiev et al. [16], where a fitting to improve the accuracy of the available data from 2 μm up to 4μm has been proposed using the following equation:

$$n = \sqrt{1 + \frac{A}{\lambda^2 - B^2} - \frac{C}{\lambda^2 - D^2}} \tag{2.17}$$

where λ is expressed in micrometers and the constant values of the ordinary and extraordinary polarization are reported in Tab.A.2 and in Tab.A.3, respectively.

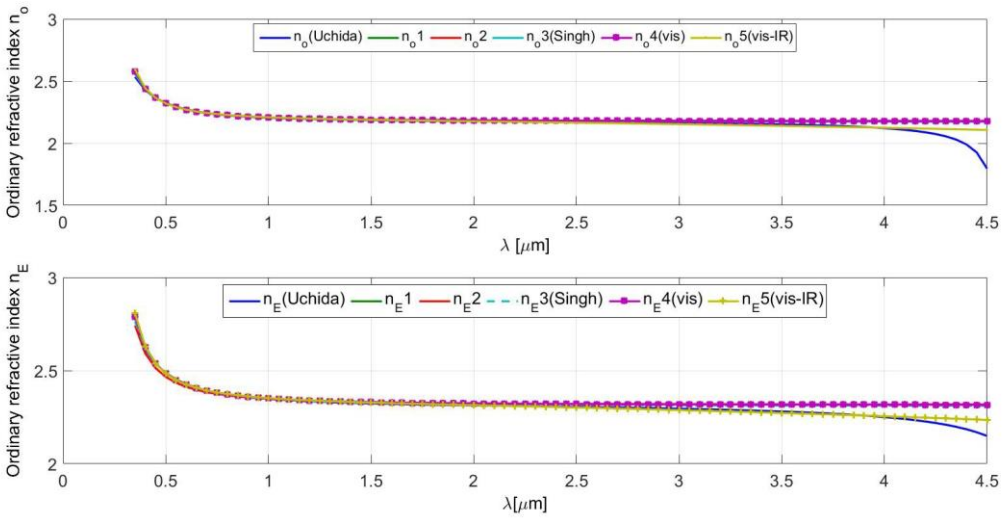

Figure 2.6: Change of refractive index with wavelength using the dispersion equations reported in literature for ordinary (top) and extraordinary (bottom) refractive indexes.

The different dispersion formulas had been compared to highlight any discontinuity and discrepancy. The dispersion equations for the refractive indexes show similar trend but their validity ranges are extended up to different wavelengths. A discontinuity in the vicinity of 4.5μm using Eq.2.17 is visible, therefore particular attention has to be paid when in the AOTF design process. The change of birefringence with wavelength shown in Fig.2.7 highlight the limitation of the Sellmeier equation from [REF1] - [REF2] - [REF3], leading to a discrepancy between the theoretical and experimental results on the tuning curve of AOTFs.

The different dispersion formula have been introduced on the AOTF design routines

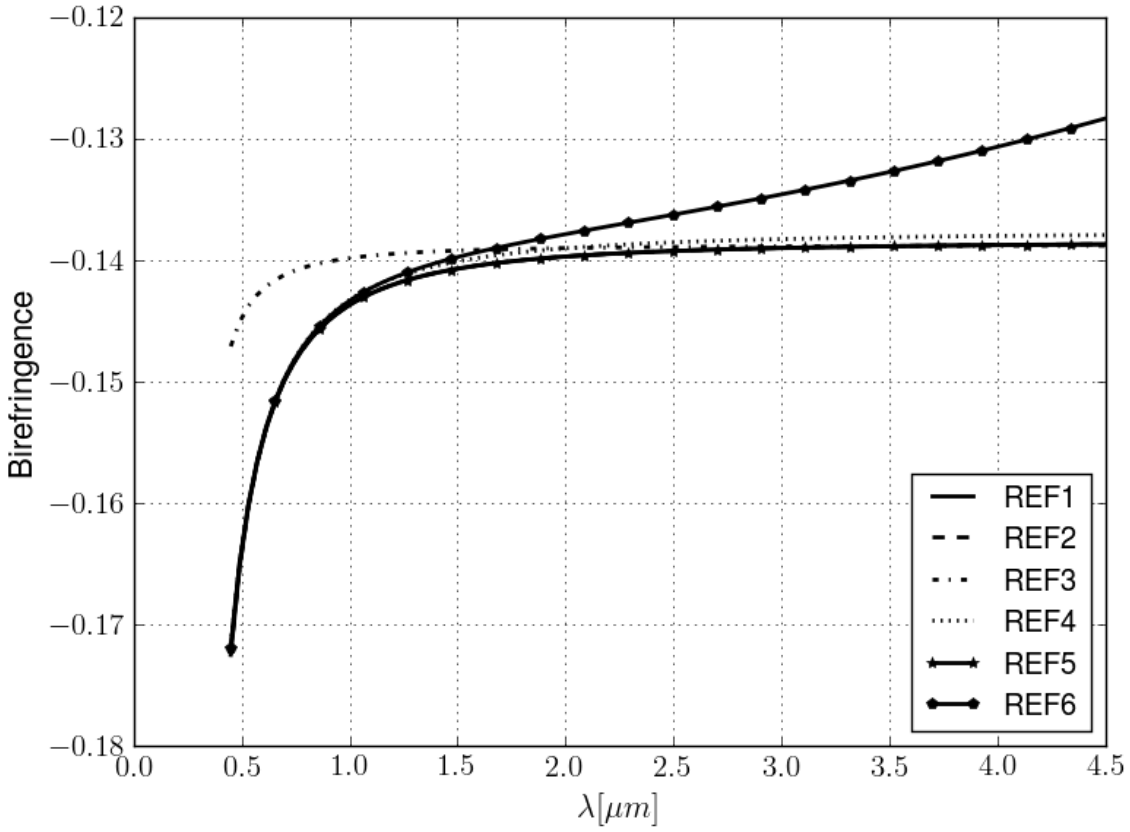

Figure 2.7: Change of birefringence with wavelength using the dispersion equations reported in literature.

Develop, and the prediction have been compared to the experimental results obtained from commercial and prototype devices built in G&H.

2.5.1 Optical Activity in TeO_2

Tellurium Dioxide (TeO_2) is an optical active crystal characterized by strong optical rotatory power. The optical activity along the optical axis has been investigated by Bagan et al. [9] and its wavelength dependency [deg/mm] is defined by a best-fit equation:

$$\rho(\lambda) = \left[\frac{43.2}{\lambda^2 - 0.08099716} - \frac{17.7}{\lambda^2 - 0.04293184} \right] (1.008 - 0.0372\lambda)^{-1} \qquad (2.18)$$

with λ expressed in micrometer and valid in the wavelength range between 408 nm and 1.565 μm. The value of the gyration tensor g_{33} could be estimated from Eq.2.18. The other components of the gyration tensor (g_{11}) related to the propagation direction perpendicular to the optical axis could be inferred by the study published by Kaminsky et al. [10], where the rotatory power for three different wavelengths is reported. Due to the high birefringence of the material the accuracy achieved is quite low for this component of the gyration tensor.

In case of TeO_2 experimental results obtained from AOTF testing show that in practice the effect of the optical activity become negligible when the propagation direction of the electro magnetic wave is above 10° from the optical axis.

In conclusion, the optical activity of Tellurium Dioxide (TeO_2) requires further research activity, although the high birefringence limits the accuracy achievable of the optical activity along the perpendicular direction of the optical axis. The model described by Xu and Stroud [6] is not valid for propagation direction far from the optical axis, because the presence of the gyration tensor (g_{11}) means that some sort of perturbation exists for perpendicular direction to the optical axis, as described by Nye [8] and confirmed by measurement done by Kaminsky [10].

2.6 Calomel single crystal

Mercurous Chloride, known also as Calomel single crystal, has an extended transmission range from 450 nm to 20 μm and it has been selected has a candidate to develop AO devices for wavelengths > 4.5 μm, under the MINERVA Project, which is an EU

framework 7 project[1]. The dispersion formulas of the refractive indexes are obtained from an internal document released by BBT, which is a crystal growth company part of the consortium of MINERVA pecialized on growing Calomel crystals with good optical quality.

The values reported by BBT allow to calculate the change of the refractive index values with wavelength using a polynomial fitting from experimental data:

$$n_o = 1.898 + 1.5 \times 10^{-2} E_{ph}^2 + 3.7 \times 10^{-4} E_{ph}^4 + \\ +7 \times 10^{-6} E_{ph}^6 + 4 \times 10^{-7} E_{ph}^8 + 5 \times 10^{-8} E_{ph}^{10} \quad (2.19)$$

$$n_E = 2.444 + 3.87 \times 10^{-2} E_{ph}^2 + 1.73 \times 10^{-3} E_{ph}^4 + \\ +4.5 \times 10^{-5} E_{ph}^6 + 3.46 \times 10^{-6} E_{ph}^8 + 3 \times 10^{-7} E_{ph}^{10} \quad (2.20)$$

with the photon energy E_{ph} [eV] defined by:

$$E_{ph} = \frac{hc}{\lambda} \quad (2.21)$$

where h is the Planck's constant, c is the speed of light and λ is the wavelength in the vacuum. The transmission range for Calomel is up to 20μm and the change of the refractive index is shown in Fig.2.8.

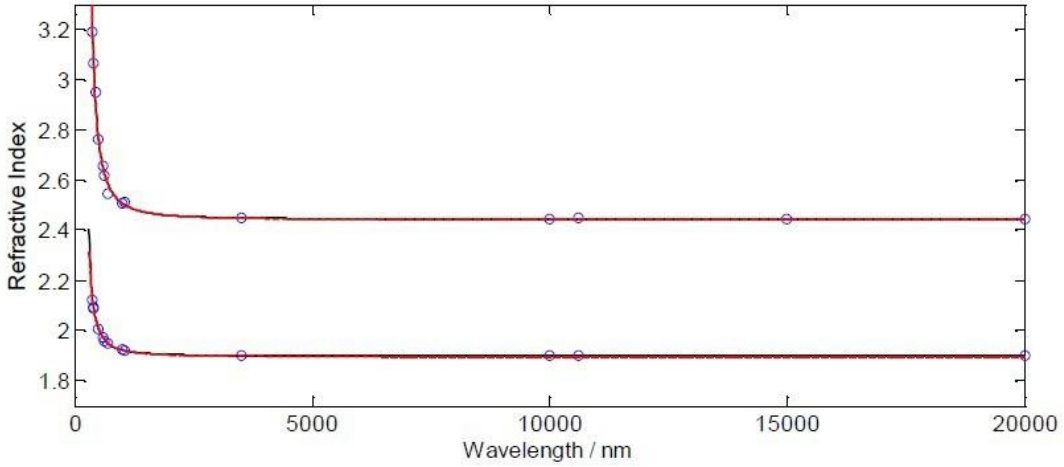

Figure 2.8: Refractive index values vs. wavelength for Calomel Single crystal

The accuracy of these equation has not been verified experimentally due to the lack of suitable equipment in G&H, but from AO experiments it is shown a good agreement with the values obtained from Eq.2.19- Eq.2.20.

[1] http://minerva-project.eu/

2.7 Conclusions

The refractive index values and related birefringence of different AO materials have been reported. In case of crystal quartz the refractive index is well characterized in UV and visible region and for AO applications the wavelength interval of interest is between 200 nm and 450 nm. The refractive indexes of tellurium dioxide (TeO_2) has been measured for $\lambda < 1\mu$m by Uchida [14], and different dispersion equations have been found in the literature for 1 μm $< \lambda <$ 4.5 μm. The accuracy of the refractive index values is relevant on the performance predictions of AOTFs, and it will affect the design routines.

Tellurium dioxide and crystal quartz are optically active, and the introduction of optical activity inside AO interaction physics is reported in the literature [6] but it is only applicable to an optical beam propagating along the optical axis. AOTFs typically are designed with an incident direction far from the optical axis, therefore a different model has been introduced, which extends its validity to any direction in the AO plane. Crystal quartz is fully characterized and the values of both gyration tensors are reported; in case of TeO_2 only one value of the gyration tensor has been found in literature and it is proposed a possible values for the other gyration tensor (g_{33}) by Kaminsky [10].

Chapter 3

Acoustic waves in anisotropic material

The fundamental equations to described the acoustic waves properties in anisotropic crystals are reported with particular attention to the phase velocity and acoustic walk-off for all the pure acoustic modes, which could be excited by conventional ultrasonic transducer as described in appendix C.
The properties of acoustic waves depend on the propagation direction and on the selected mode, due to the anisotropic nature of the material under consideration. Theoretical models to predict the properties of acoustic waves in anisotropic materials are introduced this chapter, where the phase velocities and related acoustic modes are obtained from the solution of Christoffel equation with the help of the point restriction symmetry of the crystal.

3.1 Anisotropic crystals symmetry

The symmetry of the AO crystals is applied to study acoustic wave propagation in anisotropic materials [17] with the help of symmetry point diagrams, which allow to determine the position of reference axes inside the crystals.
The point group restriction is obtained from the symmetry point diagram and reducing the complexity of Christoffel equation's solution. The AO materials examined listed belong either to tetragonal or trigonal crystal symmetry, thus no other crystal symmetries are examined in this thesis.
The point diagram symmetry for the trigonal class 32 is shown in Fig.3.1(a), where there are three axes of two-fold symmetry (120° apart) and one axis of three-fold symmetry perpendicular to the former. The axes in the plane perpendicular to the optical axis are separated by 30° as shown in Fig.3.2, for example rotating clockwise the plane

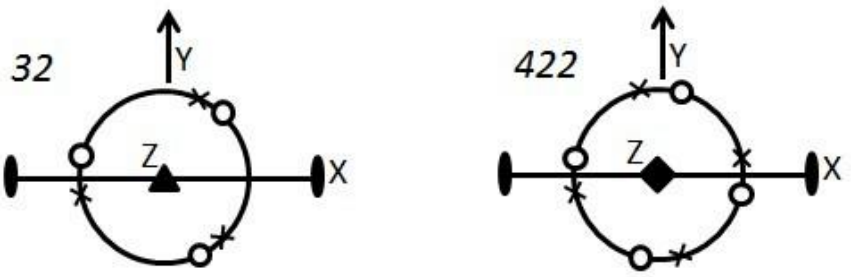

Figure 3.1: Point diagram symmetry for crystal class 32 (left) and 422(right)

of 30° about the Z axis starting from the positive direction of the X axis the negative direction of Y is selected. The low symmetry of the trigonal is affecting the symmetry of the phase velocity in anisotropic material thus particular attention is required when orienting the crystal, because the positive directions of axes need to be identified correctly inside the crystals.

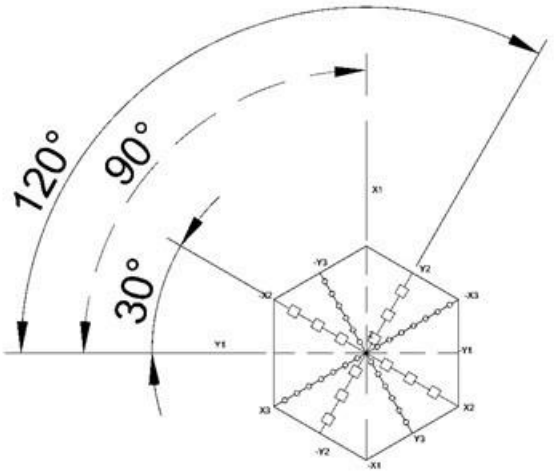

Figure 3.2: Axes orientation and position in a perpendicular plane

Crystal Quartz and single crystal Tellurium belong to this crystal class.
The tetragonal crystals 422 is shown in Fig.3.1, and the axes are perpendicular to each others due to the higher symmetry of the materials; from the acoustic point of view the direction of the axes are interchangeable, leading to a great simplification in the crystal alignment process. TeO_2 and Calomel single crystal belong to this crystal class.

3.2 Acoustic wave in anisotropic material

The analytical solution of acoustic phase velocity has been investigated in order to create mathematical model which could be implemented easily inside computer routines

to be used in the design process of prototype and commercial devices.
The first step is to study the phase velocity of each acoustic mode in the three dimensional space and on the specific plane of interest for the AO interaction by means of routines developed in Matlab and Python.

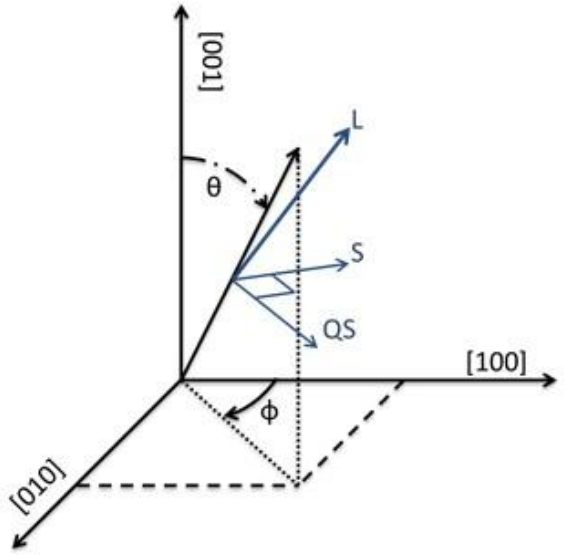

Figure 3.3: Reference angles and displacement of different acoustic modes.

In general, the phase velocity of elastic waves for an arbitrary direction is estimated by solving the Christoffel equation [**?**]:

$$\begin{aligned}[\Gamma_{ij} - \rho V^2 \delta_{ij}]\, v_j = 0 \\ \Gamma_{ij} = l_{iK} c_{KL} l_{Lj}\end{aligned} \tag{3.1}$$

where ρ is the density of the material, V is the phase velocity, and $v_j = \partial \mathbf{u}/\partial t$, where $\mathbf{u}$ is the particle displacement vector, and $[l_{iK}]$ is equal to

$$[l_{iK}] = \begin{bmatrix} l_x & 0 & 0 & 0 & l_z & l_y \\ 0 & l_y & 0 & l_z & 0 & l_x \\ 0 & 0 & l_z & l_x & l_y & 0 \end{bmatrix} \tag{3.2}$$

where

$$l_x = cos(\phi)sin(\theta) \tag{3.3}$$

$$l_y = sin(\phi)sin(\theta) \tag{3.4}$$

$$l_z = cos(\theta) \tag{3.5}$$

where θ is evaluated from [001] direction, and ϕ is evaluated from [100] direction (Fig.3.3)

$$[l_{Lj}] = [liK]^T \tag{3.6}$$

and $[c_{KL}]$ is the elastic stiffness matrix defined in compact form described by:

$$[c_{KL}] = \begin{bmatrix} c_{11} & c_{12} & c_{13} & c_{14} & c_{15} & c_{16} \\ c_{12} & c_{22} & c_{23} & c_{24} & c_{25} & c_{26} \\ c_{13} & c_{23} & c_{33} & c_{34} & c_{35} & c_{36} \\ c_{14} & c_{24} & c_{33} & c_{44} & c_{45} & c_{46} \\ c_{15} & c_{25} & c_{35} & c_{34} & c_{55} & c_{56} \\ c_{16} & c_{26} & c_{36} & c_{46} & c_{56} & c_{66} \end{bmatrix} \tag{3.7}$$

which is simplified by the point group restriction dictated by the crystal symmetry. The phase velocity and its polarization are determined by the eigenvalues and eigenvectors obtained from the solution of Eq.3.1. Only a maximum of three eigenvectors are obtained in anisotropic crystal identified by the eigenvector direction. The longitudinal mode (L) has the particle displacement along the propagation direction, and the slow-shear (SS) and fast-shear (FS) modes have the particle displacement transversal to the propagation direction.(Fig.3.3).

In general the phase velocities in solids is obtained by the eigenvalues of Eq.3.1

$$V = \sqrt{\frac{\lambda_i}{\rho}} \tag{3.8}$$

where λ is the eigenvalue with $i = 1..3$ and the related eigenvectors correspond to the polarization direction, which define the acoustic modes. The solution of Eq.(3.1) is found for a specific crystal class introducing point groups symmetry, in particular the trigonal (32,3m,$\bar{3}$m) is examined to study the acoustic wave propagation in Crystal Quartz. The tetragonal class (4mm, 422, $\bar{4}$2m,4/mmm) symmetry is applied to study the acoustic waves in Tellurium dioxide and Calomel.

3.2.1 Walk-off of acoustic velocity

The acoustic energy in general anisotropic crystals propagates in a different direction to the phase velocity, and it is theoretically estimated by the Poynting theorem [17]. This effect is known as *acoustic walk-off* and it is defined as the normal to the tangent of the slowness surface for a given direction of the acoustic wave; the angle Δ between

the phase and the group velocity is defined by:

$$\tan(\Delta) = \frac{1}{V(\theta)} \frac{\partial V(\theta)}{\partial \theta} \tag{3.9}$$

with reference to Fig.3.4. The direction of the acoustic energy flow inside the crystal

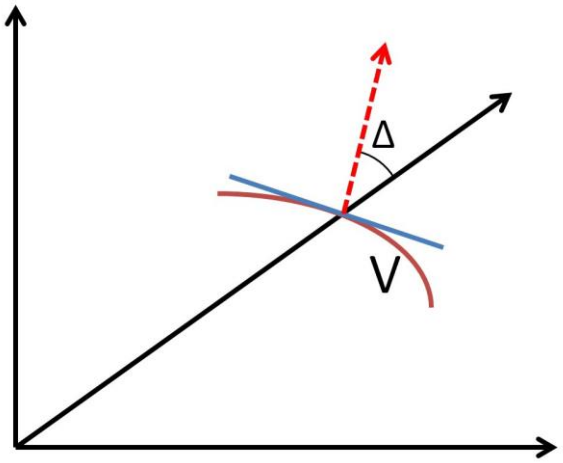

Figure 3.4: Definition of acoustic walk-off

is an important parameter needed to complete the practical design of the AO device, in order to avoid uncontrolled acoustic reflection inside the AO devices affecting the performance.

3.3 The acoustic attenuation in solids

The Christoffel equation described in Eq.3.1 describes an ideal material without internal energy losses. Materials of this type do not exist in nature, therefore additional term related to the elastic damping need to be introduced, defined as *acoustic attenuation*. These additional terms depend on the propagation direction in anisotropic crystal, and is expressed by the viscosity tensors (η_{abcd}) of the material symbolically described by [17]:

$$T_{ab} = C_{abcd} S_{cd} + \eta_{abcd} \frac{\partial S_{cd}}{\partial t} \tag{3.10}$$

where c is the elastic stiffness constant, **S** is the strain tensor and **T** is the stress tensor. The system can be described by the model, where the acoustic power is related to an applied force to a mass attached to a spring and the acoustic attenuation is the damping.

If a propagation of a plane wave is considered, then the acoustic attenuation can be

approximated by:

$$\alpha_{ij}(\boldsymbol{f},\theta_a) = \frac{\omega^2\eta_{ij}(\theta_a)}{2c_{ij}(\theta_a)}\sqrt{\frac{\rho}{c_{ij}(\theta_a)}} \tag{3.11}$$

where $\omega = 2\pi$f, and the acoustic phase velocity is defined by Eq.3.8 with $\lambda_i = c_{ij}(\theta_a)$, thus Eq.3.11 can be written as:

$$\alpha(\boldsymbol{f},\theta_a) = \frac{2\pi^2\boldsymbol{f}^2\ \eta(\theta_a)}{V(\theta_a)^3\quad\rho} \tag{3.12}$$

The effective viscosity is estimated solving the Christoffel equation introducing the dumping components η_{ij} in Eq.3.1. The detailed calculation is reported in appendix E. Acoustic attenuation is important, for example when estimating the performance of an AOTF with large aperture.

3.4 Tellurium Dioxide (TeO_2)

Tellurium Dioxide belongs to the tetragonal crystal class with four axes of two-fold symmetry and one with four-fold symmetry. The elastic stiffness constant matrix is simplified applying the restriction due to the point group symmetry of the tetragonal crystal class:

$$[c_{KL}] = \begin{bmatrix} c_{11} & c_{12} & c_{13} & 0 & 0 & 0 \\ c_{12} & c_{11} & c_{13} & 0 & 0 & 0 \\ c_{13} & c_{13} & c_{33} & 0 & 0 & 0 \\ 0 & 0 & 0 & c_{44} & 0 & 0 \\ 0 & 0 & 0 & 0 & c_{44} & 0 \\ 0 & 0 & 0 & 0 & 0 & c_{66} \end{bmatrix} \tag{3.13}$$

In the literature are reported several values for the elastic stiffness tensor components, furthermore the values reported in [6] are taken as a reference, thus $c_{11} = 5.57 \times 10^{10} N/m^2$, $c_{12} = 5.12 \times 10^{10} N/m^2$, $c_{13} = 2.18 \times 10^{10} N/m^2$, $c_{33} = 10.58 \times 10^{10} N/m^2$, $c_{44} = 2.59 \times 10^{10} N/m^2$, $c_{66} = 6.59 \times 10^{10} N/m^2$.

The three dimensional slowness curve is obtained by solving Eq.(3.1) for $0 < \phi < \pi$ and $0 < \theta < \pi$. The slow shear mode is shown in Fig.(3.5). The slowness curve representing the fast shear mode is shown in Fig.(3.6). The longitudinal mode is shown in Fig.(3.7). Tellurium Dioxide is a piezoelectric material, therefore the acoustic velocity is affected by it, but the change in acoustic velocity is negligible and not considered-

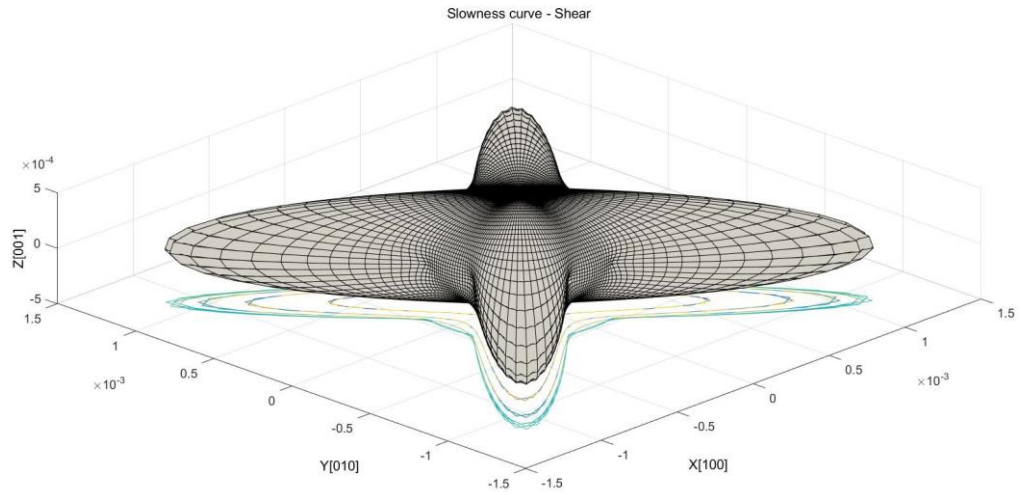

Figure 3.5: Three dimensional slowness curve of the slow shear mode

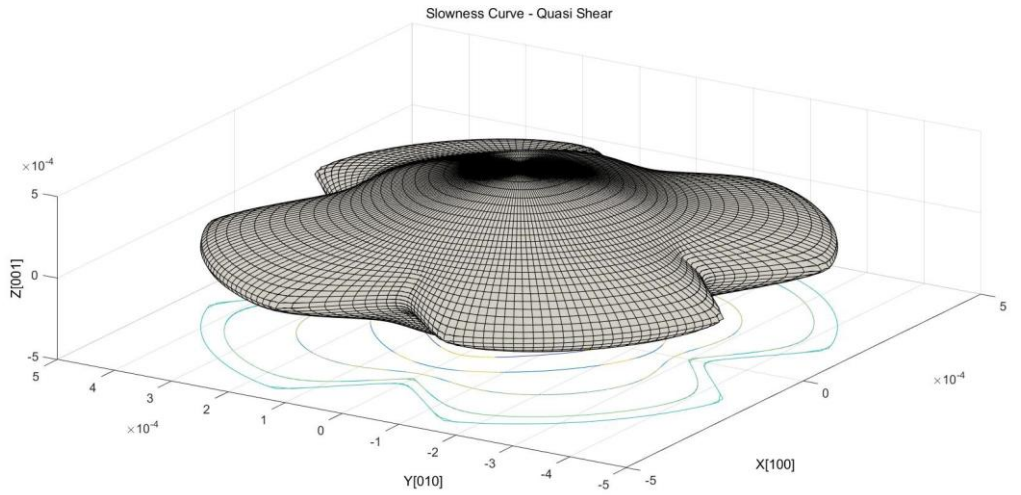

Figure 3.6: Three dimensional slowness curve of the fast shear mode

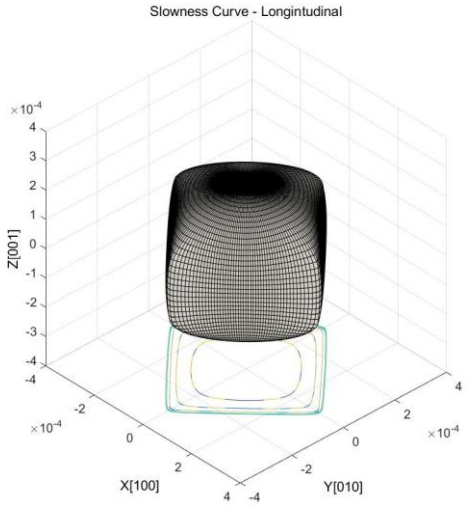

Figure 3.7: Three dimensional slowness curve of the longitudinal mode

Acoustic phase velocity in the [100]-[010] plane

Acoustic velocity in the [100]-[010] plane is obtained by substituting Eq.3.3- Eq.3.5 in Eq.3.2 and in Eq.3.6. The slow and fast shear modes are degenerate and cross each other at certain points of the space, therefore the solution of Eq.3.1 with Matlab solver does not keep track of the correct acoustic mode, as shown in Fig.B.1, due to the issue related to the linear algebra solver described in details in appendix B; consequently the solution of the Christoffel's equation cannot be directly introduced in the design routines.

An analytical expression of the phase velocity can be easily implemented in a design routines, for this reason Eq.(3.1) for a given direction of acoustic wave in space **(x,y,z)** in TeO_2 can be simplified as:

$$\begin{bmatrix} A-\rho V^2 & \sigma_1 & \sigma_3 \\ \sigma_1 & B-\rho V^2 & \sigma_2 \\ \sigma_3 & \sigma_2 & C-\rho V^2 \end{bmatrix} \begin{bmatrix} v_i \\ v_j \\ v_k \end{bmatrix} = 0 \qquad (3.14)$$

where

$$A = c_{44} + [c_{11}cos^2(\phi) + c_{66}sin^2(\phi) - c_{44}]sin^2(\theta) \quad (3.15)$$

$$B = c_{44} + [c_{11}sin^2(\phi) + c_{66}cos^2(\phi) - c_{44}]sin^2(\theta) \quad (3.16)$$

$$C = c_{44}sin^2(\theta) + c_{33}cos^2(\theta) \quad (3.17)$$

$$\sigma_1 = \tfrac{1}{2}[c_{12} + c_{66}]\sin^2(\theta)\sin(2\phi) \quad (3.18)$$

$$\sigma_2 = \tfrac{1}{2}[c_{13}\sin(\phi) + c_{44}\cos(\phi)]\sin(2\theta) \quad (3.19)$$

$$\sigma_3 = c_{44}\cos^2(\theta) \quad (3.20)$$

where the constants A, B, C, $\sigma_1, \sigma_2, \sigma_3$ have been obtained using the symbolic calculus toolbox available in Matlab, knowns as Mupad.
Acoustic velocities and polarization directions are evaluated from the eigenvalues and the eigenvectors of the Eq.(B.1). The acoustic velocity in *[100]-[010]* is equal to:

$$V^2_{[S,L]} = \frac{c_{11} + c_{66} \pm \sqrt{(c_{12} + c_{66})^2 \sin^2(2\theta) + [c_{66} + c_{11}(1 - 2\cos^2\theta)]^2}}{2\rho} \quad (3.21)$$

where positive sign refers to the longitudinal acoustic wave *(L)* and the negative sign is the shear acoustic wave *(S)*. The fast shear acoustic wave *(FS)* is determined by the third eigenvector:

$$V^2_{QS} = \frac{c_{44}}{\rho} \quad (3.22)$$

The acoustic velocity is shown in Fig.3.8 as a slowness curve, which is the inverse of the acoustic wave, in a polar plot.

Walk-off of the acoustic wave in XY plane

The wallk-off of the acoustic wave along in the XY plane is determined by $\boldsymbol{f}(\theta)$ for the shear acoustic wave is equal to has been calculated using Mupad and deriving the analytical expression of Eq.3.9 for specific planes :

$$\boldsymbol{f}(\theta) = \frac{4(c_{11} - c_{66})^2 \sin^3(\theta)\cos^3(\theta) + (c_{12} + c_{66})^2 \sin(4\theta)}{4\rho V_S^2(\theta)(c_{66} + c_{11} - 2\rho V_S^2(\theta))} \quad (3.23)$$

and for the longitudinal acoustic wave:

$$\boldsymbol{f}(\theta) = \frac{4(c_{11} - c_{66})^2 \sin^3(\theta)\cos^3(\theta) + (c_{12} + c_{66})^2 \sin(4\theta)}{4\rho V_L^2(\theta)(2\rho V_L^2(\theta) - c_{66} + c_{11})} \quad (3.24)$$

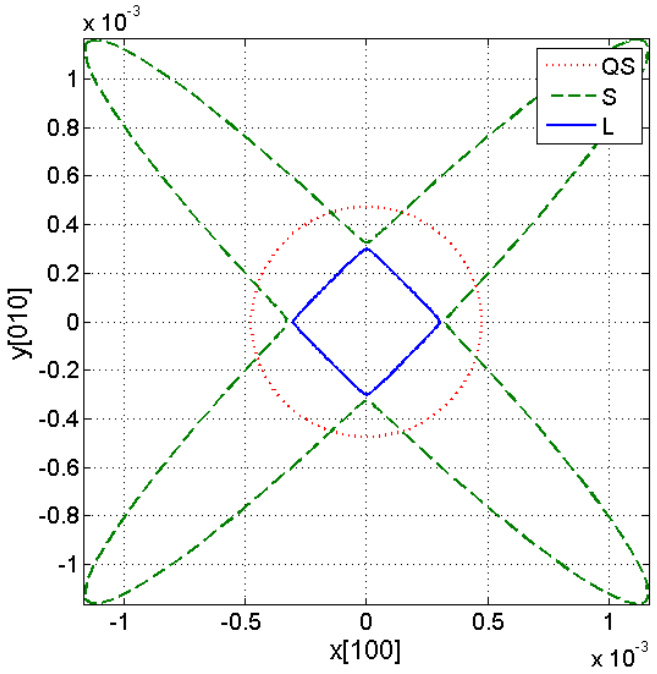

Figure 3.8: Slowness curve of the three acoustic wave mode in TeO_2 in [100]-[010] plane.

The acoustic walk-off is shown in (Fig.3.9)

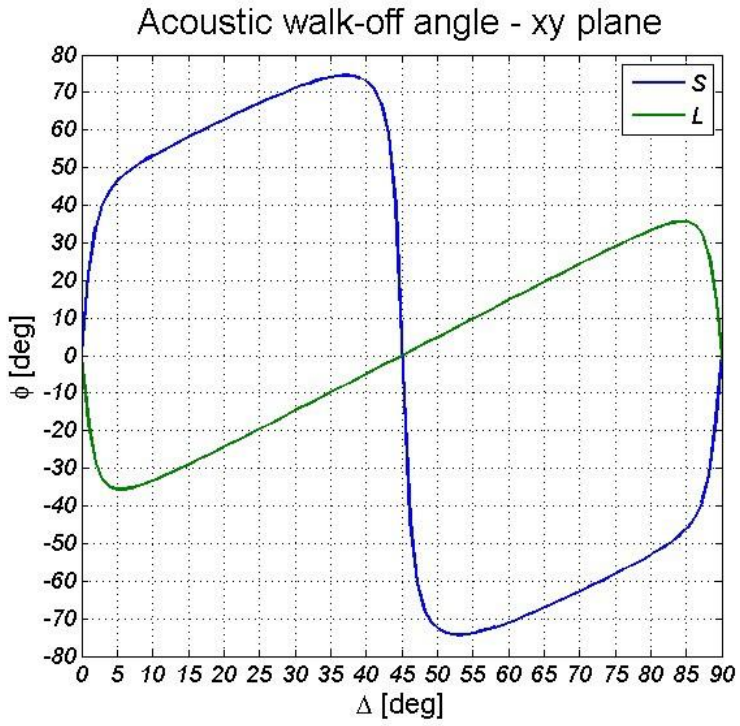

Figure 3.9: Acoustics walk-off in XY plane for TeO_2

This solution has been compared with the results reported in [18]

Acoustic Velocity along t[110]-Z[001]

The t[110]-Z[001] plane is the preferred plane for the slow shear AO interaction [6] and it is selected rotating the references plane about the Z axis of $\pi/4$ from [100] direction. The rotation of the reference axis is obtained by using the coordinate transformation matrices M_z (Eq.A.3) applied to the elastic stiffness constant matrix

$$[c'_{KL}] = [M_z(\theta)][c_{KL}][M_z(\theta)]^T \tag{3.25}$$

where θ is the angle of rotation about the Z axis. The new elastic stiffness constant matrix for a rotation equal to $\pi/4$ becomes:

$$[c'_{KL}] = \begin{bmatrix} c'_{11} & c'_{12} & c_{13} & 0 & 0 & 0 \\ c'_{12} & c'_{11} & c_{13} & 0 & 0 & 0 \\ c_{13} & c_{13} & c_{33} & 0 & 0 & 0 \\ 0 & 0 & 0 & c_{44} & 0 & 0 \\ 0 & 0 & 0 & 0 & c_{44} & 0 \\ 0 & 0 & 0 & 0 & 0 & c'_{66} \end{bmatrix} \tag{3.26}$$

where

$$c'_{11} = \frac{c_{11} + c_{12} + 2c_{66}}{2} \tag{3.27}$$

$$c'_{12} = \frac{c_{11} + c_{12} - 2c_{66}}{2} \tag{3.28}$$

$$c'_{66} = \frac{c_{11} - c_{12}}{2} \tag{3.29}$$

Introducing (Eq.3.26) in (Eq.3.1), the velocity of acoustic wave for a given direction of θ, which is defined from [110] direction, for the slow shear mode can be defined as:

$$V_S^2 = \frac{c'_{66}cos^2(\theta) + c_{44}sin^2(\theta)}{\rho} \tag{3.30}$$

The fast shear (FS) and longitudinal (L) modes are expressed by:

$$V^2_{[L,QS]} = \frac{c_{44} + c_{33} + [c'_{11} - c_{33}]\cos^2(\theta) \pm \sigma_1}{2\rho} \tag{3.31}$$

where

$$\sigma_1 = \sqrt{[(c_{33} - 2c_{44} + c'_{11})sin^2(\theta) + c_{44} - c'_{11}]^2 + (c_{13} + c_{44})^2 sin^2(2\theta)} \qquad (3.32)$$

The slowness curve of the t-Z plane in TeO_2 is shown in Fig.3.10. The inverse of the

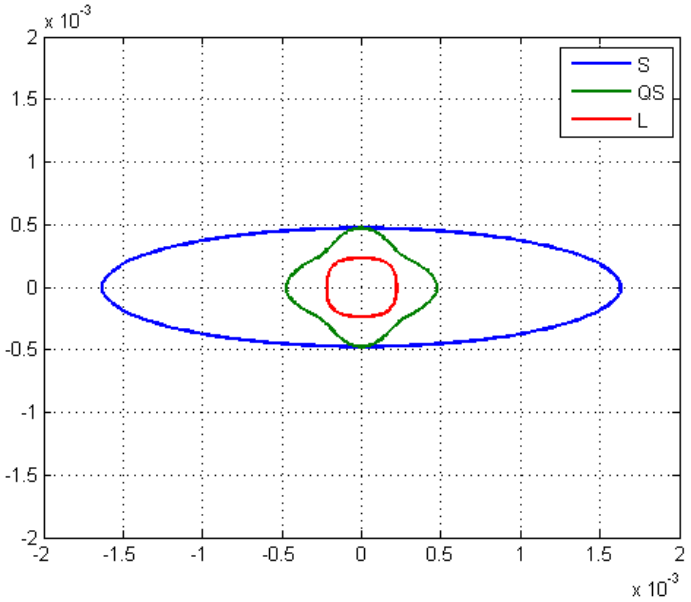

Figure 3.10: Slowness curve in tZ plane

acoustic wave of slow shear mode described by Eq.3.30 is a geometrical ellipse in a polar representation, where the slowest velocity is along the [110] direction and equal and the fastest velocity is along the optical axis. This plane is of primary importance in the design of AOTF made of TeO_2, because the AO interaction is characterized by a high acousto-optic figure of merit (M_2) due to the extremely slow shear velocity.

Walk-off in t-Z plane

The acoustic walk-off defined by Eq.3.9 applied to the acoustic mode in the t-Z plane could be solved by:

$$tan(\Delta) = f(\theta) \qquad (3.33)$$

where $f(\theta)$ is defined by the acoustic mode considered and the propagation direction defined by θ. The analytical expression of $f(\theta)$ is obtained by using Mupad and simplifying the expression obtained. The walk-off of the shear acoustic wave is determined by:

$$f(\theta) = -\frac{\frac{c_{66}}{\rho} - c_{44}}{2V(\theta)} sin(2\theta) \qquad (3.34)$$

where $V(\theta)$ is the acoustic phase velocity defined in Eq.3.30. The walk-off angle of the FS mode could be defined by:

$$f(\theta) = -\frac{\frac{C}{c_{11}^{'}cos^2(\theta)+c_{33}sin^2(\theta)+c_{44}-2\rho V^2(\theta)} + (c_{11}^{'} - c_{33})sin(\theta)cos(\theta)}{2\rho V^2(\theta)} \tag{3.35}$$

$$A = c_{33}(c_{11}^{'} - 3c_{44} + c_{33}) + c_{44}(2c_{44} - c_{11}^{'}) \tag{3.36}$$

$$B = c_{44}(2c_{44} - 3c_{11}^{'} - c_{33}) + c_{11}^{'}(c_{11}^{'} + c_{33}) \tag{3.37}$$

$$C = Acos(\theta)sin^3(\theta) - Bsin(\theta)cos^3(\theta) + (c_{13} + c_{44})^2 sin(2\theta)cos(2\theta) \tag{3.38}$$

where $V(\theta)$ is the acoustic velocity of the fast shear acoustic wave. The walk-off of the longitudinal acoustic wave is estimated by:

$$f(\theta) = \frac{\frac{C}{c_{11}^{'}cos^2(\theta)+c_{33}sin^2(\theta)+c_{44}-2\rho V^2(\theta)} + (c_{11}^{'} - c_{33})sin(\theta)cos(\theta)}{2\rho V^2(\theta)} \tag{3.39}$$

where $V(\theta)$ is the acoustic velocity of the longitudinal acoustic wave where C is given by (Eq.3.38)

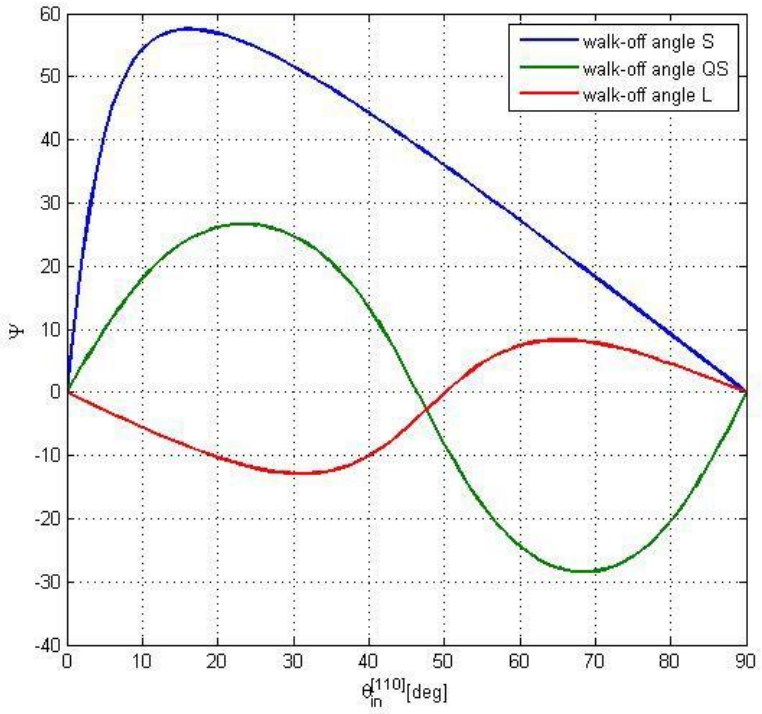

Figure 3.11: Acoustic walk-off in tZ plane for TeO_2

3.4.1 Acoustic attenuation in TeO_2

The acoustic attenuation in TeO_2 is defined by Eq.3.12, where the effective viscosity is defined by

$$\eta(\theta_a) = \sqrt{\eta'_{66}\sin^2\theta_a + \eta_{44}\cos^2\theta_a} \tag{3.40}$$

where $\eta'_{66} = 0.5(\eta_{11} - \eta_{12})$, for similarity to the structure of the elastic stiffness constant. The values of the viscosity tensor of TeO_2 are not reported in the literature, but the values of the acoustic attenuation for specific orientations and modes are reported in [19]. The attenuation for the slow shear acoustic mode along [110] direction is equal to $\alpha = 19.8 dB/cm$ and along the [001] direction is equal to $\alpha = 6.8 dB/cm$ for a given frequency. Introducing the acoustic attenuation values inside Eq.3.11 and solving for $\eta_{ij}(\theta_a)$, the values of η'_{66} and η_{44} could be derived and introduced in Eq.3.11.

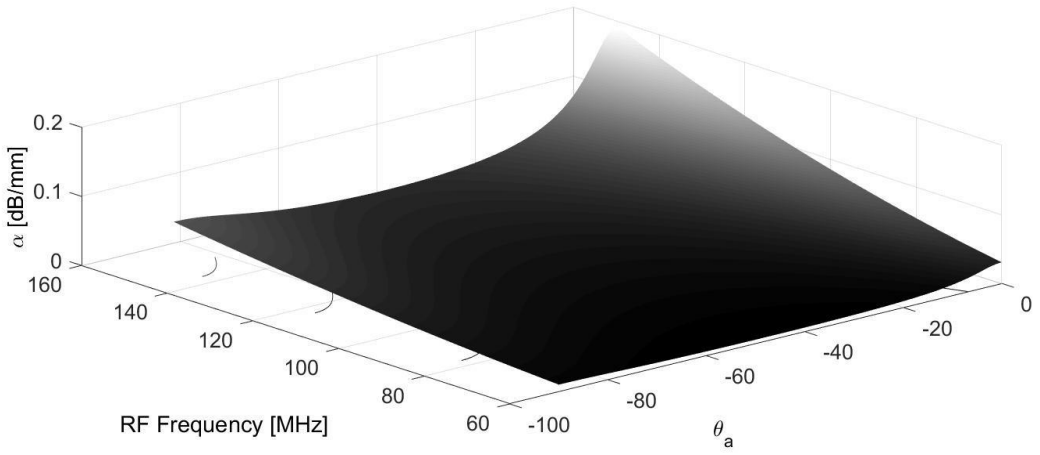

Figure 3.12: Acoustic Attenuation [dB/mm] for an arbitrary propagation (θ_a) and RF Frequency (MHz).

3.5 Mercurous Chloride (Hg_2Cl_2)

Calomel single crystal belongs to the same crystal class as TeO_2 therefore the theory developed in the previous section may be applied but with different elastic constant values. In literature the elastic stiffness constant values are $c_{11} = 1.8925 \times 10^{10} N/m^2$, $c_{12} = 1.7192 \times 10^{10} N/m^2$, $c_{13} = 1.563 \times 10^{10} N/m^2$, $c_{33} = 8.037 \times 10^{10} N/m^2$, $c_{44} = 0.8456 \times 10^{10} N/m^2$, $c_{66} = 1.225 \times 10^{10} N/m^2$.[20].

The acousto-optic interaction plane considered is the t-Z plane, thus the slowness curve (Fig.3.13(a)) for the three acoustic mode is obtained substituting the values of the relevant elastic stiffness constant into Eq.3.30 - Eq.3.31.

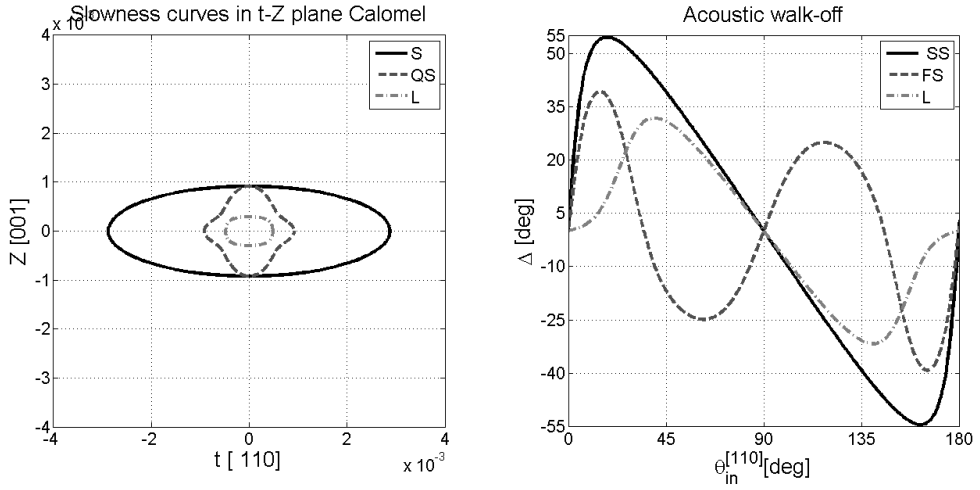

Figure 3.13: Slowness curves and Acoustic walk-off in tZ plane for Calomel Single Crystal

The minimum and maximum velocities of the slow shear acoustic waves are equal to $V_t = 384$ [m/s] and $V_z = 1084$ [m/s], respectively. Calomel is characterized by large acoustic walk-off with $\Delta_{max} = 54.23^\circ$ for $\theta = 15.52^\circ$ (Fig.3.13(b)).

3.6 Crystal Quartz

Crystal Quartz belong to the trigonal class (32) and the phase velocity is estimated by solving Eq.3.1 applying the point group symmetry:

$$[c_{KL}] = \begin{bmatrix} c_{11} & c_{12} & c_{13} & c_{14} & 0 & 0 \\ c_{12} & c_{11} & c_{13} & -c_{14} & 0 & 0 \\ c_{13} & c_{13} & c_{33} & 0 & 0 & 0 \\ c_{14} & -c_{14} & 0 & c_{44} & 0 & 0 \\ 0 & 0 & 0 & 0 & c_{44} & 0 \\ 0 & 0 & 0 & 0 & 0 & c'_{66} \end{bmatrix} \tag{3.41}$$

where $c'_{66} = (c_{11} - c_{12})/2$, with c_{66} =3.987510^{10} N/m^2, c_{14} = -1.79110^{10} N/m^2, c_{44} = 5.79410^{10} N/m^2, and $\rho = 2651$ kg/m^3. A program has been developed in Matlab to study the acoustic wave properties of crystal quartz in different planes where the acousto-optic interaction could take place. A detector of the degeneracy of the acoustic wave mode has been added to track the correct acoustic mode.

3.6.1 t-Z plane

The slowest velocity is situated on a plane rotated of $\pi/4$ about the optical axis, similar to the t-Z plane in Tellurium Dioxide and selected applying the coordinate transformation matrices Eq.A.1 and Eq.A.3 to Eq.3.41. The slowness curves of the three acoustic modes are estimated substituting the rotated elastic stiffness constant matrix in to Eq.3.1.

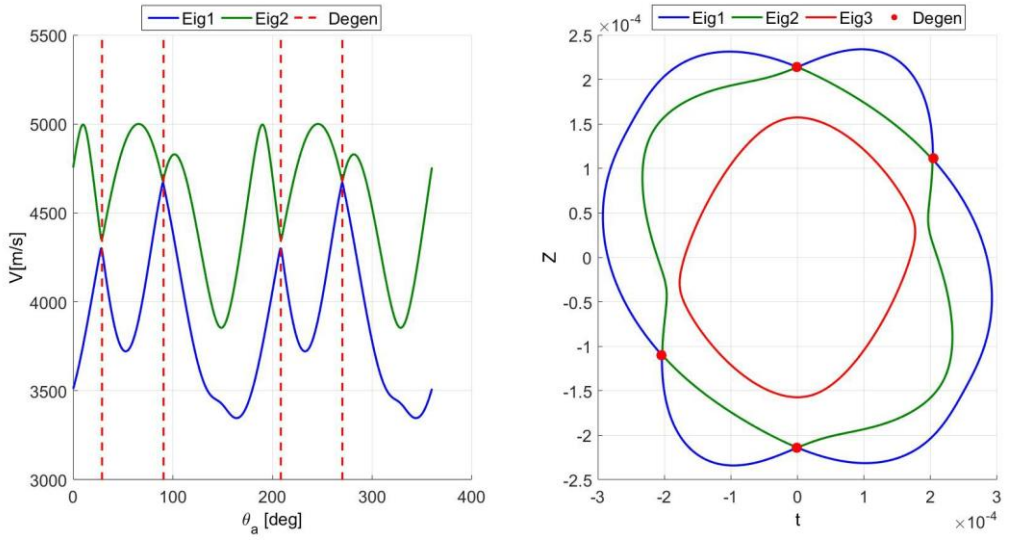

Figure 3.14: Acoustic velocity (a) and slowness curves (b) of acoustic waves in the tZ plane for crystal Quartz.

The degeneracy points of the acoustic wave were found by a dedicated Matlab routine and is marked by dashed red lines in Fig.3.14(a) and by red dots in Fig.3.14(b). Similar results were obtained for the slowness curve of other two planes rotated by 15° and 75° due to the symmetry of crystal quartz.

The tZ plane seemed a good candidate due its low acoustic phase velocity but the direction of the eigenvectors (Fig.3.15) is not matched by a conventional ultrasonic transducer, leading to an efficient coupling coefficient between the ultrasonic transducer and the AO cell.

3.6.2 XZ plane

The plane XZ has been investigated due to the symmetry to the reference axes and the degeneracy of the acoustic wave limited only in two points (Fig.3.16). The degeneracy of the slow and fast shear acoustic modes occur for $\theta_a = 90°$ and $\theta_a = 270°$.

The eigenvector directions (Fig.3.17) are not matched by conventional ultrasonic transducer. The angle ϕ_{pol} and θ_{pol} are estimated from the acoustic plane.

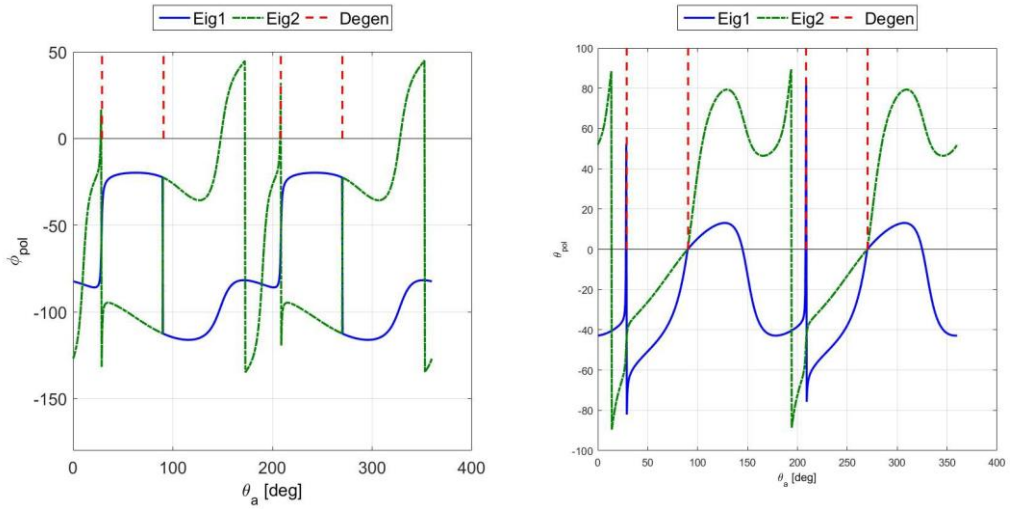

Figure 3.15: Direction of the eigenvectors of the slow shear mode in TZ plane for Quartz. ϕ_{pol} is the rotation angle out of the plane and θ_{pol} is the rotation angle into the plane.

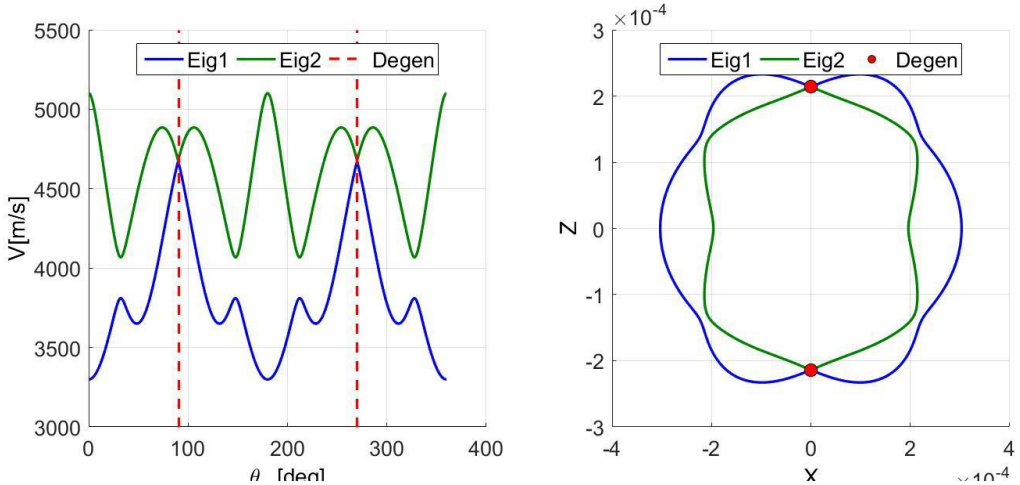

Figure 3.16: Slowness curve of acoustic wave in the XZ plane in crystal Quartz.

A conventional ultrasonic transducer could efficiently excite a pure shear acoustic wave only for $\phi_{pol} = 0^\circ$ and $\theta_{pol} = 90^\circ$.

3.6.3 YZ plane

The last plane investigated is the YZ plane, due to the symmetry of the material this plane could be selected rotating the reference axis of -30° or 90° about the Z axis. The phase velocity and the slowness curve of the slow and fast shear modes are shown in Fig.3.18, calculated by a dedicated Matlab routine.

The eigenvalues of the slow and fast shear cross in 4 points which are for θ_a equal to: 90.125°, 155.72°, 269.87°, 335.98°, and determined by the routine developed in Matlab.

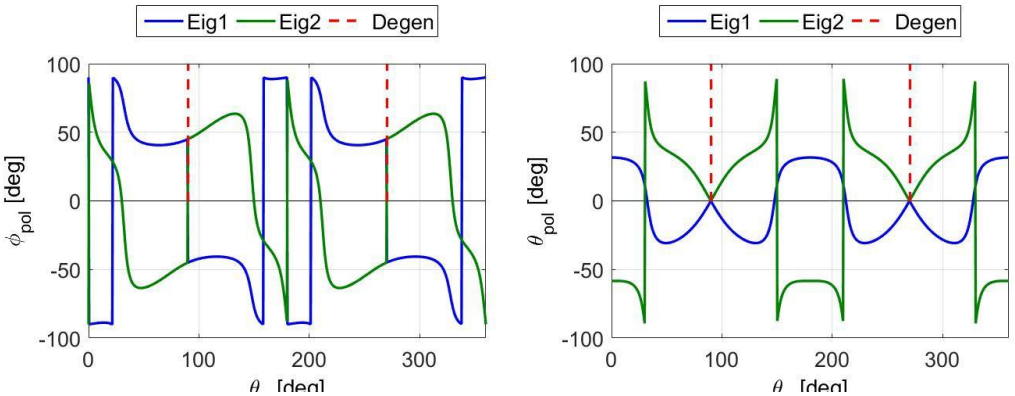

Figure 3.17: Direction of the eigenvectors of the slow shear mode in XZ plane for Quartz. ϕ_{pol} is the rotation angle out of the plane and θ_{pol} is the rotation angle into the plane.

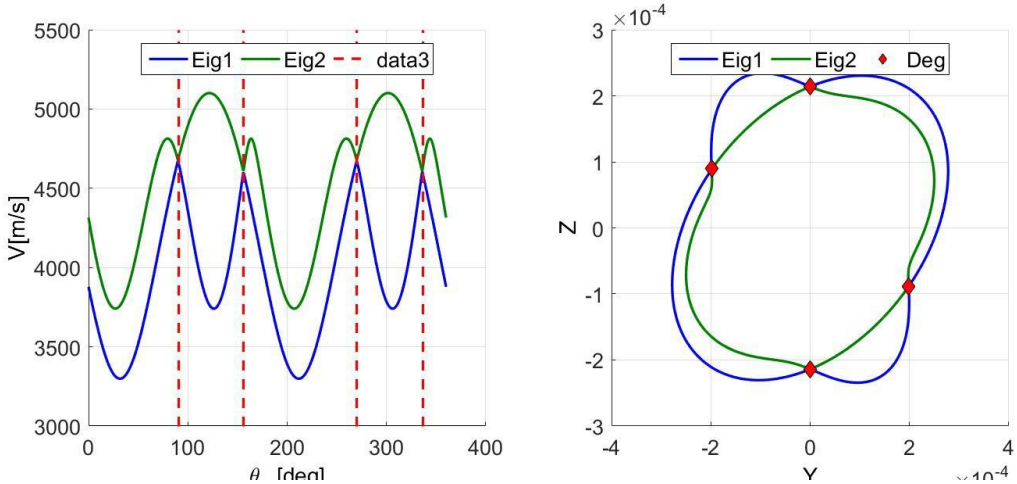

Figure 3.18: Slowness curve of acoustic wave in the XZ plane in crystal Quartz.

In order to track the correct acoustic mode a simple solution is to swap the eigenvectors in the range $90.125^\circ < \theta_a < 155.72^\circ$ and $269.78^\circ < \theta_a < 360^\circ$, but this procedure could lead to gross error in the design procedure if not applied correctly.
The eigenvector directions (Fig.3.19) are oriented perpendicular to the acoustic plane for any propagation direction of the acoustic waves, where the direction $\phi_{pol} = 90^\circ$ and $\theta_{pol} = 0^\circ$, where the switch between acoustic modes are shown at the points of degeneracy.

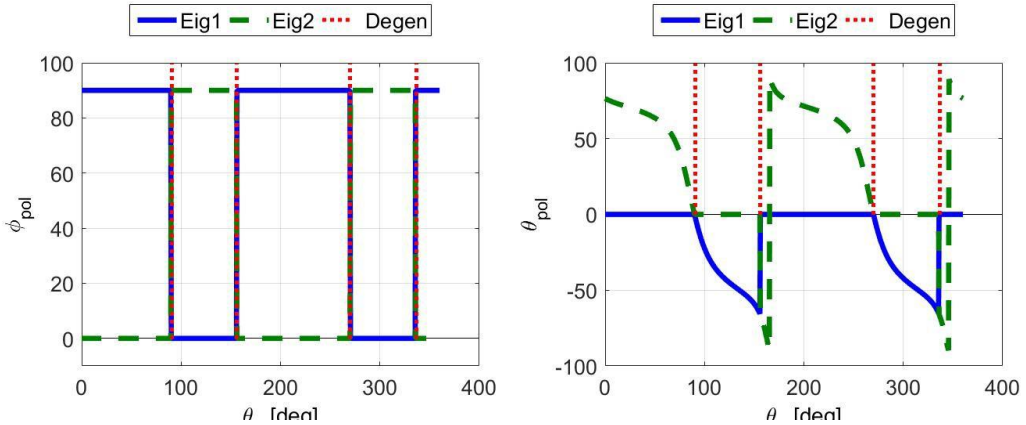

Figure 3.19: Direction of the eigenvectors of the slow shear mode in TZ plane for Quartz. ϕ_{pol} is the rotation angle out of the plane and θ_{pol} is the rotation angle into the plane.

In conclusion, the YZ plane in crystal quartz has the polarization of slow shear waves naturally perpendicular to the plane, hence an acoustic wave can be excited efficiently using conventional transducer. The direct solution of Eq.3.1 help to track the correct acoustic mode, but the estimation of the acoustic walk-off is cumbersome and difficult to introduce in the AOTF design routines. After further investigation it has been found that the slowness curve of the slow shear mode can be described by a geometrical ellipses in specific planes.

3.6.4 Approximation of the slow shear acoustic wave in YZ plane.

Here we use an approximation to simplify the calculation of the relevant (slow shear) acoustic slowness (dispersion) surface based on the same analytically simple expression, i.e. conic sections, and slices through conic sections. It was found experimentally that an ellipse has also proven to be an excellent approximation to the appropriate slice through the slowness curve for the slow shear mode, but this time it needs to be tilted. We therefore find that the acoustic slow-shear direction dependency in the YZ plane

of quartz is accurately described by:

$$V(\theta_a)^2 = V_y^2 \cos^2(\theta_a + \alpha_{rot}) + V_z^2 \sin^2(\theta_a + \alpha_{rot}) \tag{3.42}$$

where V_y = 3299.8 m/s, V_z = 5100.5 m/s, and α_{rot} = -31.6184°. The values of V_y, V_z and α has been found using a specific Matlab routine. Fig.3.20(a) shows the two eigenvalues of the slow and fast shear obtained by the Matlab solver and the superimposition from Eq.3.42. The error introduced by the approximation is within the range of ±0.0005 %. The acoustic walk-off angle (angle between phase and group velocities)

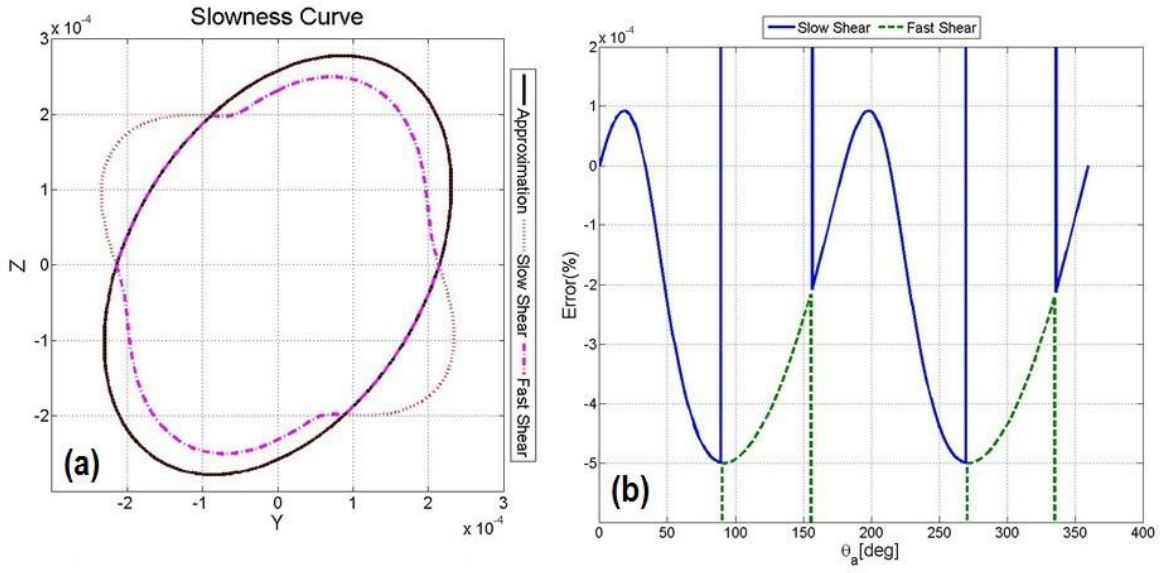

Figure 3.20: Approximation of the slowness curve of crystal quartz(a) and error introduced by the approximation (b).

is defined by Eq.3.9 and the analytical expression of the walk-off for the slow shear mode is obtained substituting Eq.3.42 (Fig.3.21):

$$\Delta = \arctan\left(-\frac{\cos(\alpha + \theta_a)\sin(\alpha + \theta_a)(V_y^2 - V_z^2)}{V_x^2 \cos^2(\alpha + \theta_a) + V_z^2 \sin^2(\alpha + \theta_a)}\right) \tag{3.43}$$

3.7 Conclusion

In conclusion this chapter was focused on the properties of the acoustic waves in anisotropic crystals. The solution of the Christoffel's equation has been investigated only for certain crystal class symmetries, which belong to the AO crystal used to build

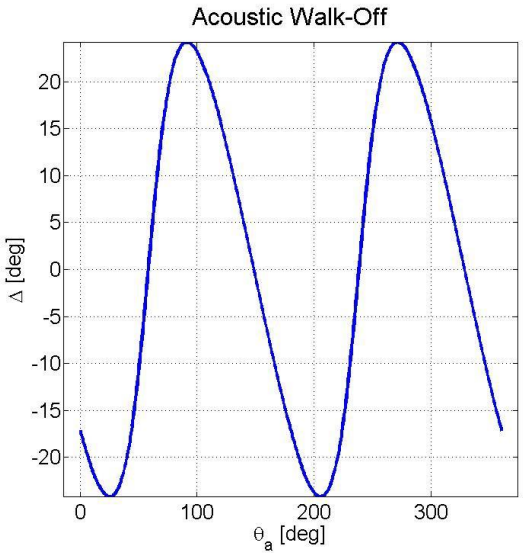

Figure 3.21: Acoustic walk-off of the slow shear mode in crystal quartz.

AO devices exploiting the slow shear interaction such as AOTFs. The analytical solution of the three acoustic mode has been found in specific planes of interest for different materials, allowing to implement them easily in Matlab codes to study the acoustic reflection of the different modes.

Tellurium dioxide and Calomel belong to the tetragonal crystal and the properties of the main crystal planes have been investigated. The direction of the axes is interchangeable thank to the high degree of symmetry in the crystal class.

In case of trigonal crystal, the positive directions of the axes have to be identified when orienting the crystals, because the identification of the correct quadrant is relevant to select the proper direction of phase velocity and related acoustic walk-off specified by the acousto-optic interaction geometry. In chapter **??** is described a procedure devised by the author in order to identify the correct quadrant by mean of piezoelectric test. This easy test allow to determine the quadrants position inside the material, which is of major importance when building an AOTF

Chapter 4

The physics of the acousto-optic interaction in anisotropic crystals.

An Acousto-Optic (AO) device is realized by bonding an ultrasonic transducer to a suitable AO material. The incident electromagnetic radiation is diffracted when specific matching conditions are satisfied. Acousto-Optic Tunable Filters exploit the slow shear AO interaction, where the acoustic propagation direction is determined by the orientation of the transducer relative to the crystallographic axes; the acoustic phase velocity is propagating in a direction as described in the previous chapter and the energy direction is estimated from the acoustic walk-off.
The different geometries of the acousto-optic interaction are investigated in this chapter from a theoretical point of view, and the results are introduced in design routines for AOTFs.

4.1 Acousto-Optics interaction under the Bragg condition.

Efficient acousto-optic interaction is obtained when the phase matching condition between acoustic waves and incident electromagnetic radiation is satisfied and described

by:

$$\mathbf{k_d}(\lambda,\ \boldsymbol{f}, \theta_a) = \mathbf{K_a}(\theta_a, \boldsymbol{f}) + \mathbf{k_i}(\lambda,\ \theta) \tag{4.1}$$

$$\mathbf{k}_{d,i} = \frac{2\pi n_{i,d}\,(\lambda,\ \theta)}{\lambda} \tag{4.2}$$

$$\mathbf{K_a} = \frac{2\pi V\,(\theta_a)}{\boldsymbol{f}} \tag{4.3}$$

where $n_{d,i}\,(\lambda)$ are the refractive index of the incident and deflected beam, $V(\theta_a)$ is the acoustic velocity, and f is the RF frequency applied to the ultrasonic transducer.
In uniaxial crystals the refractive index depends on the polarization state and on direction of incident electromagnetic radiation, conventionally the ordinary and extraordinary refractive index are related to the vertical and horizontal polarizations, respectively, where the refractive indexes surfaces are described by Eq.2.1 - Eq.2.2, which is repeated again below:

$$n_e(\theta,\lambda) = \sqrt{\frac{n_o(\lambda)n_E(\lambda)}{n_o(\lambda)^2\sin(\theta)^2 + n_E(\lambda)^2\cos(\theta)^2}}$$

where $n_o\,(\lambda)$ and $n_E\,(\lambda)$ are the refractive indices along the direction perpendicular to the optical axis, and θ is polar angle from the optical axis.
The phase matching condition described by Eq.4.1 is graphically represented in the K-space diagram (Fig.4.1), where k_i is the incident light, k_d is the first diffracted order, and K_a is the acoustic wave. In this treatment angles are defined using the polar

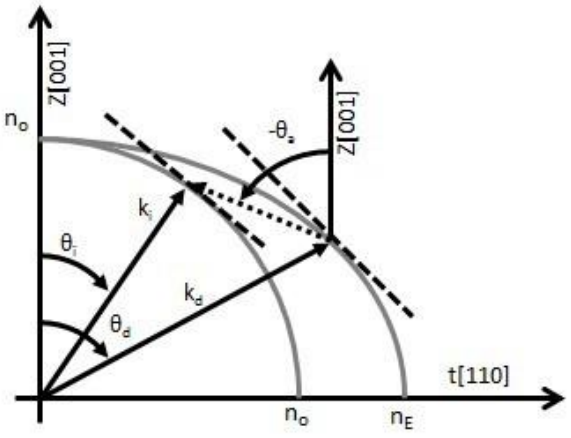

Figure 4.1: K-space diagram of an AO interaction from O to E for given wavelength in case of Tellurium Dioxide single crystal.

definition from the optical axis, thus angle rotated clockwise are considered positive and counter-clockwise are negative.
An AO interaction from ordinary to extraordinary polarization is defined as "EO" and

viceversa "OE" defines the AO interaction from extraordinary to ordinary polarization. From Eq.4.1 it is possible to define the tuning relation, which is the relation between RF frequency applied to the transducer and the wavelength of the diffracted order for broadband incident light.
The general solution of the phase matching condition is defined by applying simple geometrical calculation in the space diagram:

$$n_d(\lambda)(\tan\theta_a \cos\theta_d - \sin\theta_d) = n_i(\lambda)(\tan\theta_a \cos\theta_i - \sin\theta_i) \tag{4.4}$$

where n_d, n_i, θ_i and θ_d are defined by the specific AO interaction. The relation between RF frequency applied to the ultrasonic transducer and the wavelength of the diffracted order, is known as the tuning relation, is defined by a simple vector subtraction and confirmed by Gass[21]:

$$\lambda = \frac{V(\theta_a)}{f}\sqrt{n_i(\lambda)^2 + n_d(\lambda)^2 - 2n_i(\lambda)n_d(\lambda)\cos\theta_{sep}} \tag{4.5}$$

where $\theta_{sep} = \theta_i - \theta_d$ is the separation angle, with the deflection angle (θ_d) of the 1^{st} diffracted order obtained from Eq.4.4 for a given wavelength when θ_i, and θ_a are defined. An infinite number of configuration of the AO interaction exists, but in practice some constraints are applied in order to optimize one of the parameters in real devices such as: resolution, field of view, RF drive power versus diffraction efficiency etc. The main categories of AO interaction are:

- the **non-collinear interaction**, where the acoustic field is transverse to the optical beam
- the **collinear interaction**, where the energy direction of the acoustic field is collinear with the optical beams

Different mathematical models have been develop and introduced in routines to help the prototyping process of new devices and the characterization of current devices, where two different programming languages have been used: Matlab and Python.

4.1.1 Non-collinear interaction

The non-collinear interaction is obtained when the acoustic field intersects obliquely with the incident electromagnetic radiation. This configuration is typically used with an additional constraint known as the parallel tangent matching condition, which is

characterized by a large field-of-view and is typically used for non coherent sources. The *parallel tangent matching condition* firstly reported by Chang [22] and defined as:

$$\tan\theta_d = \left(\frac{n_d}{n_i}\right)^2 \tan\theta_i \tag{4.6}$$

where the tangents to refractive index surfaces are parallel for the incoming and diffracted light, thus a constraint between θ_i and θ_d is set. Introducing the condition of Eq.4.6 in to Eq.4.4 it is possible to determine the input direction for an arbitrary propagation of the phase velocity of the acoustic wave. The phase matching condition was derived by author for a given θ_a, and the input angle of the electromagnetic radiation:

$$\tan\theta_a = \frac{\left(\frac{n_E}{n_o}\right)^2 \tan\theta_i - \sin\theta_i \sqrt{1 + \frac{n_E^2}{n_o^2}\tan^2\theta_i}}{1 - \cos\theta_i \sqrt{1 + \frac{n_E^2}{n_o^2}\tan^2\theta_i}} \tag{4.7}$$

from the solution of the above equation is possible to determine θ_i and consequently θ_d using Eq.4.6, which once introduced in Eq.4.5 allows to determine the tuning relation of the AO interaction for a given wavelength. In practice θ_i obtained from Eq.4.7 varies with the wavelength due to the dispersive nature of the refractive index, theoretical investigation shows the change on θ_i is limited and accentuated in the visible region as expected. The phase matching condition problem has been solved defining the acoustic direction to determine the required variation of θ_i to always achieve phase matching. The phase matching condition could also be solved by defining θ_i and solving Eq.8.1 using condition of Eq.4.6, from this solution is possible to determine the range of θ_a where the parallel tangent matching condition is satisfied for a given wavelength.

4.1.2 Quasi-collinear AO interaction

The Quasi-Collinear (QC) AO interaction is obtained when the energy direction of the acoustic field is parallel to the propagation of the electromagnetic field [23][24]. Two different approaches can be used when studying this configuration, the first approach is to define the incident direction of the electromagnetic wave and the acoustic wave direction is determined using a mathematical routine or by graphical solution. The other approach is to define the acoustic direction, then the propagation of the incident electromagnetic radiation is defined by [6]:

$$\theta_i = \Delta(\theta_a) + \theta_a \tag{4.8}$$

where Δ is given by Eq.3.9 depending on θ_a. The tuning relation is estimated by Eq.4.5, once the deflection angle of the first diffracted order is derived by the solution of Eq.4.4.

This type of AO interaction is conventionally used to achieve long interaction length when a narrow bandwidth filter with low RF power is required. This configuration particularly allows a long interaction length in an AOTF made of TeO_2, because the crystal naturally grows along the [110] direction allowing long crystal along the desired direction.

4.1.3 Efficiency of AO interactions

The efficiency of the AO interaction is proportional to the RF power applied to the ultrasonic transducer, when the phase matching condition is satisfied, and theoretically it can be estimated by [6]:

$$\eta = \sin^2\left[\frac{\pi}{\lambda_0}\sqrt{\frac{M_2 L_a}{2H}P_a}\right] \tag{4.9}$$

where H is the height of the acoustic field, defined by the electrode size on the ultrasonic transducer, L_a is the interaction length, P_a is the RF power, λ_0 is the wavelength of the diffracted order and M_2 is the acousto-optic figure of merit. The RF power for Peak Diffraction Efficiency (PDE) for a given wavelength is estimated theoretically by solving Eq.4.9 for $\eta = 1$:

$$P_{PDE} = \frac{H\lambda^2}{2L_a M_2} \tag{4.10}$$

The RF power for PDE depends on λ^2, and it is inversely proportional to the acousto-optic figure of merit

$$M_2 = \frac{n_i^3 n_d^3 p_{eff}^2}{\rho V(\theta)^3} \tag{4.11}$$

where p_{eff} is the effective photoelastic constant, $V(\theta)$ is the phase velocity of the acoustic wave, ρ is the density and $n_{i,d}$ are the refractive indices of the incident and diffracted orders. In order to optimize the RF power vs. Diffraction Efficiency (DE) for a given wavelength, one should maximize M_2 maximizing, i. e. the ratio p_{eff}^2/V^3. The effective photoelastic constant is obtained from tensorial equation, therefore it is related to the geometry of the AO interaction. A general expression of the p_{eff} was determined in order to maximize the M_2.

4.1.4 Determination of the effective photoelastic constant

The effective photoelastic constant is defined as [6]:

$$p_{eff} = \left[\hat{e}_I^{(m,m-1)}\right][P_{IJ}]\,[S_{IJ}] \tag{4.12}$$

where P_{ij} is the photoelastic tensor, which is material dependent, S_{ij} is the strain tensor related to the acoustic wave and

$$\hat{e}_I^{(m,m-1)} = \hat{e}_i^{(m-1)}\hat{e}_{iI}^{(m)} \tag{4.13}$$

is the polarization direction of the incident electromagnetic wave defined as:

$$\hat{e}_{iI}^{(m-1)} = \left[\begin{array}{ccc|ccc} e_1^{(m-1)} & 0 & 0 & 0 & e_3^{(m-1)} & e_2^{(m-1)} \\ 0 & e_2^{(m-1)} & 0 & e_3^{(m-1)} & 0 & e_1^{(m-1)} \\ 0 & 0 & e_3^{(m-1)} & e_2^{(m-1)} & e_1^{(m-1)} & 0 \end{array}\right] \tag{4.14}$$

which has similar structure to l_{iK} (Eq.3.2), where m is the number of the diffracted order. The generic polarization vector is defined as:

$$\hat{e}_i = [\cos(\theta)\cos(\phi),\ \cos(\theta)\sin(\phi), \sin(\theta)] \tag{4.15}$$

with Fig.4.2 as a reference, where the angle are measured from the X direction, in this case the polar angle convention is not used. The acoustic and optical field are treated separately when solving Eq.4.12.[6]

The photoelastic tensor depends on the crystal class and its structure is identical to the elastic stiffness tensors, with the following condition applied to the photoelastic constant[6]:

$$p_{ij} /= p_{ji}$$

where the compact notation is introduced thanks to the crystal symmetry, which is generally applied to all the AO materials examined in this thesis. The effective photoelastic constant is derived for the trigonal class due the low symmetry and the solution obtained is applied to other classes with higher symmetry, such as tetragonal and cubic.

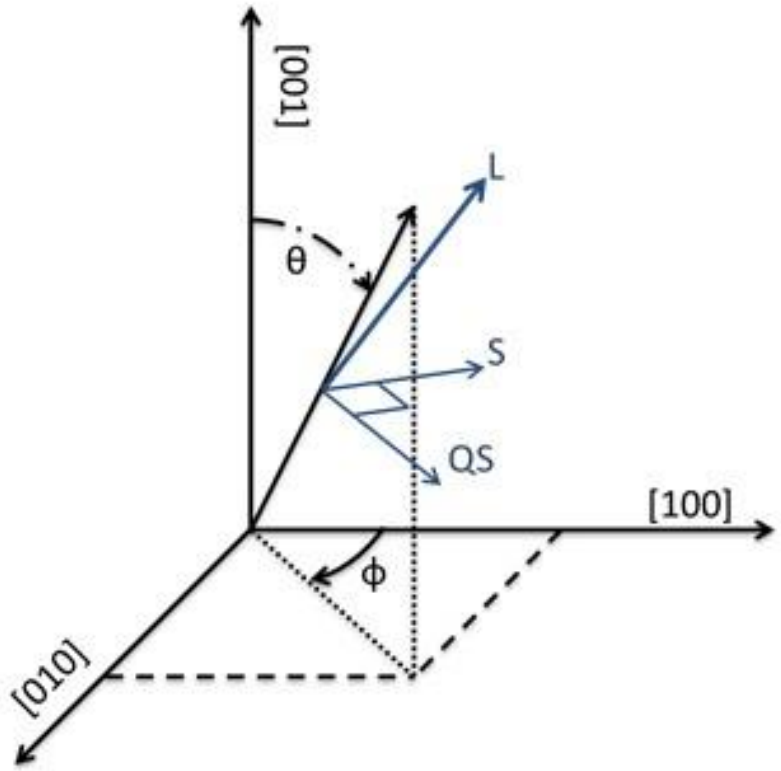

Figure 4.2: Rotation angle for reference axis.

4.1.5 Effective photoelastic constant in trigonal crystal: 32,3m, $\bar{3}$m

The general expression of the effective photoelastic constant is derived for the birefringent slow shear interaction in trigonal crystals, where the AO interaction takes place in the Y-Z plane and the polarization of the acoustic wave is perpendicular to the former. The photoelastic constant matrix [6] in the main reference axis X[100]-Y[010]-Z[001] is

$$P_{IJ} = \begin{bmatrix} p_{11} & p_{12} & p_{13} & p_{14} & 0 & 0 \\ p_{12} & p_{11} & p_{13} & -p_{14} & 0 & 0 \\ p_{31} & p_{31} & p_{33} & 0 & 0 & 0 \\ -p_{41} & p_{41} & 0 & p_{44} & 0 & 0 \\ 0 & 0 & 0 & 0 & p_{44} & 0 \\ 0 & 0 & 0 & 0 & 0 & p_{66} \end{bmatrix} \tag{4.16}$$

where $p_{66} = 0.5(p_{11} - p_{12})$.

In order to estimate p_{eff} two different approaches may be used, one is to rotate the strain tensor (S_J) and the optical polarization vectors ($\hat{e}_I^{(m,m-1)}$) in the reference axis of the photoelastic matrix [6]; this approach requires several rotation of the reference

axis and it is useful to determine p_{eff} for specific case. Ultimately the results obtained cannot easily be extended to a generic geometry of the AO interaction in a specific plane and the implementation of such solutions in design routines is of difficult optimization. An alternative method to determine p_{eff} is to align P_{IJ} to the acoustic direction by means of the coordinate transformation matrices Eq.A.1 for this specific case.
The photoelastic constant matrix $[P_{IJ}]$ has to be aligned to the direction of the phase velocity obtained by applying the coordinate transformation matrix $\mathrm{M}_x(\phi)$, therefore the new photoelastic constant matrix is estimated by

$$[P_{ij}^{'}(\psi)] = [M_x(\psi)][P_{ij}][M_x(\psi)]^T \tag{4.17}$$

where M_x is defined by A.1 and

$$\psi = \pi/2 - \theta_a \tag{4.18}$$

with θ_a measured from the optical axis. The strain components (S_{ij}) of a slow shear wave propagating along the Y direction and x-polarized is defined by:

$$S_J = \begin{matrix} \\ \mathrm{S1} \\ \mathrm{S2} \\ \mathrm{S3} \\ \mathrm{S4} \\ \mathrm{S5} \\ \mathrm{S6} \end{matrix} = \begin{matrix} \\ 0 \\ 0 \\ 0 \\ 0 \\ 0 \\ 1 \end{matrix} \tag{4.19}$$

with the abbreviated subscript notation [17]. If the birefringent AO interaction from ordinary to extraordinary polarization is considered, then the input polarization is perpendicular to the plane of the AO interaction is defined by:

$$\hat{e}_i^{(0)} = [1, 0, 0] \tag{4.20}$$

from the definition given in Eq.4.15, and is independent to the propagation direction. Consequently the output polarization lays on the plane of the AO interaction and depends on the propagation of the first order (Fig.4.3) defined by the deflection angle of the first order (θ_d), thus the polarization vector of the first order is defined by:

$$\hat{e}_{iI}^{(1)} = [0, \sin\theta_d, \cos\theta_d] \tag{4.21}$$

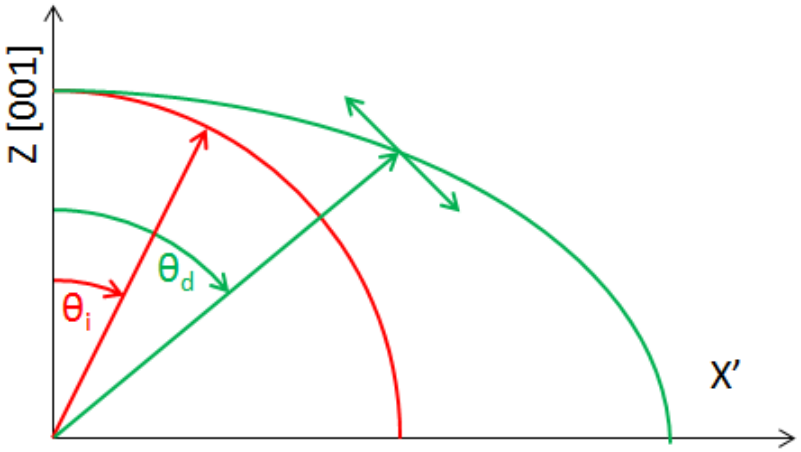

Figure 4.3: Optical polarization of 0^{th} and 1^{th}

The expression of $\hat{e}_I^{(m,m-1)}$ required in Eq.4.12 is obtained introducing Eq.4.21 and Eq.4.14 in to Eq.4.13:

$$\hat{e}_I^{(1,0)} = [0, 0, 0, 0, \cos\theta_d, \sin\theta_d] \tag{4.22}$$

in case of Bragg diffraction (m = 1).

The analytical expression of p_{eff} for an arbitrary direction of the acoustic wave is obtained introducing Eq.4.17 and Eq.4.22 in to Eq.4.12 and is defined by:

$$p_{eff} = \cos\theta_d \left[p_{66}\cos^2\psi + p_{44}\sin^2\psi + \sin 2\psi \frac{p_{14} - p_{41}}{2} \right] + \\ + \sin\theta_d \left[p_{41}\cos^2\psi - p_{14}\sin^2\psi - \sin 2\psi \frac{p_{44} - p_{66}}{2} \right] \tag{4.23}$$

where the values of the photoelastic constants are material dependent, and θ_a and θ_d are defined by the AO interaction.

The expression in Eq.4.23 is valid only for the AO interaction from ordinary to extraordinary, but the results obtained could be extended for the AO interaction from extraordinary to ordinary. In this case the input polarization depends on the incident propagation θ_i, then Eq.4.20 becomes

$$\hat{e}_i^{(0)} = [0, \sin(\theta_i), \cos(\theta_i)] \tag{4.24}$$

and Eq.4.14 simplifies to:

$$\hat{e}_{iI}^{(0)} = \begin{bmatrix} 1 & 0 & 0 & 0 & 0 & 0 \\ 0 & 0 & 0 & 0 & 0 & 1 \\ 0 & 0 & 0 & 0 & 1 & 0 \end{bmatrix} \tag{4.25}$$

introducing the above equation in to Eq.4.25, which becomes:

$$\hat{e}_{I}^{(1,0)} = [0, 0, 0, 0, \sin(\theta_i), \cos(\theta_i)] \tag{4.26}$$

comparing the above equation to Eq.4.22 consequently the values of the effective photoelastic constant is obtained substituting θ_d to θ_i

$$\begin{aligned} p_{eff} = \cos\theta_i \left[p_{66}\cos^2\psi + p_{44}\sin^2\psi + \sin 2\psi \frac{p_{14} - p_{41}}{2} \right] + \\ + \sin\theta_i \left[p_{41}\cos^2\psi - p_{14}\sin^2\psi - \sin 2\psi \frac{p_{44} - p_{66}}{2} \right] \end{aligned} \tag{4.27}$$

The general solutions of Eq.4.23 and Eq.4.27 have been implemented in the AOTF design routine.

4.1.6 Effective photoelastic constant in tetragonal crystal: 4mm,422,42m,4/mmm

Tetragonal crystals have the following photoelastic constant matrix

$$(P_{IJ}) = \begin{bmatrix} p_{11} & p_{12} & p_{13} & 0 & 0 & 0 \\ p_{12} & p_{11} & p_{13} & 0 & 0 & 0 \\ p_{31} & p_{31} & p_{33} & 0 & 0 & 0 \\ 0 & 0 & 0 & p_{44} & 0 & 0 \\ 0 & 0 & 0 & 0 & p_{44} & 0 \\ 0 & 0 & 0 & 0 & 0 & p_{66} \end{bmatrix} \tag{4.28}$$

for the reference axis X[001] - Y [010] - Z[001]. The tetragonal crystals used in AO applications are tellurium dioxide and calomel single crystals, where the plane of the AO interaction is the t[110]-Z[001] plane. Then the photoelastic constant matrix requires a rotation of $\theta = \pi/2$ about the optical axis to align the reference axis to the AO interaction plane using $M_z(\theta)$ (Eq.A.3), and a rotation equal to ϕ about $\hat{t}\,[1\bar{1}0]$ direction

to align along the acoustic wave propagation using $M_y(\phi)$ (Eq.A.1.
The photoelastic constant matrix in the new reference frame is determined by:

$$[P_{ij}^{'}] = [M_y][M_z][P_{ij}][M_z]^T[M_y]^T. \tag{4.29}$$

The effective photoelastic constant is estimated by introducing Eq.4.29 in Eq.4.12 using Eq.4.22 in case of an AO interaction $\mathbf{OE}^+$

$$p_{eff} = p_{44}\cos\theta_a \sin\theta_d - p_{66}^{'}\sin\theta_a\cos\theta_d \tag{4.30}$$

For the case of the AO interaction $\mathbf{EO}^+$, the effective photoelastic constant is obtained from the substitution of θ_d with θ_i in Eq.4.30

$$p_{eff} = p_{44}\cos\theta_a \sin\theta_i - p_{66}^{'}\sin\theta_a\cos\theta_i \tag{4.31}$$

where θ_a,θ_i, and θ_d are obtained from the AO interaction configuration and

$$p_{66}^{'} = \frac{p_{11} - p_{12}}{2} \tag{4.32}$$

The general expressions of p_{eff}, defined in Eq.4.23 - Eq.4.27 for trigonal crystals and in Eq.4.30 - Eq.4.31 for tetragonal crystals, are used to estimate the acousto-optic figure of merit (M_2) for a given AO interaction.

4.2 Conclusion

The geometry and the efficiency of the acousto-optic interaction has been introduced in this chapter and the results have been specialized for two different class of symmetry trigonal and tetragonal. The geometry is defined by the phase matching condition between the acoustic field and the incident electromagnetic radiation and the AO interaction could be separated in two groups, quasi-collinear and non-collinear, identified by the relation between acoustic and optical waves direction.
The analytical expression of the effective photoelastic constant was derived for the trigonal crystal class only because this solution can be applied to tetragonal crystal setting $p_{14} = p_{41} = 0$.
AOTFs are designed under the parallel tangent matching condition [25] investigated for non-collinear configuration, where the acceptance angle is maximize. The collinear interaction instead is obtained when the acoustic walk-off and incident electromag-

netic radiation propagate along the same direction, therefore the achievable interaction length is maximize giving a narrow passband and low RF power requirement to achieve peak diffraction efficiency.

The results obtained in this chapter are introduced in design routines realized in Matlab and Python for crystalline materials described in Ch.2.

Chapter 5

AOTF in the wavelength range: 380 nm - 4.5 μm

5.1 Introduction

Acousto-Optic Tunable Filters in the wavelength range between 380 nm and 4.5 μm are conventionally realized using Tellurium Dioxide (TeO_2), which has a high M_2 and is available in crystals of large dimension with good quality. The configuration of the AO interaction is dictated by specific application, defined by: wavelength range, acceptance angle as described in the previous chapter. Two different configurations are typically used: the quasi-collinear interaction is used to achieve narrow pass-band and to reduce the RF power versus diffraction efficiency maximizing the interaction length at the expense of the field of view; this configuration is used for example in case of line selection applications and single point detector systems.

The non-collinear interaction under the parallel matching condition maximises the field of view at the expense of the interaction length, which determines the relation between RF power and diffraction efficiency. The RF power to achieve peak diffraction efficiency depends on the square of the filtered wavelength in the first approximation, thus a high level of RF power is required for wavelengths above 2 μm. Under high RF power operation, AO devices are affected by elevated thermal gradients altering the operational condition such as tuning curve shift, and changes on the passband.

In order to reduce the RF power for peak diffraction efficiency a solution is proposed in this chapter by means of a resonant acoustic cavity. The performance of conventional AOTFs are compared to the resonant AOTF both theoretically and experimentally.

5.2 Large aperture AOTF

Large aperture AOTFs are typically used as tunable filters for imaging systems or when a large etendue is required due to the spectral properties of the source or the target. A large field of view is achieved when the parallel tangent matching condition (Eq.4.6) is applied as described in Sec.4.1.1.
High quality crystals with linear dimensions larger than 30 mm are difficult to grow and processing significantly increases the cost of the final device. Therefore the design process is a trade-off between specification and cost, with the following limiting factors:

- the RF frequency range of the tuning relation is defined by the wavelength range and the incident angle
- the RF power for peak diffraction efficiency is set by the ratio of the electrode size and filtered wavelength
- the bandpass required by the application, is a function of the interaction length, and θ_i
- the angular separation between the 0^{th} and 1^{st} order is related to the RF frequency, wavelength and crystal orientation
- the homogeneity of the acoustic power across the aperture is limited by the attenuation of the acoustic wave
- the AO crystal dimension should be as small as possible to achieve competitive costs and simplify the manufacturing process.

A series of design routines developed in Matlab and Python have been created to predict and optimize the AOTF design.
The general solution of the AO interaction under the parallel tangent matching condition is investigated in the next section.

5.3 Trade-off between the different specification of an AOTF

The trade-offs between the performance are dictated by the applications. If the parallel tangent matching condition is applied to the AO interaction configuration, then it is

possible to estimate the acoustic direction, the interaction length, the acoustic attenuation and the acousto-optic figure of merit for any incident direction θ_i for a given wavelength. The relation between θ_a and θ_i applying Eq.4.6 is shown in Fig.5.1 for 450 nm < λ < and 4.5 μm examining both the AO interaction type, **EO+** and **OE+**.

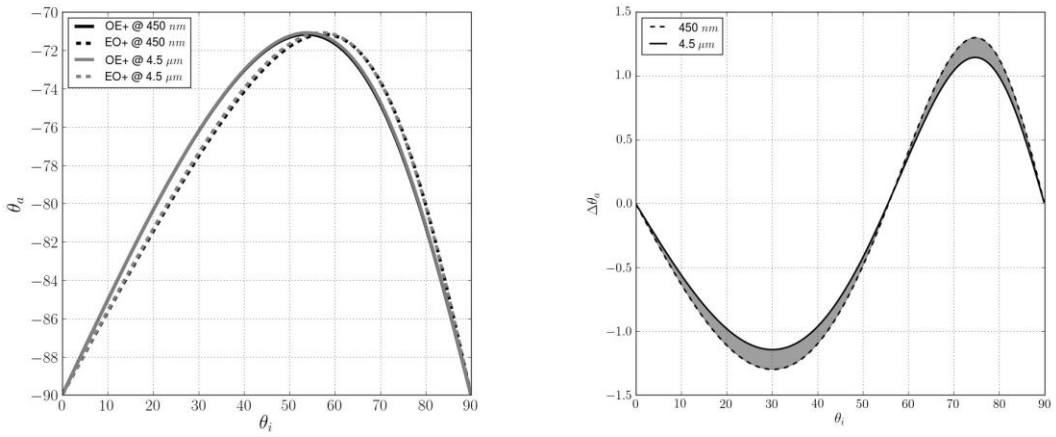

Figure 5.1: Angle relation between θ_i and θ_a under parallel tangent matching condition for two wavelength with different incident polarization(left) $\Delta\theta_a$ between the two different type of AO interactions(right).

The acoustic direction has to change with θ_i in order to satisfying the phase matching condition (Fig.5.1). The phase matching condition effects the AO configuration under parallel tangent matching condition; in general it is not possible to satisfy the parallel tangent matching condition for both polarizations, unless for a given specific direction of θ_i, where the curves cross.

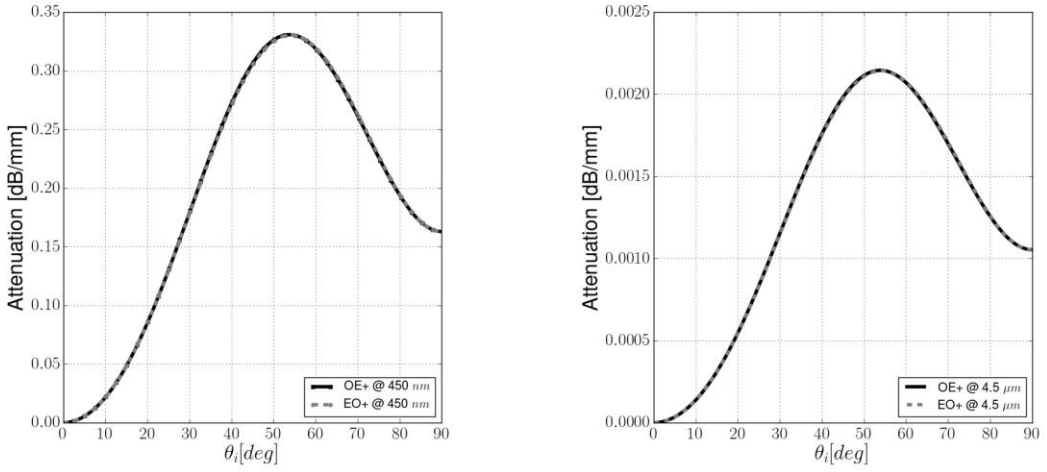

Figure 5.2: Acoustic attenuation for λ = 450 nm (left) and λ = 4.5 μm (right).

Once the geometry of the AO interaction is defined, then the variation of the acousto-optic figure of merit (M_2) is estimated by Eq.4.30 and Eq.4.31 for both type of AO

interaction respectively and shown in Fig.5.3; the RF frequency required to achieve phase matching conditions for an arbitrary direction of θ_i is shown Fig.5.3.
In addition the acoustic attenuation depends on θ_i and on the f^2, therefore one should select a low θ_i. This dependency is shown in Fig.5.2 for an arbitrary direction of θ_i, which is related to θ_a.
The RF power for peak diffraction efficiency and the passband is defined by the interaction length (L_a), which depends on θ_i and the acoustic walk-off as shown in Fig.5.4.
The trade-off between the different specification is obtained from the solution of the AO configuration for an arbitrary θ_i, from the theoretical point of view the phase-matching condition is satisfied for any θ_i as shown Fig.5.1. From the practical point of view only a limited interval can be used to design real devices, because M_2 decreases with increasing θ_i (Fig.5.3) and the interaction length decrease with θ_i increasing the RF power for Peak Diffraction Efficiency (PDE). The RF frequency increase with θ_i (Fig.5.1) and consequently the acoustic attenuation (Fig.5.2), therefore the intensity of the acoustic field will be strongly dependant on the propagation distance from the transducer.

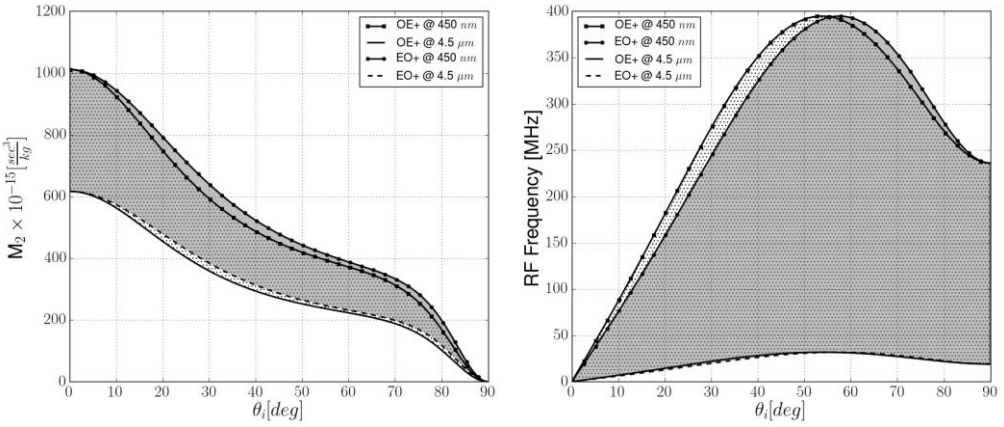

Figure 5.3: Variation of M_2 with theta$_i$ (left) and frequency range (right) to achieve phase matching condition for both type of AO interaction for the wavelength range of transparency of TeO_2 under parallel tangent matching condition.

An arbitrary limit to the RF power of 5 W in TeO_2 is assumed in order to avoid strong temperature gradients inside the AO cell. At such a level of RF power the heat generated by the acoustic attenuation will affect the accuracy of performance predictions due to the temperature dependency of the acoustic velocity and of the refractive indices. In addition the lifetime of the device is affected by repeated temperature cycling, and in extreme cases could lead to cracking in the AO medium due to the difference of the coefficients of the thermal expansion; this limit is easily reached at long wavelength ($\lambda > 2\ \mu$m), due to the inherent elevated drive power.
A limitation on the RF frequency has to be applied due to the acoustic attenuation

and broadband matching condition, thus a maximum and a minimum RF frequency have been set to between 15 MHz and 150 MHz.

The low RF frequency limits the tuning range achievable with a standard matching network. In the case of high frequency (f> 150 MHz), an octave is broad enough to easily allow broad band matching, but the bonding process requires tight tolerance on layer deposition.

The higher frequencies are typically related to the shorter wavelengths, where the RF power for peak diffraction is inherently low, but the acoustic attenuation will dominate the performance of the AOTF. In the case of an RF signal above about 120 MHz the complexity of the matching network will increase significantly due to the uncertainty at the manufacturing level (such as the bond thickness, and also wire-bonds etc…) limiting the tuning range. The lower limit is mainly due to limitation on the tuning range due to the absolute range corresponding to 1 octave.

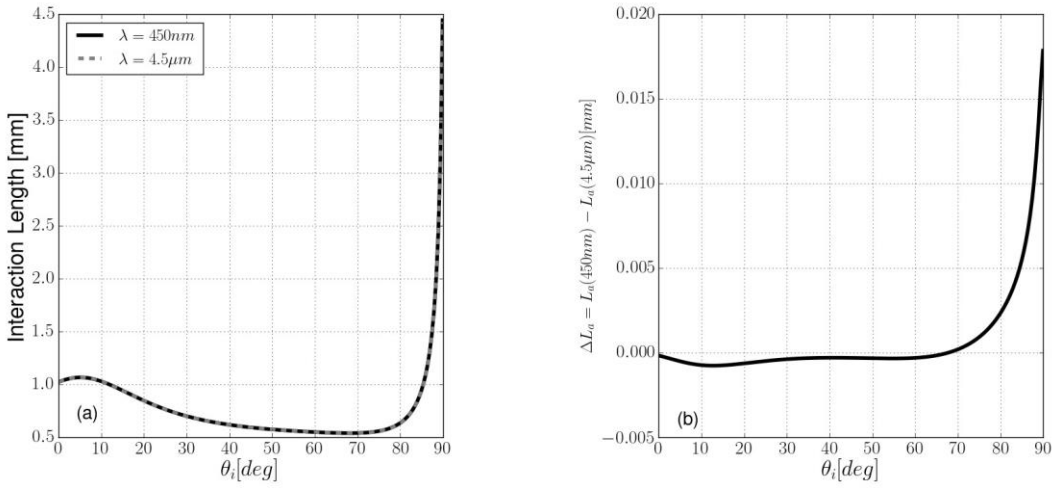

Figure 5.4: Interaction length variation with θ_i for an electrode of 1 mm (left) difference on interaction length between 450 nm and 4.5 μm (right).

In conclusion, large aperture AOTFs could be subdivided in two main wavelength ranges: one between 380nm < λ < 1 μm and the second one is between 1 μm < λ < 4.5 μm, where different trade-offs are applied during the design process, and described in detail in the next sections.

5.3.1 Wavelength range from UV up NIR (< $1\mu m$)

The wavelength range from 450 nm up to 1000 nm is of particular interest on different application such as remote sensing [26], cytologist[27], and other applications where a fast tunable filter is required with narrow bandwidth [28]. The field of view is maximized when the parallel tangent matching condition is applied to the AO interaction

configuration, which introduces constraints on the choice of θ_i.
The arbitrary limitations on the maximum RF frequency and RF power introduced in the previous section, set an interval of θ_i, where the trade-off between passband, tuning range and RF power consumption meet the required specification defined by the application. In order to optimize the AOTF performance the relation between θ_i and θ_d is given by Eq.4.6 and defines the AO interaction geometry for a given wavelength. If the input direction is considered between 0 and $\pi/2$, then the acoustic direction to achieve phase matching is given by Eq.4.4 and shown in Fig.5.1. The RF frequency

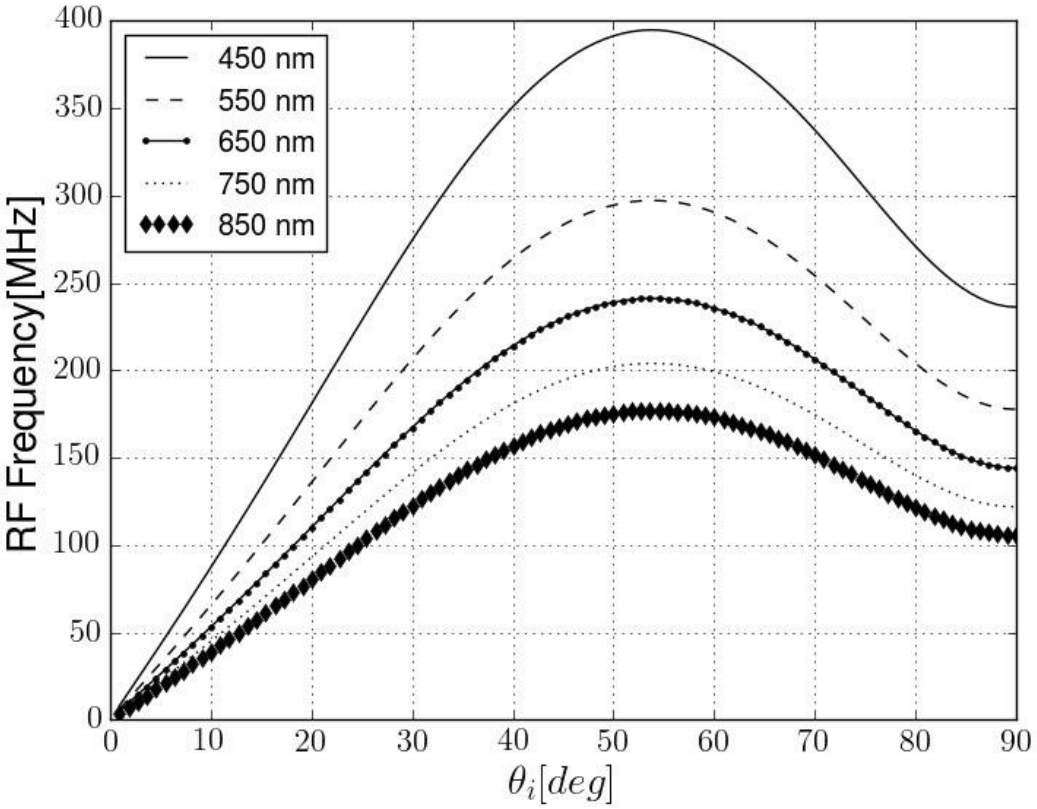

Figure 5.5: RF Frequency for an arbitrary input direction under the parallel tangent matching condition for different wavelengths.

dependency to θ_i and λ is defined by Eq.4.5, which shows inherently high frequencies in the wavelength range up to 850 nm. If the RF frequency limit is applied then only a small interval of θ_i between 10.0 $^\circ$ and 20.0 $^\circ$ could be selected; for $\theta_i < 10^\circ$ the RF frequency is significantly reduced at the expenses of the wavelength range covered due to the low centre frequency and the effects of optical activity need to introduced.
Close to the optical axis the polarization state of the incident light should be elliptical in order to achieve peak diffraction efficiency, and the ellipticity of the polarization depends on the wavelengths selected by the RF frequency and on the optical path inside the AO crystal due to the dispersive nature of the optical activity.

The elevated RF frequency affects the acoustic power across the aperture. The diffraction efficiency across the aperture is reduced in large aperture AOTF, because the acoustic attenuation in TeO_2 increases with f^2, giving a variation in the DE across the aperture. Non-Collinear AOTFs are available from a number of manufacturers for the wavelength range covering 450 nm and 2 μm.

5.3.2 Wavelength range from 1μm to 4.5 μm

The RF power needed to achieve peak diffraction efficiency is theoretically evaluated by Eq.(8.11), which increases with λ^2 and reduced by maximizing the ratio L_a/H. The dimension of the optical face is determined by the field of view required and by the available dimension of the crystal, therefore a trade-off is required between the field of view and the interaction length achievable. The wavelength region between 1μm and 4.5μm is of particular interest for many applications and the availability of super-continuum sources covering this range is pushing the effort to extend the wavelength range to the very limit of the transparency range of Tellurium Dioxide. NKT Photonics for example is developing a source covering the wavelength range above 2 μm within the MINERVA Project (FP-7), consequently AOTFs are the typically used due to the fast random access capability and narrow bandwidth. The wavelength range is characterized by elevated RF power for peak diffraction efficiency in case of non-collinear interaction. Two possible solutions to reduce the RF power requirement are: increase the interaction using a quasi-collinear configuration at the expense of the field of view; or to configure the AO cell as an acoustic resonant cavity increasing the acoustic power available inside the AO medium. Another possible solution is to find a more suitable material, but this task has proved very problematic over 3 decades of research.
The quasi-collinear configuration is typically selected for line selection application due to its narrow passband and low RF power, hence this configuration is particularly suitable for filtering wavelength above 2 μm, the narrow field of view and diffracted limited beam requirement limit the use of this configuration, when the spatial coherence of the source is high (Beam quality as measured by M2 <1.5 [29]).
The non-collinear configuration is a more suitable solution due to the large acceptance angle, but at the expense of a higher RF power for peak diffraction efficiency and broader pass-band due to a shorter interaction length, consequently high level of RF power (> 5 W) is required; under this operational condition some practical limitations (e.g. temperature gradient, power handling) rise for operational wavelength above 2μm.

It is possible to predict the RF power dependencies of the diffraction efficiency for a given ratio of the interaction length and optical face by using Eq.4.9 for a specific

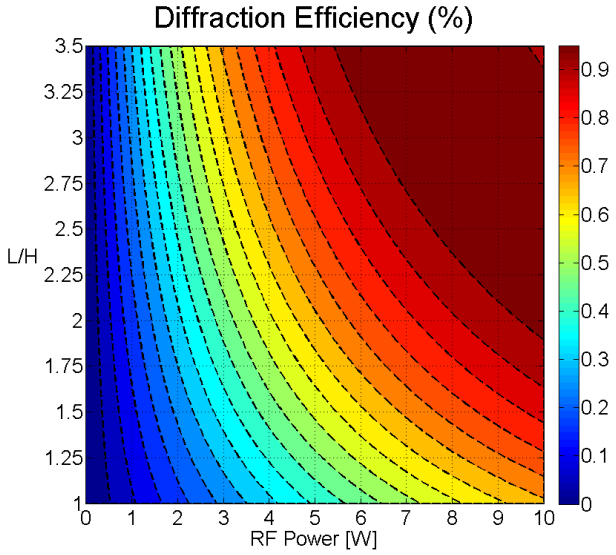

Figure 5.6: Diffraction efficiency for different ratio of the electrode dimension at 4.5 μm under the parallel tangent matching condition.

wavelength and θ_i, an example is shown in Fig.5.6.

In theory the RF power required to achieve peak diffraction efficiency could be drastically reduced for a ratio of L/H above 5. This becomes impractical for non-collinear AOTFs due the material dimension required to realize the device; in practice the ratio is of about 2.5 in case of non-collinear configuration. If the practical limit to the RF power (< 5 W), when TeO_2 is used, then maximum diffraction efficiency achievable is about 65% for a polarized source for $\lambda = 4.5\ \mu$m. The AOTF performance can be drastically improved with the help of an acoustic resonant cavity which increases the available acoustic power in the AO medium.

5.4 Acoustic resonant configuration

Conventional AOTFs have an acoustic absorber at the opposite face to the transducer, or for that face to be angled to deflect the sound out of the Bragg plane(Fig.5.7(a)). The acoustic power inside the AO medium is related to the RF power applied to the ultrasonic transducer and the diffraction efficiency is predicted by Eq.4.10 [6]. The diffraction efficiency versus acoustic power inside the medium can be increased by configuring the cell as an acoustic resonant cavity, where the acoustic wave propagates between parallel faces. Acousto-Optic mode locker relies on a similar configuration, but in this case the device is used due to the frequency shift introduced by the travelling acoustic wave back and forward.[6]

The acoustic wave will travel forward and backward where the strain inside the medium

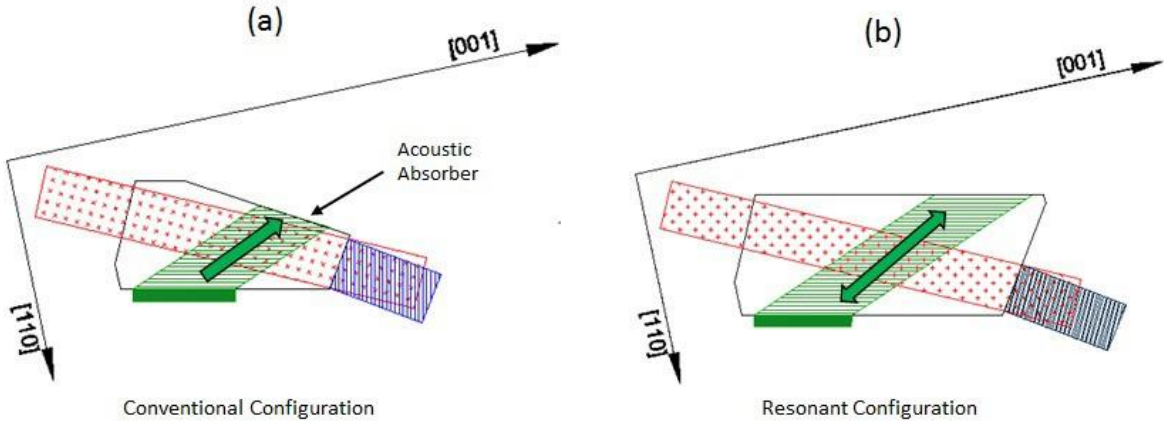

Figure 5.7: Conventional (a) and resonant (b) AOTF

increases, if the two waves are in phase. The relation between acoustic power and strain is defined as:

$$|S| = \sqrt{\frac{2P_a}{\rho V^3 H L_a}} \tag{5.1}$$

where V is the phase velocity, P_a is the acoustic power, ρ is the density of the material, H is the height of the acoustic beam (defined by the electrode), and L_a is the interaction length. In first approximation the acoustic power is considered equal to the RF power absorbed by the ultrasonic transducer, and from experimental results this approximation has been shown be in good agreement on the predicted performances. The acoustic power is given by:

$$P_a = \frac{\rho V^2 S^2 H L_a}{2} \tag{5.2}$$

which is substituted directly in Eq.4.9 for a conventional AOTF. In the case of a resonant AOTF the average power inside the AO medium is increased by the presence of the forward and backward waves depending on the number of reflection at both surfaces. In theory, if an ideal medium is considered where no acoustic losses are present and the medium is in perfect equilibrium, then the acoustic power inside the cavity could be theoretically predicted by a simplified model. The acoustic power stored inside the AO cell is determined by the applied acoustic power (P_i) applied to the transducer and estimating the number of "useful" reflection including the acoustic attenuation. The power stored inside a cavity length equal to L in case of an even number of reflection N is estimated by determining the effect of the acoustic attenuation for a given RF frequency and then folding the cavity and summing the acoustic power

of each acoustic reflection (Fig.5.10(a)):

$$P^{tot} = \sum_{i}^{N} P_i(x_j) \tag{5.3}$$

with $P_i(x_j)$ is defined by Eq.5.2, and the summation is carried over the same elements of different arrays.

The resonant AOTF devices has similarity with the AO mode locker, which rely on acoustic resonance. A simple physical analogue to described the effect of an acoustic resonant cavity where waves travel in opposite direction using an ideal losses medium, where the *"Hooke's Law corresponds to the force-displacement relation for a spring"* [17]

$$F = K x \tag{5.4}$$

where the strain corresponds to the displacement x and the applied force F correspond to the stress. In a conventional AOTF, acoustic waves create a periodic perturbation applied to a single particle therefore the strain is proportional to the applied stress. If a second acoustic wave with the same amplitude is travelling in the opposite direction to the first one, then the displacement is proportional to the instant force applied to the particle, hence the phase difference between the two waves will affect the total displacement (Fig.5.8).

The particle displacement reaches a maximum when $\phi = 0$ and the amplitude is double, which means the acoustic power at that specific point is four time the input power. The effect of the phase difference between the counter propagating waves is shown in Fig.5.9.

A lossless elastic material does not exist in nature, otherwise the acoustic wave will propagate unaltered forever, in reality a viscous damping term is introduced to described the acoustic attenuation; hence the acoustic power is dependant on the position and on the distance travelled inside the medium. The values of the acoustic attenuation has been introduced in section 3.4.1 for TeO_2, thus the intensity of the acoustic wave is reduced travelling back and forward in the crystal estimating the number of "passes" before the intensity of the acoustic wave go below a threshold level, where the diffraction efficiency is no longer improved. Here it is defined an advantage factor as

$$ADV = \frac{P^{tot}}{P_{in}} \tag{5.5}$$

where P^{tot} is the total power inside the resonant cavity, and P_{in} is the RF power applied to the ultrasonic transducer; the advantage factor (ADV) is dependent on the distance

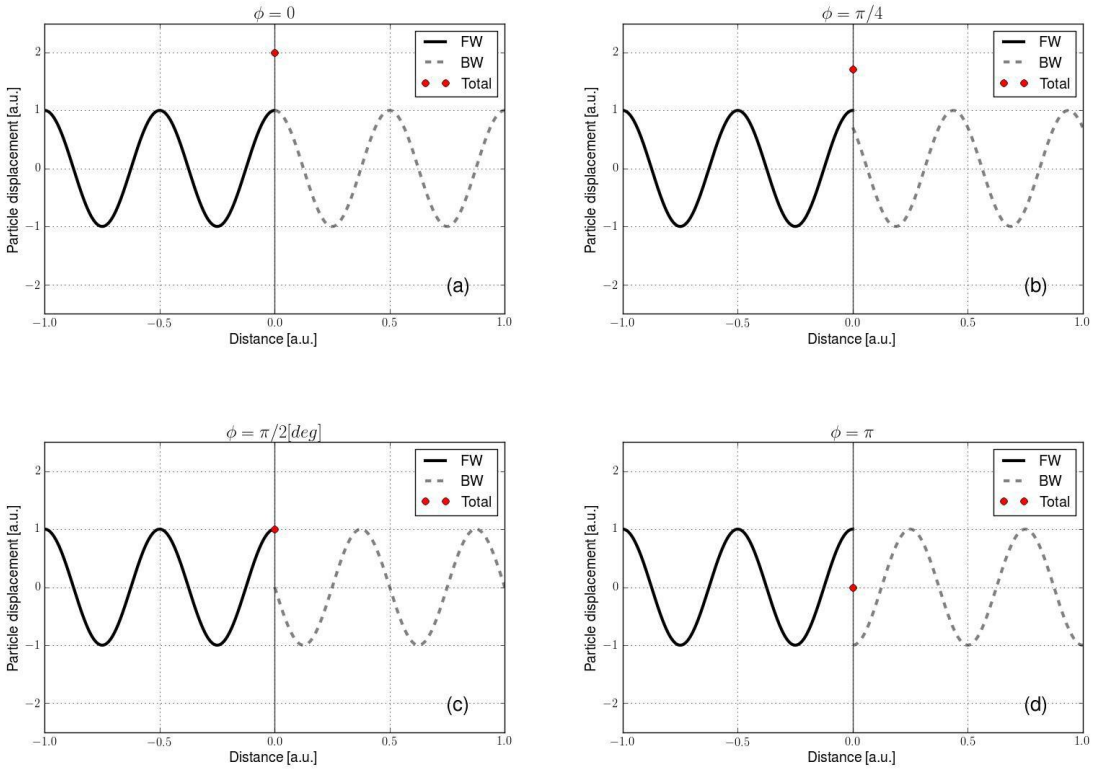

Figure 5.8: Particle displacement subjects to two counter propagating elastic waves with different phase difference: $\phi = 0$ (a), $\phi = \pi/4$ (b), $\phi = \pi/2$ (c), $\phi = \pi$ (d).

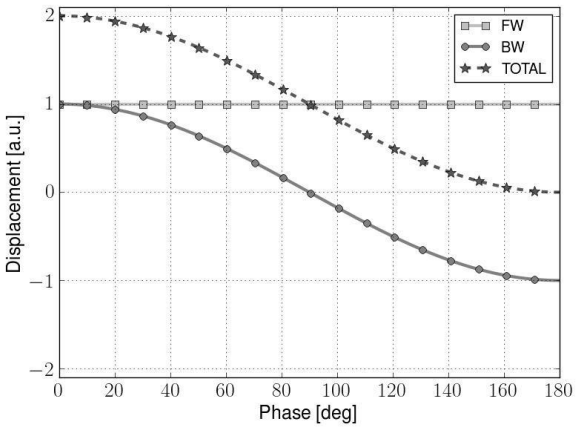

Figure 5.9: Effect of the phase difference between two counter propagating waves on the particle displacement

from the transducer, an example is reporte in Fig.5.10 for a cavity length of 20 mm. From the advantage factor it is possible define a acousto optic figure of merit for

resonant devices following Keller et al.[30]:

$$M' = \frac{M}{\alpha(f)d} \tag{5.6}$$

where d is the distance between the parallel faces in millimetres, $\alpha(f)$ is defined as:

$$\alpha(f) = af^3 + bf^2 + cf + d \tag{5.7}$$

with f defined in megahertz, and with a = -9.3947 × 10^{-5}, b = 0.0130, c = -0.6548, and d = 13.7673.

The acoustic wave is also subject to diffractive effects, which are not considered in this model, therefore the advantage factor is limited by the acoustic attenuation. The acoustic attenuation increases proportionally to f^2, thus in order to obtain an elevated advantage factor the RF frequency has to be lower than 50 MHz, which is typically obtained for $\lambda > 1\mu m$.

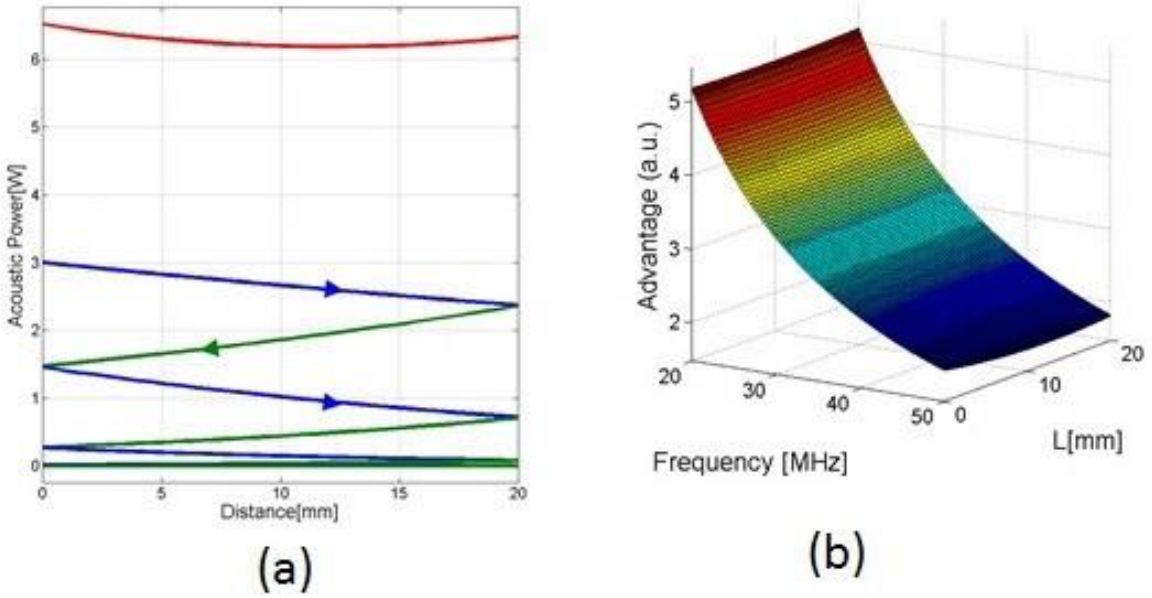

Figure 5.10: Acoustic power inside a resonant cavity (red line) and forward (blue line) and backward (Green Line) travelling acoustic wave for a cavity length of 20 mm (a). Advantage factor for different different frequency and cavity length of 20 mm. (b)

The acoustic waves travelling in both direction are in phase when the correct RF frequencies are selected, defined as *"resonance frequencies"* and determined by the distance between the parallel faces (l) of the AO medium and the phase velocity (V) of

the acoustic wave using the following relation:

$$F_{res} = \frac{V}{2l} \tag{5.8}$$

thus the RF frequency applied to the ultrasonic transducer has to be a finite multiple of F_{res}, if this condition is satisfied then the backward and forward acoustic waves are in phase and resonance between the different elastic waves is established, consequently the advantage factor reaches a maximum. The effect of the acoustic wave travelling back inside the ultrasonic transducer affects the performance of the device and is introduced in the next section in more detail.

5.4.1 Effects of travelling wave in acoustic resonant cavities

The reflected acoustic wave travelling inside the ultrasonic transducer does not affect the RF matching performance because no additional stress is created inside the ultrasonic transducer since the forward and backward acoustic waves are in phase. In reality thermal gradients are present inside the AO medium due to the acoustic attenuation. The acoustic attenuation is a source of heat inside the AO medium, this changes the cavity dimension altering the phase of the backward acoustic wave and subsequent reflection. Two noticeable effects are visible when out-of-resonance: first a feedback signal is generated by the ultrasonic transducer due to additional stress components, which generate an electrical signal transmitted inside the matching networking affecting the VSWR which can reach a level above 10. Hence most of the RF signal applied to the ultrasonic transducer is reflected back into the RF driver. The resonance is dependent on the acoustic cavity dimension, which is strongly affected by any change in temperature of the crystal mainly due to the acoustic attenuation effect. The second effect is the reduction of the diffraction efficiency because acoustic wave are no longer generated by the ultrasonic transducer and the temperature inside the AO medium drops generating temperature gradients. Consequently, the free spectral range (the distance between resonance frequencies) changes due to the modification in time of the cavity length.

In conclusion in order to maintain resonance, the AO medium should be in thermal equilibrium with the aid of a lock-in mechanism to track the resonance frequency. It has been seen experimentally that a lock-in mechanism is required when the RF power is above 500 mW for TeO_2, and several Watts in case of crystal Quartz.

Acoustic resonance has been observed in the transducer by monitoring the VSWR experimentally by means of pulse echo measurements, described in Appendix F. The results obtained have been compared to the measurements taken by a network analyser.

The resonance frequencies of the devices were determined by the presence of negative peaks in the VSWR, where the "actual" VSWR was measured (Fig.5.11).

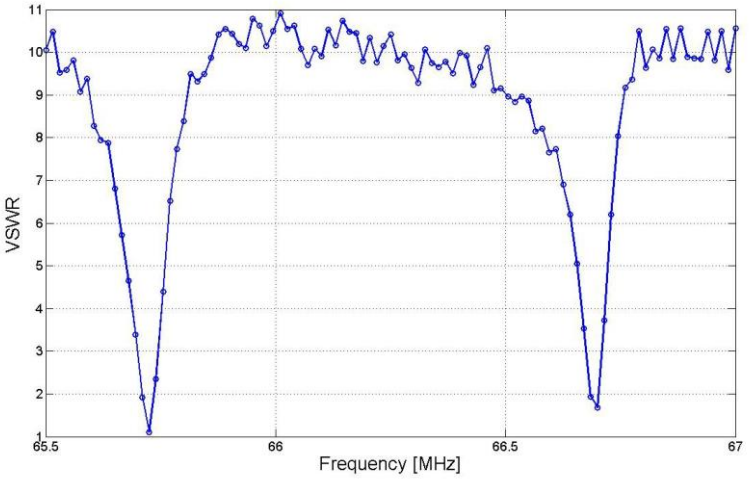

Figure 5.11: VSWR recorded by Network analyser of the resonant AOTF, with tuning range between 1µm and 2µm.

When the cavity is off resonance the electrical coupling is poor, and most of the RF power delivered by the RF driver is reflected back from the transducer (VSWR>25). The "free spectral range" of the cavity is determined by $\Delta f = V/2L$ and this was in good agreement with the observed frequency spacing on the network analyser.
The position of the resonance frequencies depends on the cavity dimension and is affected by temperature modification, due to the attenuation of acoustic waves and heat generated by the transducer. Therefore the resonance frequency spacing and position are not stable and without a temperature compensation mechanism are difficult to track. For this reason a lock-in process is described in order to maintain the device on resonance. This would continuously monitor the VSWR of the transducer and the temperature of the cell and so maintain resonance.
As it has been previously stated, the out-of-resonance the electrical coupling is poor, therefore the tuning relation (Eq.4.5) is not continuous, as on conventional a device, but is formed by a series of allowed frequencies. For this reason the dimension of the resonant cavity should be configured so as there are sufficient resonance frequencies for a given passband. In practice, this is easily achievable for a large aperture AOTF.

5.5 Resonant AOTF devices in Tellurium Dioxide

Two resonant AOTFs were designed and built to demonstrate the principle and accuracy of the mathematical model. The first prototype had a tuning range between 1μm

and 2μm but no temperature compensation mechanism was included (Fig.5.12). The second prototypes was optimised design for the wavelength range between 2 μm and 4.5 μm.

5.5.1 Prototype Resonant AOTF between 1μm and 2μm.

The first prototype of the resonant AOTF was built using an existing cell from an imaging AOTF working in the visible range, but bonding an ultrasonic transducer with a different thickness in order to allow operation in the IR range between 1μm and 2μm. A broad band matching network was designed and built in the desired frequency range. The acoustic phase velocity direction was about -82° and $\theta_i = 15.5°$. The electrode size is equal to 5 mm(H) x 10 mm(L), which is smaller compared to a standard device to take account the acoustic divergence in the out of the plane direction typically shown in the K-space diagram. The performance predicted by the mathematical model showed RF power for diffraction efficiency lower than 400 mW, therefore no temperature compensation mechanism was added since for RF powers below 1 W it is possible to achieve temperature stabilization easily.

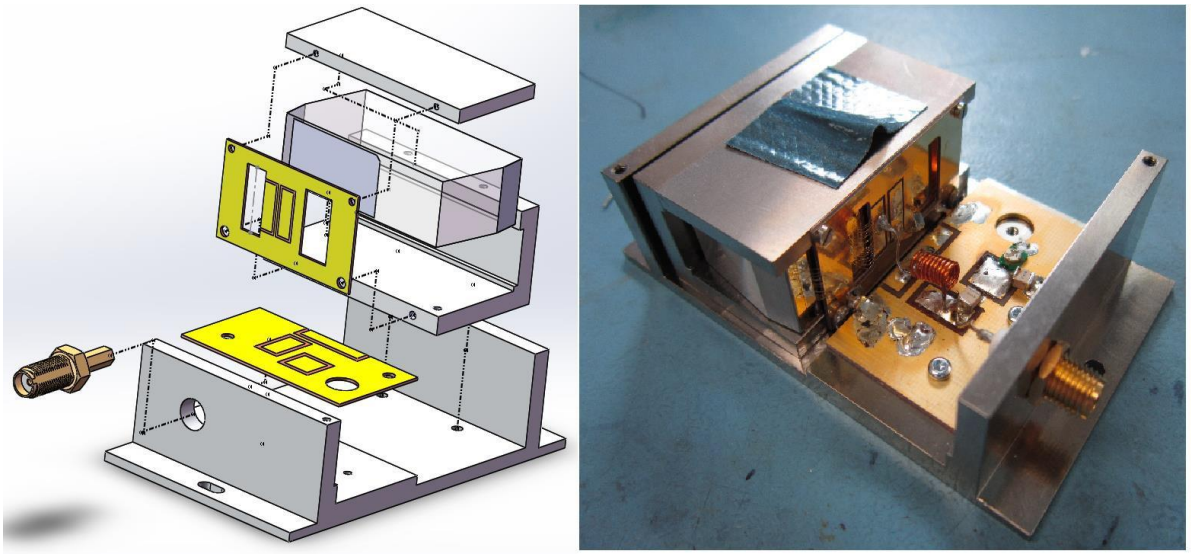

Figure 5.12: SolidWorks assembly (left) and final device (right).

The matching network was been split in to two different PCBs in order to obtain the broad band matching, this solution is typically used on a large aperture AOTF with extended frequency range. The presence of feedback signal from the transducer when the resonance frequencies are not selected makes it difficult to predict the matching network.

In this case the vertical PCB has been added because the conventional way to design

matching networks is of applied here due to the presence of the reflected acoustic wave, which has been verified by recording the VSWR of the device on a spectrum analyser. The free spectral range of the acoustic wave was 15,75 MHz, which confirmed the acoustic phase velocity excited by the ultrasonic transducer for the thickness of the cell equal to 21.26 mm, giving an acoustic velocity equal to 669,69 m/s with an error equal of 0.04% (where the theoretical value of the phase velocity is 670 m/s).

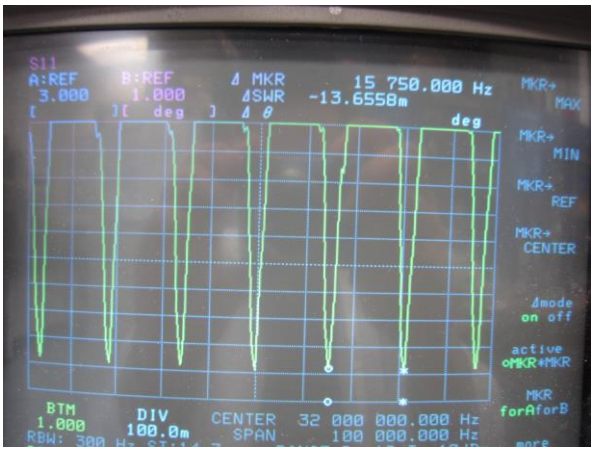

Figure 5.13: Photograph of the data recorded from the resonant AOTF with a spectrum analyser.

The RF power for peak diffraction efficiency has been measured with laser line test described in appendix G.1. A peak diffraction efficiency equal to 85% was observed, which is limited compared to a conventional AOTFs where the diffraction efficiency is typically above 95% for linearly polarized light. The RF power vs. diffraction efficiency was recorded with a laser at $\lambda = 1550$ nm.
The measured performances were close to the predicted values therefore an optimized design has been prepared operating in the wavelength range between between 2μm and 4.5μm.

5.5.2 AOTF optimized design for wavelength range between 2μm and 4.5μm

A second AOTF with an optimized design was built with a tuning range between 2μm and 4.5μm (Fig.5.14) satisfying the parallel tangent matching condition. The acoustic propagation (θ_a = -78.0°) was to increase the RF frequency to simplify broadband matching, leading to a particularly large AO cell due to the acoustic walk-off. The predicted performance was obtained from dedicated Matlab routine to design resonant device, written by the author. The temperature equilibrium of the AO cell ws moni-

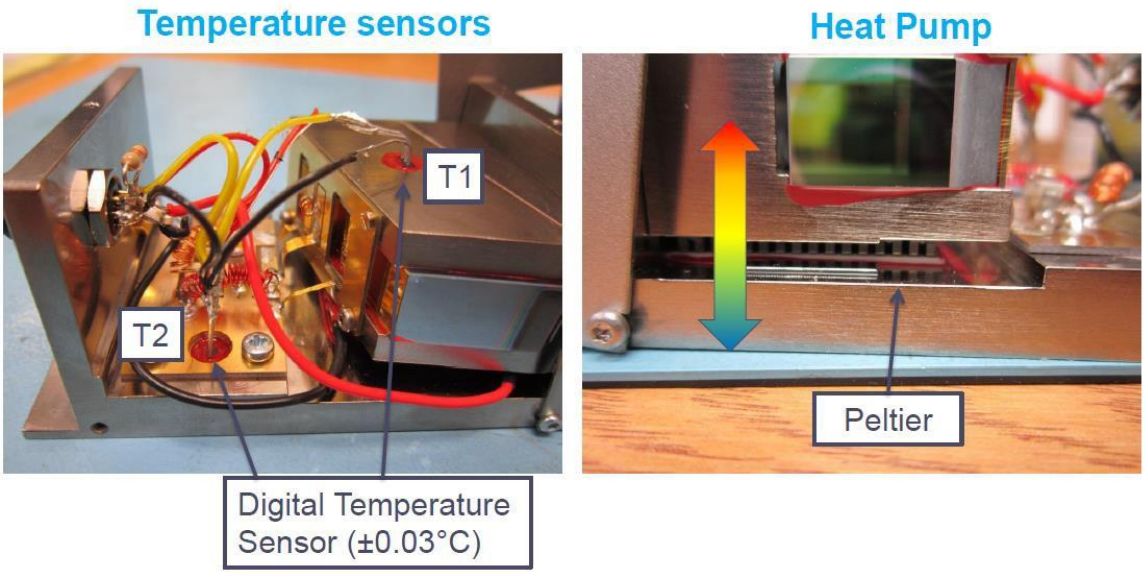

Figure 5.14: Optimised resonant AOTF photo of the inside where the position of the temperature sensor is shown(left). Detail of the heat-pump position used to stabilise the temperature (right).

tored by two digital temperature sensors (DS18B20) mounted on the top and on the bottom of the AO cell and controlled by an external microprocessor. Temperature is measured with a precision of 0.03°C. In addition, a Peltier thermoelectric heat pump was installed to control the temperature and minimise gradients inside the AO crystal. The heat pump and the temperature sensor were controlled using a dedicated connector with 6 pin and using the following schematic. The data cable and temperature con-

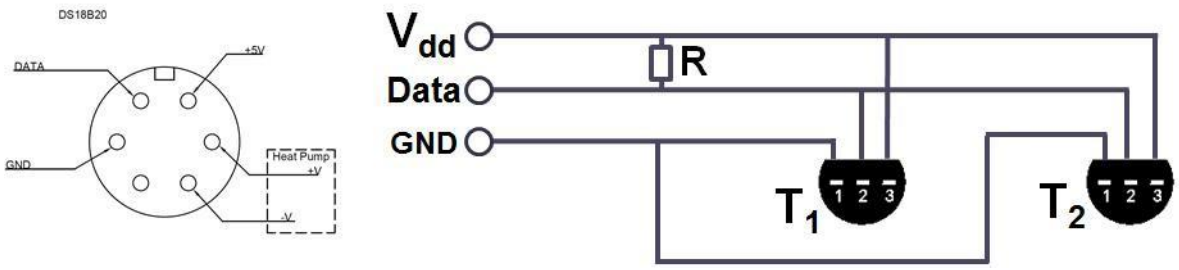

Figure 5.15: Schematic of the temperature sensors connection to the plug.

troller where connected to a power supply for the heat pump and to a micro-controller (Arduino) to read the temperature from both temperature sensors, which can be addressed separately on the same data line. The heat pump connection where connected to a power supply controlled manually, and the *+5 V*, *GND*, and *DATA* connections were wired to the Arduino, which allow to record the temperature of the crystal.

5.6 Active Lock-in via temperature control

The resonant frequency of the AOTF may be controlled by temperature, however the aim was to achieve thermal equilibrium within the surrounding ambient. This was complicated is due by the heat generated by the attenuation of the acoustic wave, which can be considered as a heat source. It has been proposed to cool down the devices to cryogenic temperature by Chang . The heat pump could be used to extract the heat generated by the acoustic wave, however this solution create a unstable lock-in condition, because the RF power increases with the wavelength and the acoustic attenuation decreases altering the thermal equilibrium. The solution proposed here is

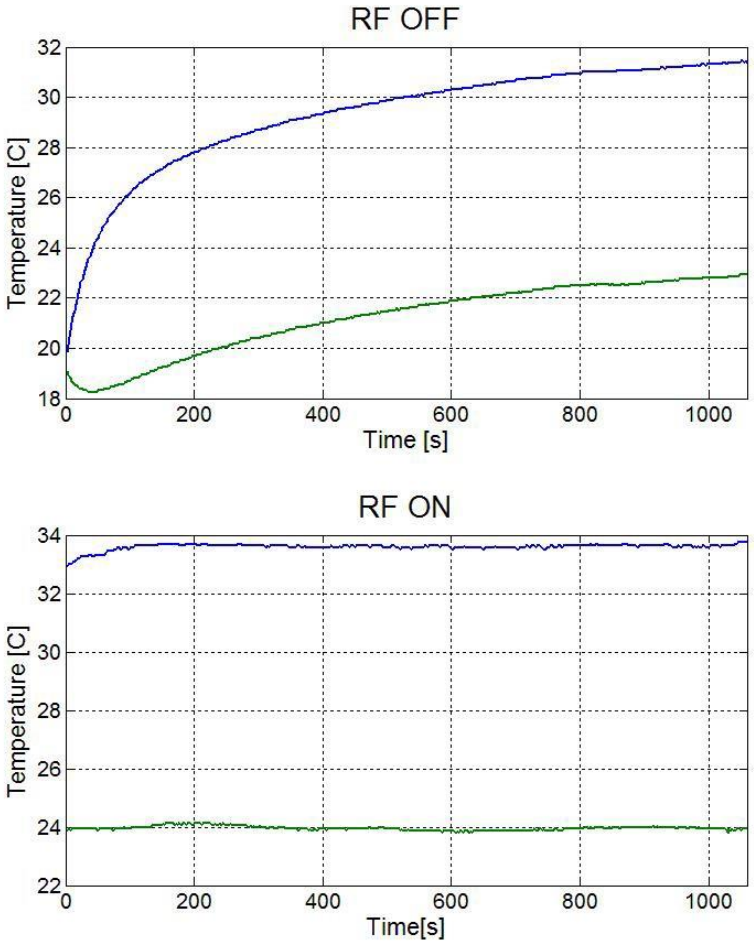

Figure 5.16: Temperature recorded from the temperature sensor with RF off and RF on.

to use the opposite approach; the cell is heated up to a temperature of about 30°C by means of the heat pump and at the same time the base of the AOTF is cooled down helping to maintain a stable matching temperature. When the RF power is

applied then the temperature inside the AO cell increases up to 1°C - 2°C, altering slightly the thermal condition. The resonance frequency of the devices change with

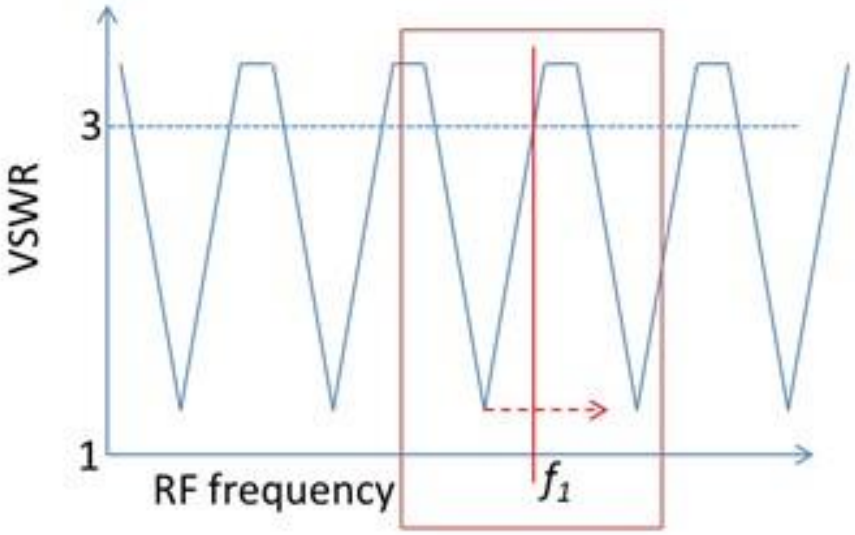

Figure 5.17: Direction of the shift of the resonant frequencies with temperature.

the cavity size, therefore a change in the temperature moves the resonance frequencies, which are the negative peaks in the VSWR. The lock-in is obtained selecting a RF frequency where the VSWR has a negative slope, with the increase of temperature the peak moves toward a minimum and then increases again. When the minimum on the VSWR is reached the coupling coefficient reaches a maximum changing the RF frequency by a small amount Δf in order to select a position, where the slope of the VSWR is negative.

The controller of the driver tracks the selected peaks, and the trigger changes the

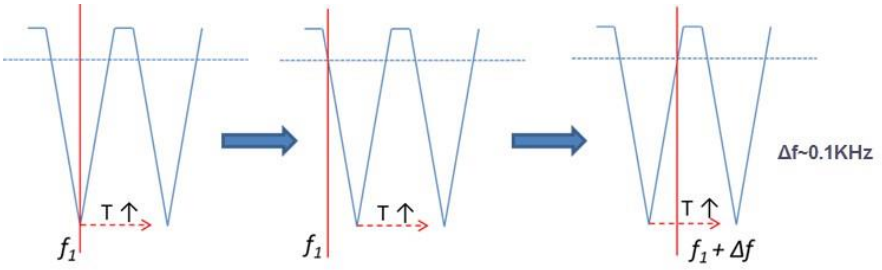

Figure 5.18: Lock-in process used to maintain the resonant device in resonance.

frequency to the correct value where the VSWR > 2, therefore the temperature of the AO cell increase continuously, after about 10 minutes, the temperature stabilization is reached and the device remain locked for about 3 hours. This solution allow to control the resonance AOTF by means of simple software.

Component	Identification	Supplier	Cost	Quantity
μ-controller		Texas Instrument	£8 - £25	1
Power Supply	117-769(350W)	RS Components	£55	1
Power Detector	ZX47-40LN+	Minicircuits	£ 75.47	1
20dB Coupler	ZDC-20-1BR+	Minicircuits	£ 44.85	1

Table 5.1: Basic components to realize the resonant RF driver.

5.6.1 Advanced RF Driver controller

The resonant AOTF driver could be also realized by using COTS[1] components.

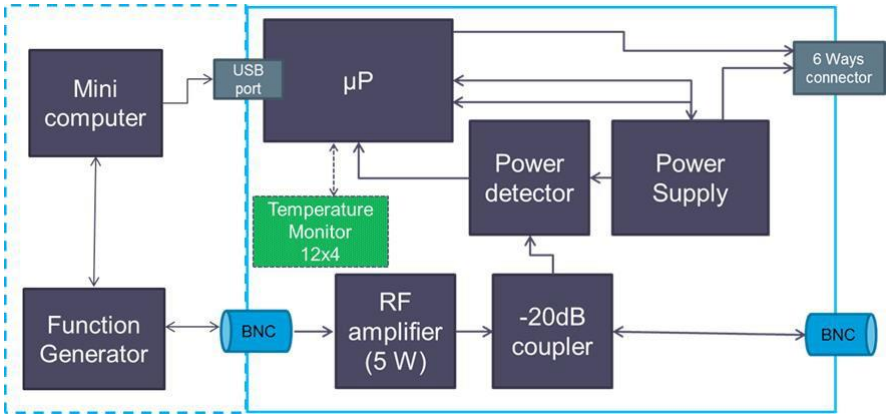

Figure 5.19: Schematic proposed to build a RF driver to be used with resonant acousto-optic device.

The solution could be embedded inside a dedicated RF driver, or realized as an external module between the RF driver and the AOTF. The list of components (Tab.5.1 and Tab. 5.2). The solution proposed is modular in order to meet potential early users needs, and list in Tab.5.1-5.2 are intended to advise COTS components, which might be used and to give a rough idea of the price range to build the preliminary system. The prototype was not been built because it was out of the scope of the research activities, and it has been presented to help additional effort on the developing of a RF driver for resonant acousto-optic devices.

Another solution is to implement a phase locked loop as described in [31], where the resonance frequency is continuously tracked, this solution could be implemented in addition to increase the capability of the current drivers produced by Gooch & Housego.

[1] Commercial Off-The-Shelf

Component	Identification	Supplier	Cost	Quantity
RF amplifier 5W	ZHL-5W-2G	Minicircuits	~ £900	1
Function generator	DSS module	AD9854	~ £100	1
Mini-Computer	Beagle board	RS components	£25- £ 50	1

Table 5.2: Additional Components

5.7 Test Setup

The resonant AOTFs were tested using the set-up shown in Fig.5.20 and Fig.5.21.

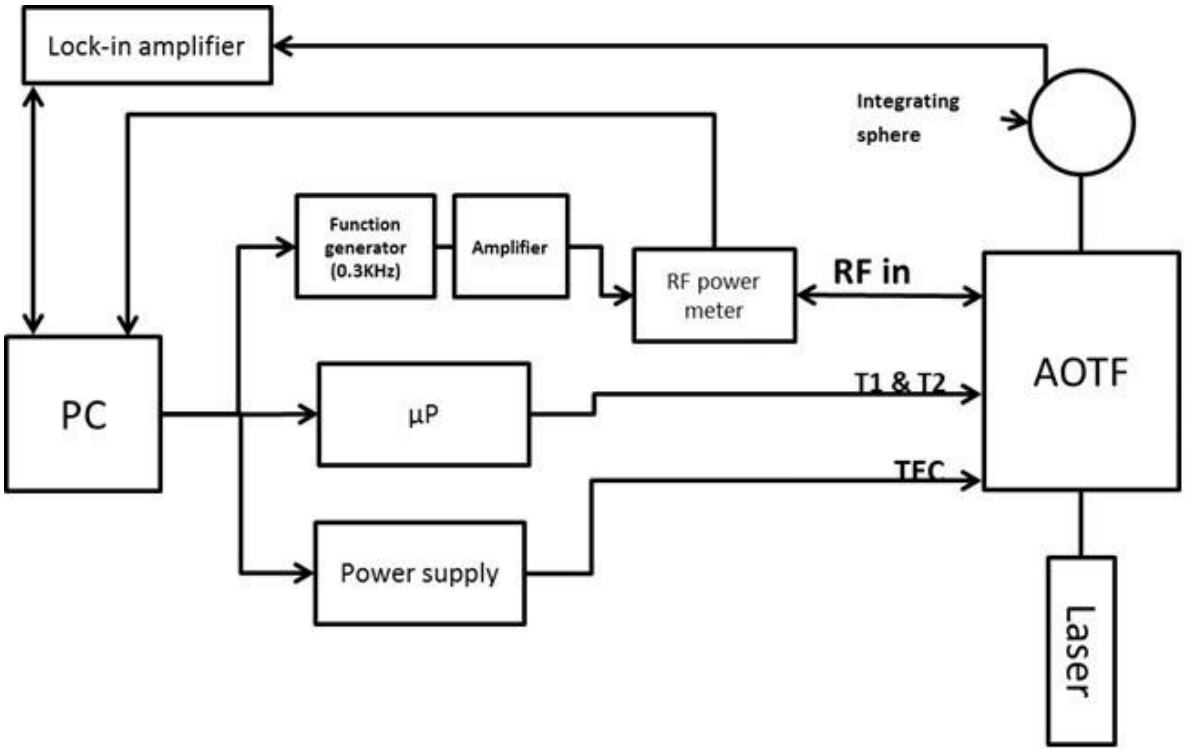

Figure 5.20: Setup with lock-in amplifier and laser source

The laser line test (Fig.5.20) was used to record the RF power versus diffraction efficiency for a fixed wavelength predicted by Eq.(8.11); a lock-in amplifier was used in order to achieve greater accuracy. Two different laser lines were chosen: 1550nm, and 3390nm. The RF power meter was used to measure the VSWR of the device and the RF power delivered by the function generator, which had a precision of 1 Hz. The tuning curve, predicted by Eq.4.5, of the first prototype was determined using the setup in Fig.5.21, where a supercontinuum source with a spectral emission in the range of 450

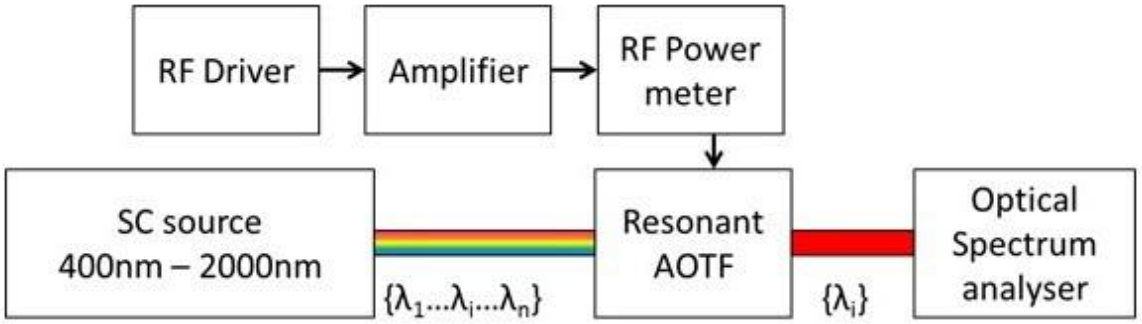

Figure 5.21: Setup and with supercontinuum source

nm up to 2000 nm was used. The first diffracted order had been measured by means of an optical spectrum analyser and the RF power for PDE had been measured for the wavelength range between $1\mu m$ and $2\mu m$.

5.8 Performance comparison between conventional and resonant configuration

In order to verify the feasibility of the proposed solution, the two different devices as described above. The first prototype has a tuning range between $1\mu m$ and $2\mu m$, as expected the advantage obtained by the resonant configuration was about 4, using the Matlab routine to design resonant AOTF, and the tuning relation was in good agreement with the predicted values with an error within ±0.05% (Fig.5.22). The optimize design with a tunable range between 2 μm and 4 μm was tested using the setup in Fig.5.20, using a laser source at 3390nm.
The advantage factor measured was about 5 and in good agreement with the theoretical values.

5.9 Frequency shift in the resonant AOTF

The AO interaction introduce a frequency shift on the first diffracted order equal to the RF frequency applied. The direction of the shift depends on the phase matching condition, as previously reported a phonon could be generated or annihilated in the AO interaction, this effect could be represented in the K-space diagram by the by the direction of the K_a vector [6]. It has been reported by Ward and Pannell [32], where

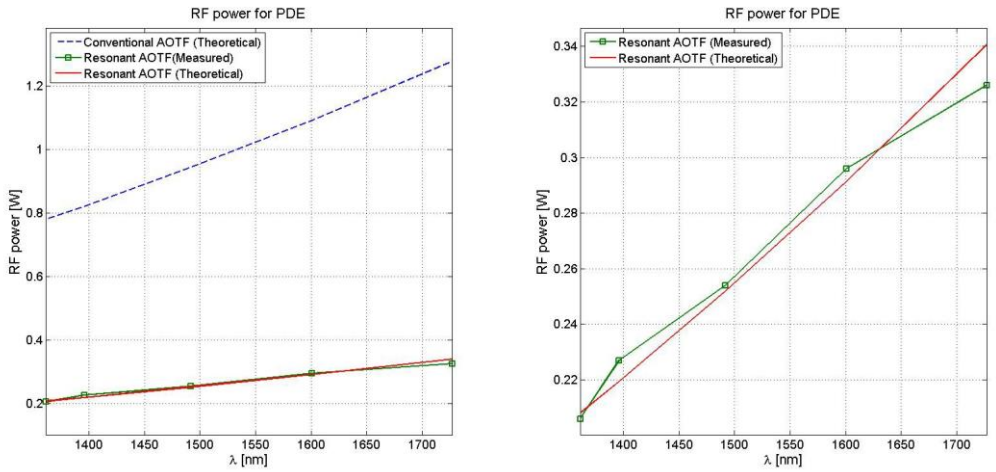

Figure 5.22: RF power for peak diffraction efficiency(right), detailed view of the resonant AOTF performance(left)

a pair of AOTFs was matched to generate a null frequency shift, where the acoustic vector propagates in opposite direction. In case of a resonant AO devices particular was not clear if the travelling acoustic wave travelling forward and backward in the device would generate an up-shift, down-shit, or a null-shift. Therefore an experiment was carried to experimentally measure the frequency shift of the device by means of an interferometer. The set-up is shown in Fig.5.24, where two AOTFS were used.
The first AOTF was used to introduce an initial frequency shift, which was measured in order to have the reference. The first AOTF was operated at 64.5670 MHz with an RF level of 1 Watt. The resonant AOTF was driven at 32.6632 MHz. The combined signal from the reference and shifted arms was measured with a photo diode connected to a spectrum analyser with an accuracy of 1 Hz.
The experimental results shows the presence of a down-shift and up-shift components, due to the forward and backward acoustic wave respectively. The reason of the presence of both shifts is believed to be the resonant acoustic wave is seen by the phase matching condition as two separate waves, which are in phase, therefore an advantage factors is measured and the difference between the down-shift and up-shift is of the order 10×10^{-5} nm, detailed information are going to be reported in the paper in preparation.

5.10 Conclusions

In conclusion the practical limitation on the RF power ($< 5W$) for conventional AOTFs limits their use for several applications in the wavelength range above $2\mu m$. The RF

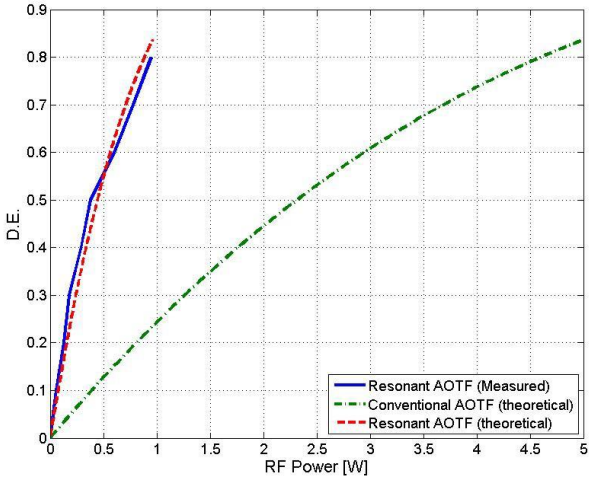

Figure 5.23: RF power versus diffraction efficiency for $\lambda = 3390$ nm.

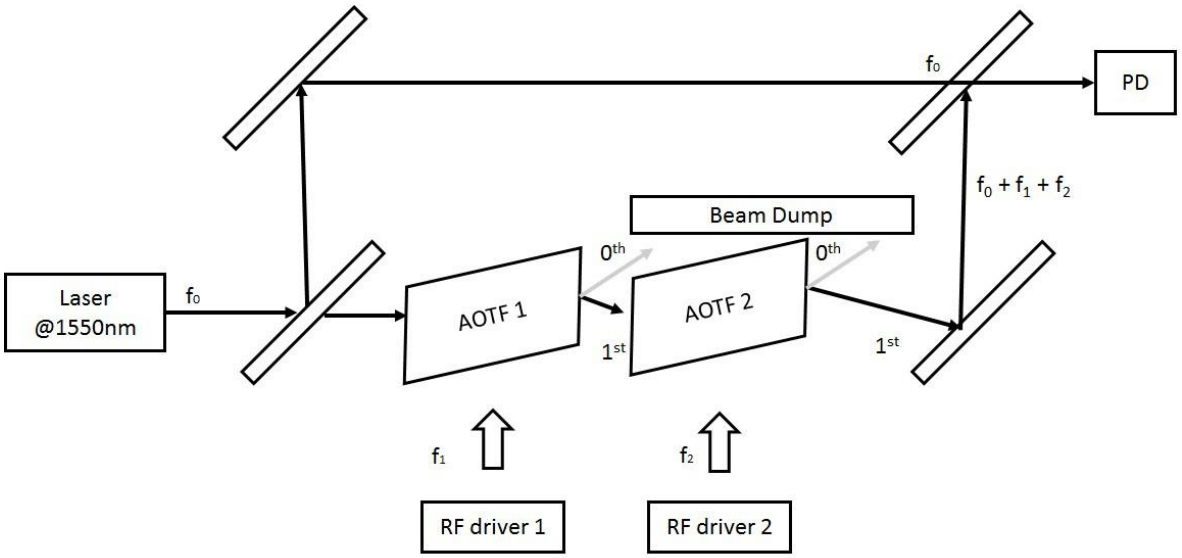

Figure 5.24: Frequency shift AOTF set-up where the resonant AOTF is second AOTF, and AOTF 1 is introduced to generate an initial frequency shift.

power for peak diffraction efficiency whilst being material dependent and limited by the interaction length tends to be determined by the λ^2 dependency. One solution to reduce the RF power could be to increase the interaction length, but because the acoustic walk-off quickly increases the material footprint and anyway, this will serve to narrow the line width and thus restrict optical throughput.

The resonant configuration is an effective solution to reduce the power consumption of AO devices since the phonon energy is effectively "recycled", thus reducing the RF power requirement. However, acoustic attenuation restricts the use of such a solution in the visible range, as the RF frequency is usually too high (>50 MHz). The tuning

curve is not continuous in the case of resonance devices, but due to the large aperture it is possible to achieve more than 20 point per nanometers.

The experimental results are in good agreement with predictions. The tunability of the first prototype was demonstrated in the wavelength from 1μm and 2μm. Unfortunately no suitable white-light source was available to test the tunability in the 2μm to 4μm range of the optimized design, but the laser test showed good agreement with the predictions. Consequently we are confident of the tunability of the device.

The electrical feedback signals, when the device was out-of-resonance, created an issue for the electrical matching which could be harmful to the RF components, for this reason a lock-in mechanism to maintain the device on resonance is highly desirable. The implementation of the resonant controller could be realized using alternative approaches, currently a non-integrated solution is under development, which hopefully will lead to an integrated solution.

Chapter 6

Acousto-Optic Tunable Filter for wavelength above 5μm in Calomel single crystal

6.1 Introduction

The wavelength range above 5μm is of particular interest for several applications from remote sensing to biological studies [33].

Gooch and Housego Ltd.(UK) is leading a European project (FP-7) with the aim to build a system able to diagnose premature skin cancer cells analysing the spectrum between 4.5μm and 10μm. The current system in development is a microscope fitted with a super-continuum source illuminating the target, with a tunable filter to select a narrow bandwidth of the spectrum. Thus an acousto-optic tunable filter with wavelength range up to 10μm seems to be a good option and will be developed by G&H.

The wavelength range in consideration is beyond the transmission window of Tellurium Dioxide, which is limited to about 5 μm, thus the research activity has been focused on other birefringent AO materials with extended transmission in the Long Wavelength Infrared (LWIR). Mercurous halides have been reported to be crystals with good acousto-optic properties [34][35]; for example Mercurous Bromide (Hg_2Br_2) has been extensively studied by Gupta and Voloshinov and several papers have been published [36][37], another crystal is mercurous chloride, also known as Calomel. A Calomel single single crystal was selected due to its availability. This particular crystal is supplied by BBT, a crystal growth company based in to Czech Republic, which is part of the

c_{11}	0.8925×10^{10}	[N/m]
c_{12}	1.7192×10^{10}	[N/m]
c_{13}	1.563×10^{10}	[N/m]
c_{33}	8.037×10^{10}	[N/m]
c_{44}	0.8456×10^{10}	[N/m]
c_{66}	1.225×10^{10}	[N/m]

Table 6.1: Elastic stiffness constant for Calomel Single Crystal

consortium. The agreement within the project is to design the AO cells and polished cells supplied by BBT.

6.2 Calomel Single Crystal properties

The acousto-optic properties of Calomel single crystal have been investigated by [2][38], where a high M_2 for the longitudinal mode has been reported. In the literature the value of the acousto-optic figure of merit for slow shear interaction is only reported for propagation direction along the *t axis*, thus the physical properties of Hg_2Cl_2 are investigated for the feasibility of an AOTF design. This crystal is an anisotropic material with an extraordinary slow shear velocity and high density ($\rho = 7180\ K\ g/m^3$) [7], belonging to the tetragonal crystal class and the elastic constant values are reported in table 6.1

The crystal symmetry allows to use the same analytical results obtained for TeO_2 using the appropriate elastic stiffness constants. Only the detailed study of the relevant acoustic mode used in the birefringent AO interaction is examined, the reader is invited to follow the same analysis described in Ch.2 for Tellurium Dioxide in case of the other acoustic modes.

The acousto-optic interaction takes place in the tZ plane, because the slowest velocity lies in this plane, and the acousto-optic figure of merit is at a maximum. Another reason to select the plane is the acoustic wave polarization, which is always perpendicular to the plane due to the crystal symmetry; the phase velocity expression for the slow shear mode for an arbitrary direction of propagation in the plane can be expressed by Eq.(3.30):

$$V_S^2 = \frac{c_{66}^{'}}{\rho}\cos^2(\theta) + \frac{c_{44}}{\rho}\sin^2(\theta) = V_t\cos^2(\theta) + V_z\sin^2(\theta) \qquad (6.1)$$

with θ measured from [110] direction, V_t = 347 m/s, and V_z = 1084 m/s; the slowness curve of Calomel single crystal is shown in Fig.3.13. Before entering in to details of the AOTF design, it is necessary to introduce the physical and chemical properties of

Calomel Single crystal, which effects the design consideration.

6.2.1 The physical and chemical properties of Calomel single crystal

Mercurous Halide crystal are known to have adverse physical and chemical properties, which limits the possibility to use conventional bonding technique using elevated pressure and non-noble metals as bonding layers. Calomel single crystal (Hg_2Cl_2) chemically reacts with non-noble metals releasing free mercury and creating defects on the surface which propagate inside the crystal, therefore the conventional technique used in Gooch and Housego Ltd. (UK) cannot be implemented because it requires the use of non-noble metals at high pressures. Attempts to bond an ultrasonic transducer directly was reported by Gottlieb [36] and Gupta [34], where the calomel crystal is protected by a thick layer of gold. This solution was impractical from the point of view of day to day production due to the inherent risk of contaminating the bonding plant.
A solution was proposed to overcome the bonding issue related to the conventional technique consisting of the use of a intermediate substrate made of a material with similar acoustic impedance, where a conventional bonding technique could be used; where the continuity of polarization vectors is preserved across the two different materials, in order to excite the correct acoustic mode inside the Calomel crystal.
This technique is described in detail in the next section, before describing the design of the Calomel AOTFs developed for the MINERVA system, the non-standard bonding technique is introduced from the theoretical point of view and experimental results discussed. The results obtained are relevant for the feasibility study of the AOTF.

6.3 Non-Standard bonding technique

The non-standard bonding technique developed uses, an intermediate substrate made of a suitable crystal bonded to Calomel by means of an adhesive layer. Particular attention has been paid to identify a proper material, which should have similar acoustic impedance and most important, that the eigenvectors continuity is maintained in order to excite the correct acoustic mode inside the AO material. The continuity condition is defined by

$$v(\theta_{a1}) \times v_{Hg_2Cl_2}(\theta_{a2}) = 0 \tag{6.2}$$

where v and $v_{Hg_2Cl_2}$ are the eigenvectors related to slow shear mode in this case for the substrate material and for the Calomel cell, respectively. Different materials were

investigated in order to determined the best candidate to use as a substrate.

6.4 Substrate choice: Tellurium Dioxide TeO_2

The material choice of the substrate was influenced by the availability and possibility to be manufactured inside the G&H site, leading to three different possibilities: fused silica, crystal quartz, and Tellurium Dioxide. The theoretical performance of each substrate was investigated in order to determine the best candidate for the preliminary test. Crystal quartz and fused silica were considered but poor acoustic matching impedance was predicted by a dedicated modelling routine prepared in Matlab written by the author.

The preliminary results are not reported below for brevity and only the results of the most promising material are reported in this thesis. The material substrate giving the best performance was found to be Tellurium Dioxide, due to its crystal class being similar to the Calomel single crystal. It posses a similar acoustic impedance for the slow shear mode relevant to the acousto-optic interaction. Because of the anisotropic nature of the phase velocity in both crystals, a mathematical model was developed in Matlab by the author to determine the best orientation for both crystals to maximize the acoustic transmission between the bonded substrate and the AO cell.

6.5 Acoustic impedance matching

The theoretical acoustic coupling coefficient between two different materials is estimated by the acoustic impedance defined by $Z = \rho V$, where V is the acoustic velocity defined by the mode and propagation direction in case of acoustically anisotropic material. The transmission and reflection coefficients are defined from the acoustic impedance by [6]:

$$R = \frac{Z_2(\theta) - Z_1(\theta)}{Z_2(\theta) + Z_1(\theta)} \tag{6.3}$$

$$T = \frac{2Z_1(\theta)}{Z_2(\theta) + Z_1(\theta)} \tag{6.4}$$

where $Z_1 = \rho V_1(\theta)$ is the acoustic impedance of the acoustic wave in the first medium, which is TeO_2, and $Z_2 = \rho V_2(\theta)$ is the acoustic impedance in the second medium, which is the AO cell made of Calomel.

The theoretical reflection coefficient is estimated for any propagation direction of the

acoustic wave in the latter with θ_{a2} in the range between 0 ° and 180 ° rotating the former. Results of the theoretical transmission are shown in Fig.6.1(a), using the schematic of Fig.6.1(b) as a reference, where a perfect bond at the interface 1 is assumed.

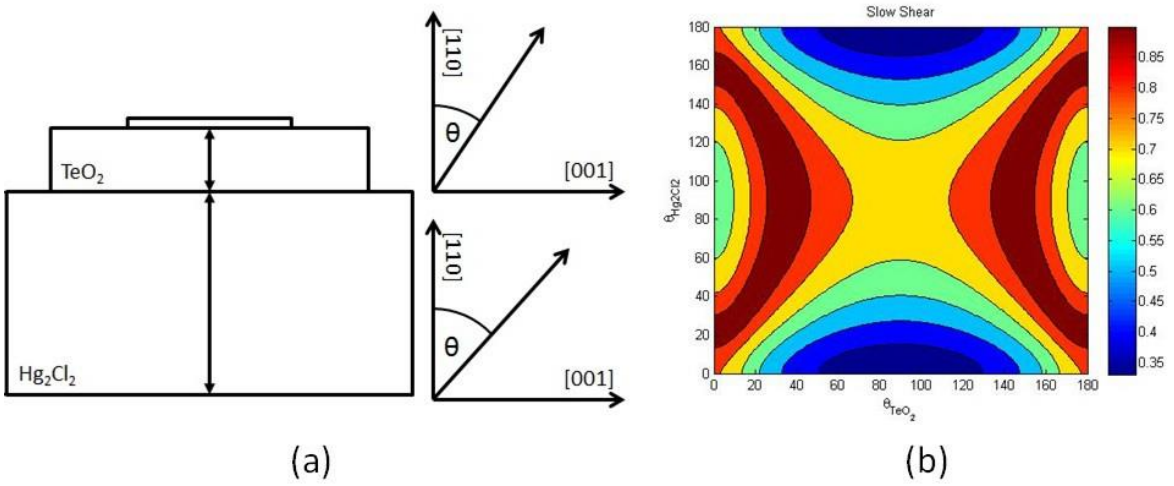

Figure 6.1: Configuration of TeO_2 bonded to Hg_2Cl_2 (a) and relative transmission coefficient (b)

The theoretical model developed in Matlab allows the best orientation of the substrate for a given direction of the acoustic wave to be selected. It is possible to maximize the transmission of the acoustic wave from a medium to another. The theoretical transmission of the acoustic wave between Hg_2Cl_2 and TeO_2 crystals is 95%, in practice this value is never reached this due to presence of an organic bonding layer affecting the coupling coefficient.

6.6 Bonding material

The choice of the bonding material depends on the Calomel single crystal properties and should have the following specifications:

- **No UV cure required**: Hg_2Cl_2 single crystal must be protected from UV radiation, otherwise the crystal becomes dark and prevents transmission (*solarize*), consequently the bonding material must cure without UV expositions.
- **Good homogeneity**: the acoustic waves travelling through the bonding layer should not be subject to scatter, in order to maintain the direction of polarization vectors; thus the particle size inside bonding layer should be an order of magnitude smaller than the acoustic wavelength.

- The **hardness** of bonding layer is proportional on first approximation to the acoustic waves attenuation, which should be minimized.
- **Room temperature cure**: due to the different thermal expansion coefficient of the two crystals and of the bonding material, a room temperature cure is desirable to avoid the introduction of additional stress at the bonding surfaces.
- **Low viscosity** would help to spread an even and thin layer of glue on the surface, helping the transmission of acoustic waves.
- **Full curing Time at room temperature** must be between the 24 and 36 hours, with setting time of about 15 minutes.

Different types of glues have been examined and the lens cement glues have the correct physical properties except the UV radiation to activate the curing process. The ones listed below do not required UV curing and fulfil the additional requirement:

- Summer Optical Lens Bond F-65
- Summer Optical Lens Bond RD3-74
- Araldite 2020

The acoustic properties of the glues are difficult to predict and no values are reported by the supplier, therefore in order to determine the transmission coefficient of the different glues an acoustic experiment has been carried over using the pulse-echo rig and an acousto-optic tests, initially bonding two different substrates made of TeO_2 with the same orientation and assuming the theoretical transmission equal to 100%. Once the glue with best acoustic performance is identified, a Calomel cell and the acoustic prism with an ultrasonic transducer is bonded to create an acousto-optic device.

6.7 Pulse-echo measurement: Setup

The acoustic wave transmission between the two different substrates was measured by means of a pulse-echo techniques, which requires an interface solid/air identified as second interface (Fig.6.2), parallel to the transducer face. A special device mount has been designed and built, which allow to test different bonded samples; the device mounted is realised in Polyoxymethylene (Delrin) (Fig.6.2) in order to avoid to damage the Calomel crystal when used. The material choice has been dictated by the incompatibility of calomel with non-noble metal layers, which would cause corrosion,

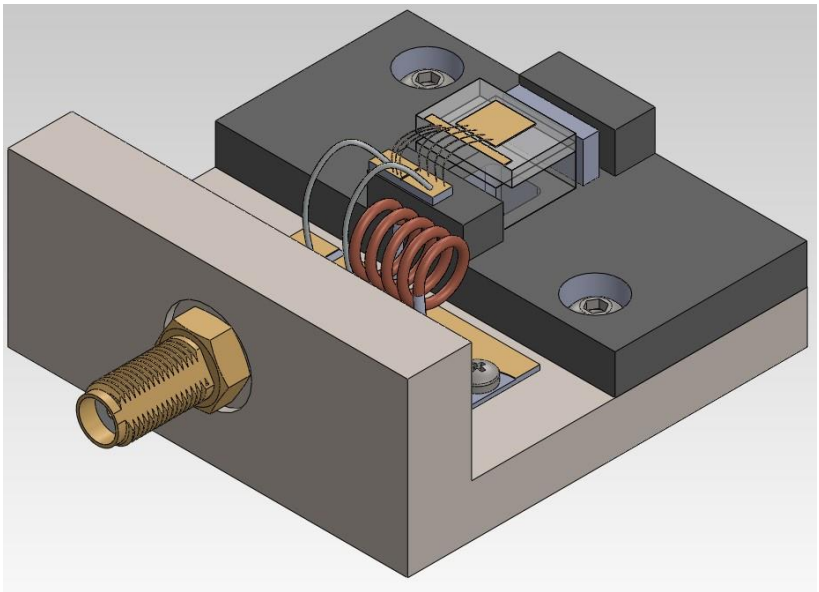

Figure 6.2: Device to measure the transmission of the acoustic wave between two materials bonded with glue

gradually destroy the bond and damage the crystal

The effect of the bonding layer on the transmission coefficient is measured from the amplitude of echo detected by the ultrasonic transducer reflected from the interface between TeO_2 and Hg_2Cl_2 and between Hg_2Cl_2 and air, where the ratio between amplitudes of two adjacent peaks gives the reflection coefficient of the interfaces.

A slow shear wave propagating along the [110] direction has been selected in both substrates because the acoustic walk-off is zero, therefore the acoustic pulse time of flight is determined only by the sample thickness. The first substrate bonded with the ultrasonic transducer has a thickness equal to 1.9 mm and 5.0 mm for the second substrate, the phase velocity (V $=$ 616 m/s) is the same in both substrates.

The transmission coefficient theoretically is equal to 1 and no reflected wave should be detected from the first interface, in practice the presence of a glue layer reduces the transmission coefficient due to the different elastic properties.

The experimental test bonding TeO_2-TeO_2 shows that the glue layers affect significantly the transmission coefficient and "spurious echo" reflected by the first interface are detected by the transducer, as shown in Fig.6.3(c).

A routine has been developed in order to determine the time distribution of all the reflection coming from both interfaces when the substrates thickness are defined by the user, and markers are automatically added to identify the "expected position" of each echo source.

The glue layer has been considered to determine the different source of the signal detected at the transducer level, therefore the first series of echoes is comes from the first interface, and the second from the solid/air interface; the third comes from a more

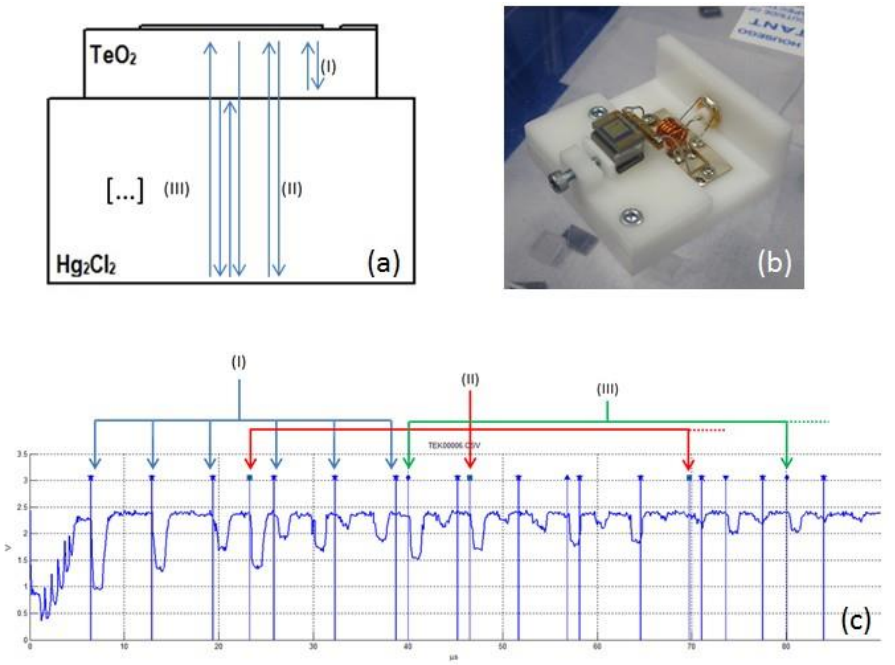

Figure 6.3: Diagram of the possible acoustic paths inside the crystals (a). Photograph of the device to assess the quality of the bonding obtained with the glue layer (b). the Experimental results obtained from the pulse-echo RIG of two TeO_2 samples bonded with Araldite 2020 (c).

complex reflection (Fig.6.3(a)).

Several substrates with a bonded transducers have been prepared) and due to the manufacturing tolerance the average thickness of the substrate is equal to 1.9 mm ± 0.001 mm, due to the variation of the transducer thickness and bond thickness between the ultrasonic transducer and the TeO_2 substrate. The tolerances introduce an error in the estimation of the time of flight which is equal to 0.100 μs, which is beyond the detectable signal from the pulse echo Rig. The second substrate in TeO_2, which represents the AO cell, has thickness of 5 mm ± 0.001 mm.

The experimental results shows a good agreement with the prediction obtained from the mathematical model developed, but the coupling coefficient was difficult to estimate due to the RF power detector which is not calibrated, therefore the only significant results obtained is the verification of the correct acoustic mode excited in both substrate and the effect of the glue layer used as a bond material.

The best results have been obtained from "Araldite 2020" (Fig.6.3), which has been selected to be used with Calomel substrates polished by BBT.

6.7.1 Bonding experiment: Calomel

The phase velocity in Calomel single crystal along the 110 direction is equal to 347m/s, and power reflection coefficient for an ideal bond obtained contacting TeO_2 and Calomel is equal to 16%. In the real device the glue layer's presence will increase the reflection coefficient. Experimentally using the F-65 and RD3-74 no echoes from the second interface could be detected by the pulse-echo Rig, and the only possible conclusion is no acoustic wave are efficiently coupled inside the Calomel substrate. Araldite 2020 shows a reaction with the Calomel cell due to the primer, and it seems that free mercury is released from the interface, helping the acoustic coupling between the substrate due to the presence of a bond layer, which gradually changes its composition from glue to mercury with an equal acoustic impedance at the interface with Calomel crystal. The pulse echo measurement shows the presence of only one echo coming from the interface air/solid. In order to have additional information, an acousto-optic experiment has been realized using the cell as a deflector, which is the topic of the next section.

6.8 Acousto-Optic Test

The Acousto-Optic test will indicate the acoustic coupling coefficient between the bonded substrates, comparing the measured diffraction efficiency versus RF power applied to the transducer, and it will be used as a reference. The theoretical values of the expected diffraction efficiency considering a *perfect* bond between the transducer and AO cell.

The Bragg condition is obtained for any internal incident angle θ_i for different wavelengths but only a limited interval can be use due to the cell dimension, therefore a routine has been developed in order to predict the performance of the AO interaction and RF frequency to achieve phase matching condition for the range of allowed angles. The acoustic field is considered equal to the electrode size and near-field effects and diffraction of the acoustic wave have not been considered for simplicity. A laser source with an emission at 1550 nm has been selected due to the low power requested to achieve peak diffraction efficiency and the relative low frequency. The diffraction efficiency is determined by Eq.4.10, proposed again below

$$\eta = \sin^2 \left\{ \frac{\pi}{\lambda_0 \cos\theta} \sqrt{\frac{M_2 L P_a}{2H}} \right\} \tag{6.5}$$

where L and H are the transducer dimension, P_a is the RF power, θ is the input angle, λ_0 is the laser wavelength and M_2 is the acousto-optic figure of merit [6]:

$$M_2 = \frac{n_i^3 n_d^3 p_{eff}(\theta)^2}{\rho V(\theta)^3} \tag{6.6}$$

where:

$$p_{eff} = \frac{p_{11} - p_{12}}{2} \cos^2(\theta) + p_{44} \sin^2(\theta) \tag{6.7}$$

In the case of tellurium dioxide single crystal the photoelastic constants are: $p_{11} = 0.0074$, $p_{12} = 0.187$, $p_{44} = -0.17$.[6]. In case of Calomel single crystal the photoelastic constants are: $p_{11} = 0.551$, $p_{12} = 0.44$, the value of p_{44} is unknown in the literature. The acoustic velocity is along the $< 110 >$ direction then $\theta = \pi/2$ and $p_{eff} = 0.0555$. For a given wavelength, the theoretical value of M_2 is given and from Eq.6.5 the RF power transmitted inside Calomel single crystals could be inferred. The phase matching condition is obtained by changing θ_i rotating the device and modifying the RF frequency applied to obtain Bragg diffraction. Theoretically the phase matching condition has been estimated by a dedicated Python routine developed by the author, which evaluate the acousto-optic properties for four different wavelengths and a given electrode size and RF power applied. The RF frequency and diffraction efficiency shown in Fig.6.4 were estimated for an RF power of 0.5 W an electrode with dimension of 5.0 mm × 5.0 mm, and an interval of θ_i between 0 and $\pi/4$.

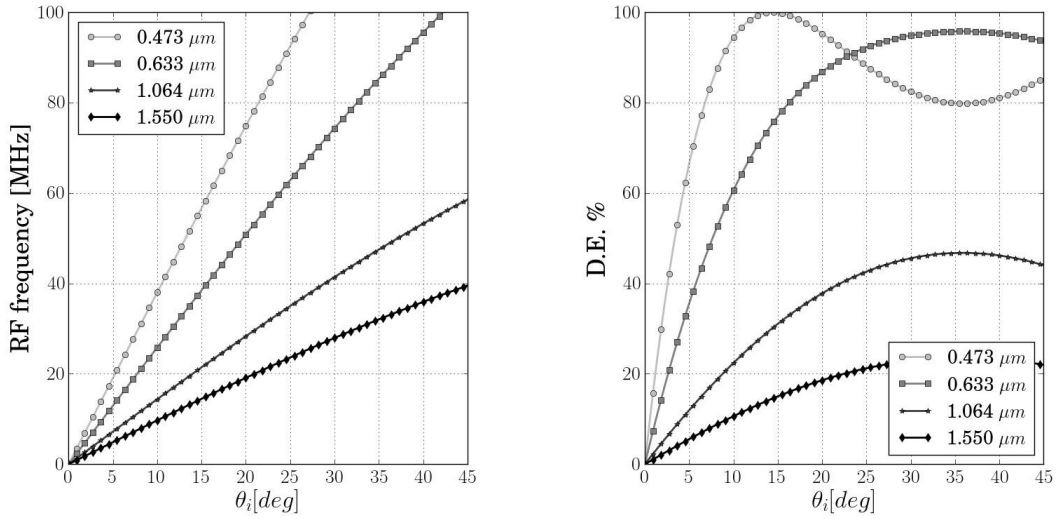

Figure 6.4: RF frequency to satisfy the phase matching condition for different wavelengths versus incident internal angle (left) and the diffraction efficiency D.E. versus incident internal angle (right).

The RF frequency is limited by the centre frequency of the transducer, therefore the

wavelength has to be choose accordingly with the available interval of θ_i determined by the geometry of the cell.

6.9 Experimental Results of the Acousto-Optic test

The AO cell used to measure the diffraction efficiency has the following dimensions: 5.0 mm [110] × 10.0 mm [$1\bar{1}0$] × 10.0 mm [001] (Fig.6.5) and the maximum external θ_i is approximately equal to 25°.

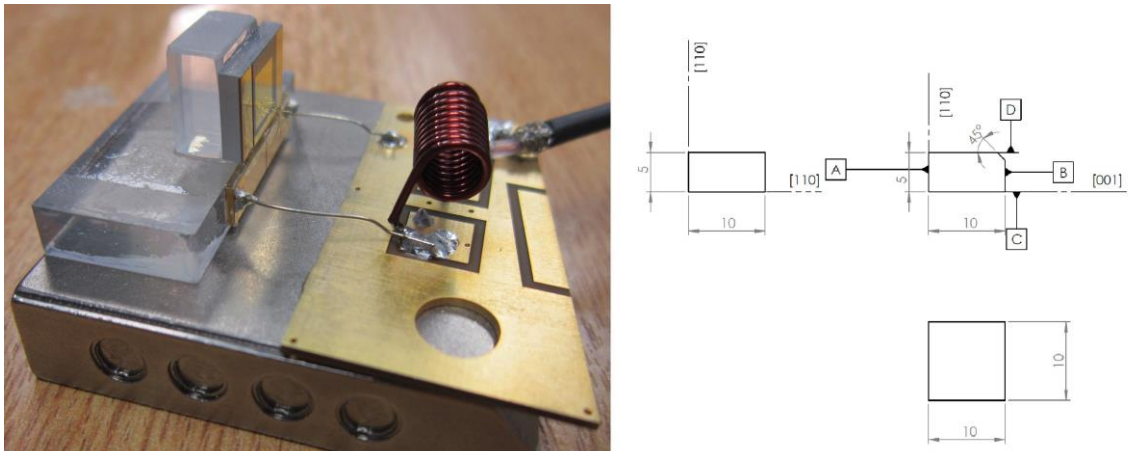

Figure 6.5: Test device built to measure the acoustic transmission (a), and the cell design.(b)

The RF frequency needed to satisfy the phase matching condition has been recorded equal to 33 MHz for an approximate input angle $\theta_i \simeq 11^\circ$ internal, and a diffraction efficiency equal to 50% using Leans Bond F65 and equal to 55% using Lens Bond RD3-74, which is lower by approximately 5% - 10% compared to the prediction due to the presence of the glue layer.

The performances achieved with the bonded Calomel cell are strongly affected by the glue layer, which is also confirmed by the pulse-echo results with an RF power of about 0.5 W and diffraction efficiency equal to 8%. The excitation of the correct acoustic mode has been verified by the Schaefer-Bergmann pattern obtained at 632.8 nm (Fig.6.6)

The bright dots visible in Fig.6.6 are due to the constructive interference of spurious acoustic waves for the applied drive frequency; the slowness curve of the slow shear is visible in the SB pattern confirming the excitation of the correct mode inside the Calomel crystal.

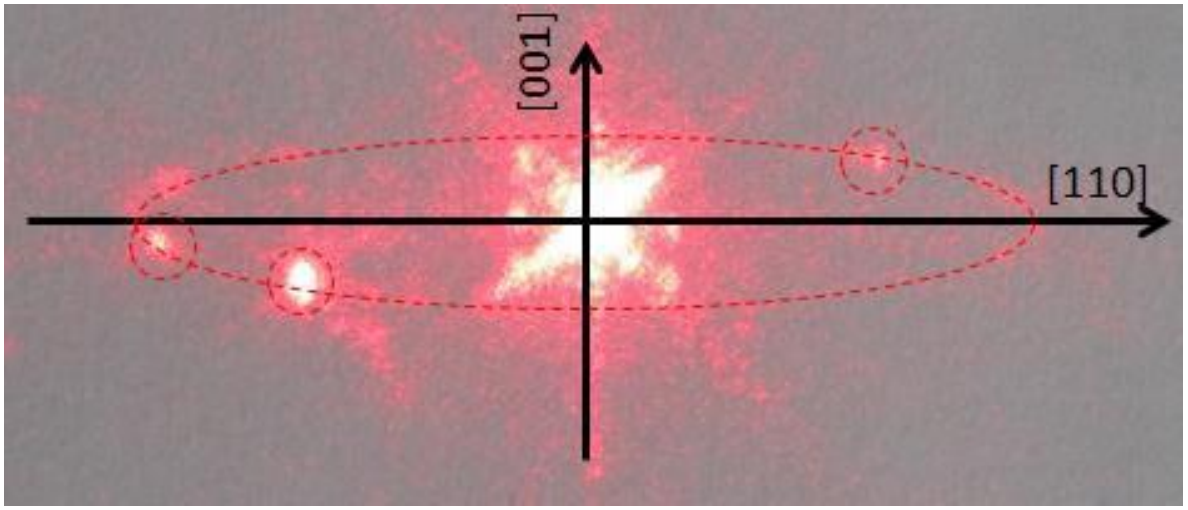

Figure 6.6: Schaefer-Bergmann pattern obtained by the slow shear.

6.10 Bonding Trial results

The results obtained from the different glue bonding TeO_2 over TeO_2 show relative good acoustic coupling between the two samples, confirmed by the pulse-echo and acousto-optic tests. Different results have been obtained when bonding the TeO_2 substrate to the Calomel crystal, because no echo has been detected from the second interface (Calomel/air) using all the three different glues identified. The acousto-optic test shows that some degree of acoustic coupling is achieved only with Araldite 2020, perhaps due to the presence of free-mercury release at the surface by the activator (Fig.6.7).

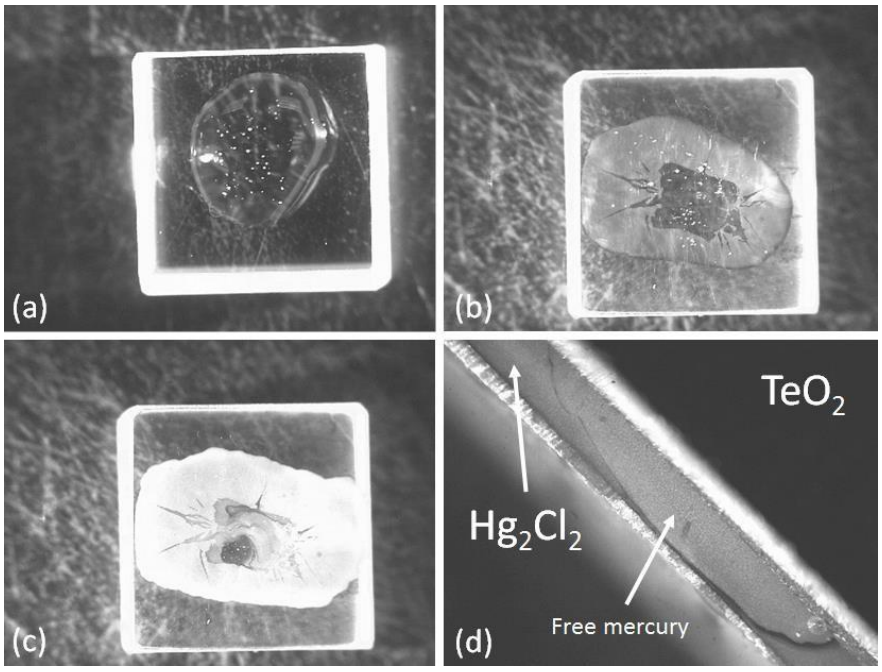

Figure 6.7: The effect of the activator used with Araldite 2020 on Calomel cell after t = 0 [s] (a), 20 [s] (b), 40 [s] (c), after full curing 48 hours (d)

The free mercury is confined inside the bond layer creating a transition from TeO_2 to Calomel, Araldite 2020 has been used to build the first prototype of the Calomel AOTF; the results reported in the next section.
Unfortunately, the experimental results cannot be easily compared against the model prediction because the current development of the bonding process does not show good repeatability. This is due to the difficulties of obtaining repeatable thickness and identical chemical composition of the adhesive layer, hence the acoustic transmission of the bonding layer is difficult to estimate in each case.
In addition, the continuity of the polarization vector for the acoustic waves between the two materials is always satisfied for any direction of propagation in the *t[110]-Z[001]* for both crystals.
The orientation of the acoustic substrate has to be determined in order to maximize the acoustic transmission for the selected direction of the acoustic wave in the AOTF.

6.11 First prototype of Calomel AOTF in a non-collinear configuration

The first prototype of an AOTF made of Calomel was designed in a non-collinear configuration under the parallel tangent matching condition, with a tuning range which covers the wavelength range from 1 μm and 2 μm; the wavelength range has been selected to cover the spectrum of the available white light source and the available optical spectrum analyser range. The input direction was equal to $\theta_i = 10.13^\circ$ and the acoustic direction equal to $\theta_a \simeq$ -85.0°, the tuning relation is shown in Fig.6.8(a) and the passband is shown in Fig.6.8(b).

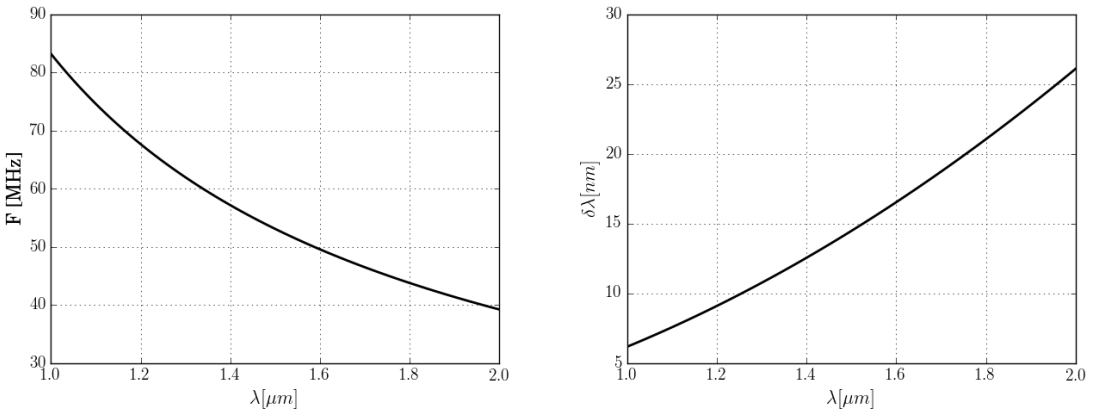

Figure 6.8: Tuning range of the first prototype(a) and related passband (b).

The interaction length is determined by the electrode dimension, which is bonded to

TeO_2 substrate (RD3060 - in the appendix). The bonding face of the Calomel cell is oriented along the [001] axis and the acoustic wave direction is determined by the angle of the prism, applying the Snell's law to the phase velocity in the two material.s

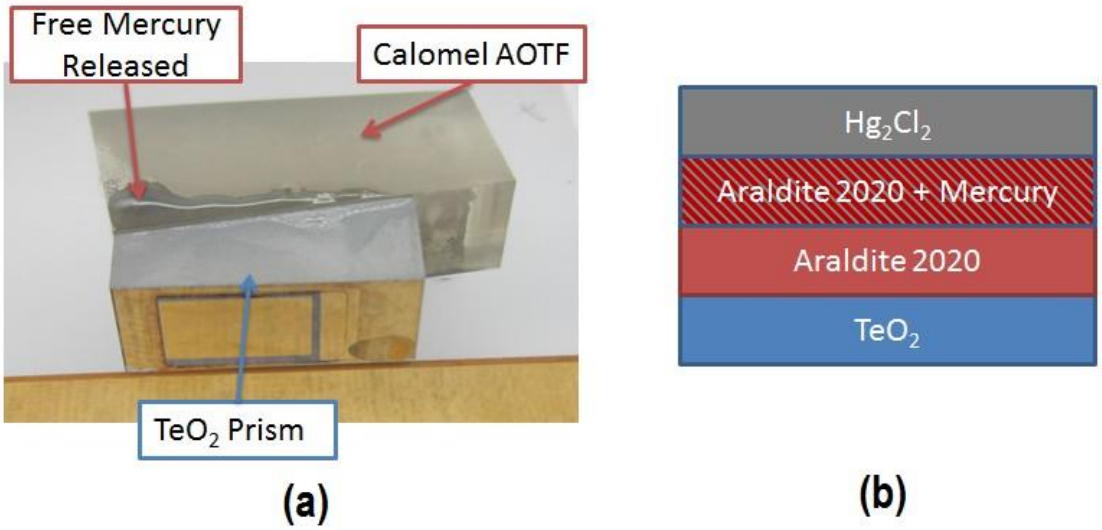

Figure 6.9: Photograph of the non-collinear bonded cell (a) and the diagram of the layer at the interfaces.(b)

In order to maximize the transmission of acoustic waves from TeO_2 in to the Calomel, the acoustic direction inside the substrate has been selected along the [110], where the phase velocity reaches a minimum; the angle between the transducer and the bonding face in the TeO_2 substrate is equal to 8.36° in order to launch acoustic wave in the desired direction inside the calomel crystal. The angle is easily determined by:

$$\frac{\sin(\theta_i)}{V(\Theta_i)} = \frac{\sin(\theta_r)}{V(\Theta_r)} \tag{6.8}$$

with Θ_i and Θ_r are measured from the perpendicular to the surface, θ_i and θ_r are relative to the crystallographic orientation using Fig.6.10 as reference.
The theoretical transmission coefficient in case of direct contact between Calomel and Tellurium Dioxide is equal to 83%, due to the acoustic impedance mismatch determined by the direction selected in TeO_2. It was selected a propagation direction along the 110, where the acoustic walk-off is zero, and the acoustic direction in the Calomel cell is the same. In reality the presence of the bonding layer will affect the transmission coefficient increasing the RF power versus diffraction efficiency, leading to a reduced acoustic power inside the calomel cell.

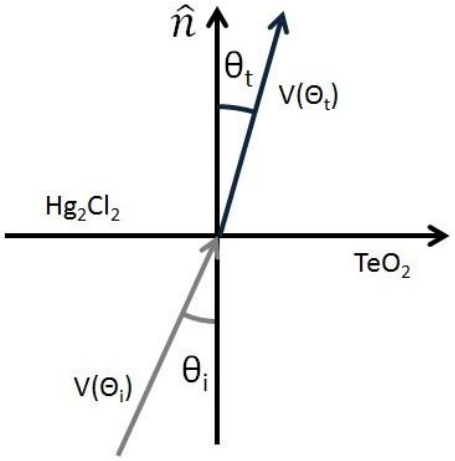

Figure 6.10: Reference angles used to predict the acoustic direction of transmitted acoustic waves applying the Snell's law.

6.12 Experimental results

Two AOTFs with the configuration described in the previous section have been built and tested using Araldite 2020 as bonding material. The TeO_2 prism has been bonded to the face C (refer to appendix) and the acoustic direction is equal to θ_a = -85.0 °.

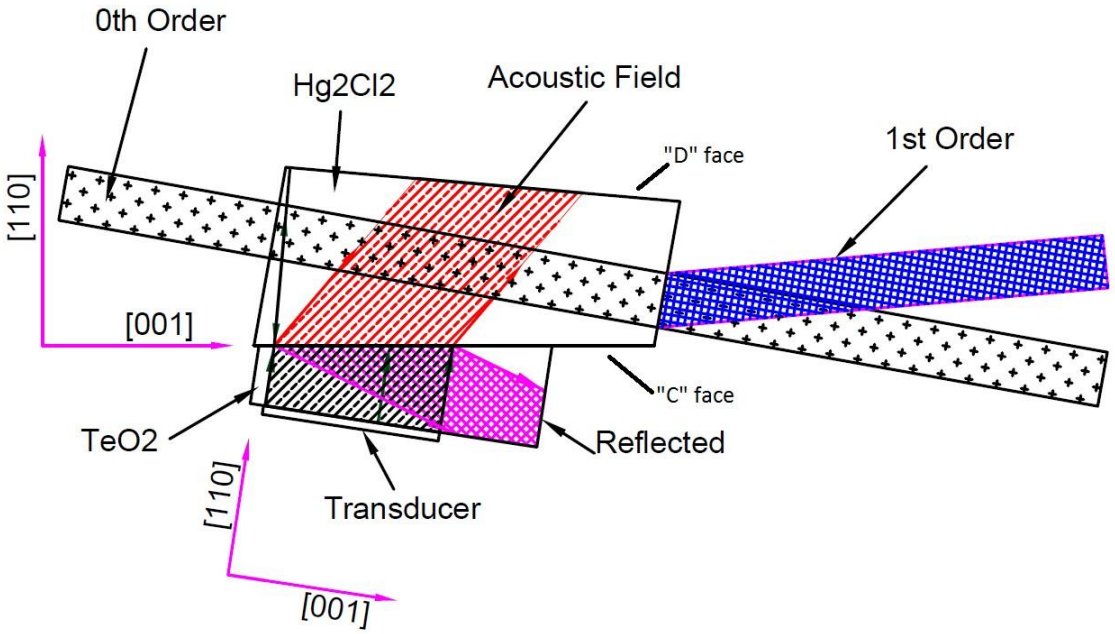

Figure 6.11: Schematic of the non collinear AOTF made of Calomel, where the acoustic field is shown in each parts of the device.

The transducer has been matched to a centre frequency of 49.2 MHz, which corresponds to 1550 nm; the diffraction efficiency of the first device is equal to 10% for an

RF power of 1.843 W, the second device showed a diffraction efficiency of about 40% for an RF power equal to 1.8 W.

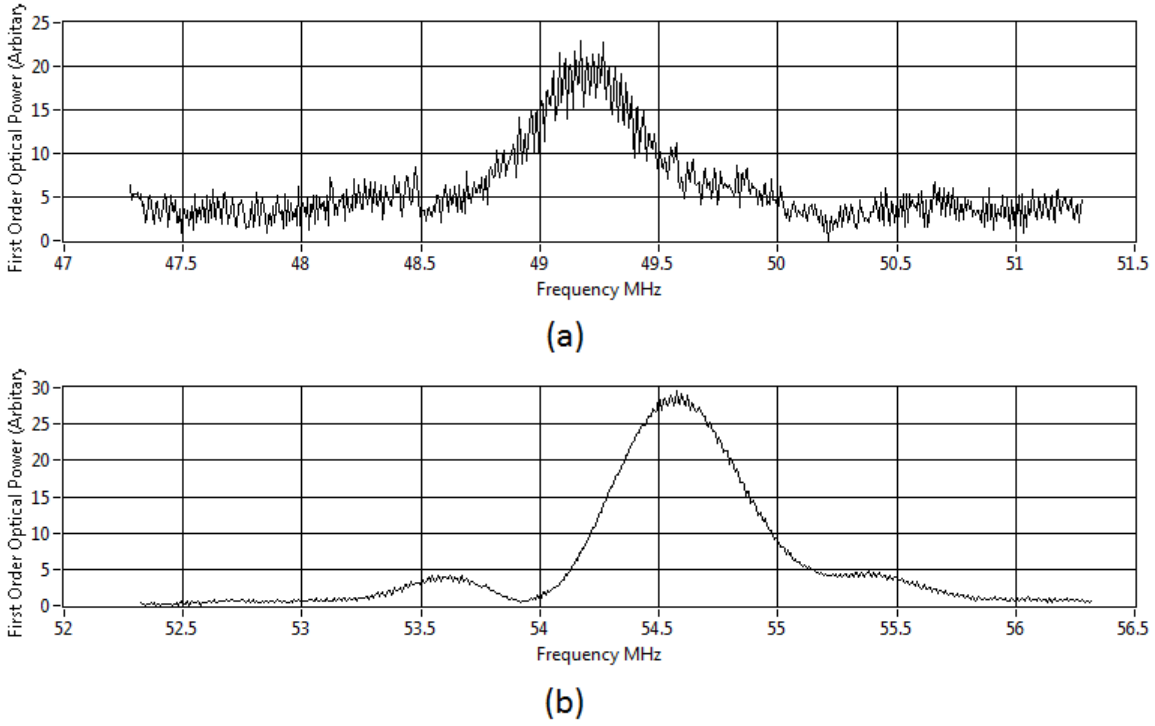

Figure 6.12: Experimental results obtained with the TeO_2 substrate bonded on the face "D" (a)and on the face "C" (b).

The AOTF cell has been configured in such way, that the Face "D", opposite to transducer, could be bonded with the same prism and have the acoustic wave propagating along the [110] direction; under this condition the phase matching is achieved at 68 MHz for a wavelength equal to 632.8 nm, where the diffraction efficiency was measured at 10 % for an RF power equal to 0.3 W.

The theoretical tuning relation shows good agreement with the results obtained from the preliminary test of the first prototype, but the diffraction efficiency measured could not be compared with the theoretical model due to the presence of the glue layer and the unknown values of p_{44}, which was set to zero. The transmission coefficient at the interface can be estimated by bonding the substrate to the opposite face, the acoustic direction is then along the [110] axis, hence the effective photoelastic constant is defined by Eq.6.7. Then the RF power versus diffraction efficiency can be predicted and the coupling coefficient between the two material can be inferred.

The measured diffraction efficiency was in the range between 1% - 3% at 1550 nm with $f = 60.31$ MHz and $P = 2$ [W], therefore the coupling coefficient has been inferred to be between 7 dB and 10 dB.

6.13 AOTF design Optimization

In the literature this material is well characterized and several papers have been published about its use in acousto-optic modulators (AOMs) due its high Acousto-Optic figure of merit compared to TeO_2 with the longitudinal mode. In the case of acousto-optic devices exploiting the slow shear interaction for an arbitrary acoustic propagation direction in the t[110]-Z[001] plane, the effective photoelastic coefficient is a linear sum of various tensor components, but it is not possible to optimize the design because one value of the photoelastic constants (p_{44}) is currently unknown.

Calomel single crystal is characterized by a modest figure of merit and limited birefringence for the wavelength range of interest, which limit the performance for wavelengths above 5 μm. A comparison between the different M_2 of several AO material useful for AO application are reported by Gupta et al. [39] and shows the limitation of Calomel as AO material for Infra-Red application; in addition the AOTF performance is strongly dependent on the values of p_{44}, which is unknown.

The non-collinear configuration shows its limitation for wavelength above 4.5 μm due to the limited birefringence, where the usable interval of θ_i is limited by the values of M_2 and the extension of the tuning range is determined by maximum frequency (Fig.6.13).

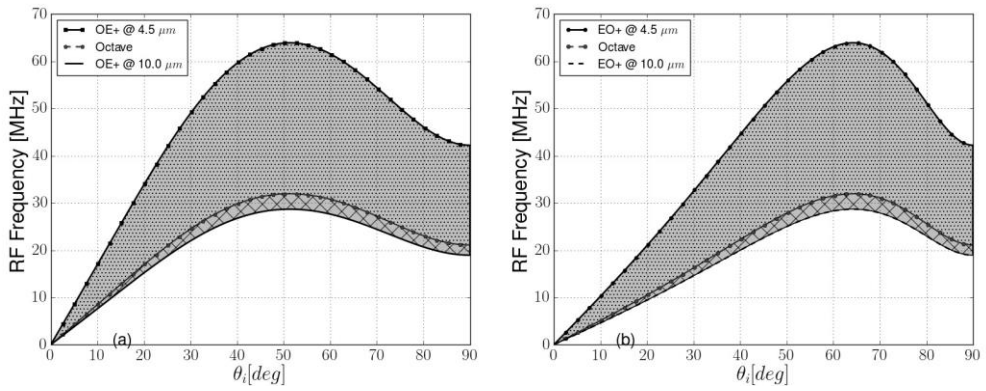

Figure 6.13: RF Frequency versus θ_i for the wavelength range between 4.5μm and 10 μm for the OE+ (a) and EO+ (b) where the octave region is shown by shaded region

.

The octave was shown in Fig.6.13 by the dotted area, therefore it is not possible to cover the whole range from 4.5 μm to 10 μm with a single device with an octave of tuning span, in addition the ultrasonic transducer does not work efficiently for frequencies below 15 MHz. In conclusion the additional constraint are added to θ_i, which should be greater than 10.0 °, achieved at the expense of the efficiency of the AO interactions. This increases the RF power consumption, assuming a conventional bonding technique is used and p_{44} equal to zero.

The RF power versus peak diffraction efficiency can be reduced by maximizing the ratio L_a /H[1]. In case of a non-collinear configuration the minimum ratio required to not exceed 5 W is theoretically estimated to be equal to 20, with the help of a dedicated routine design developed in Python. In practice due to material size limitation the maximum ratio is below 2.5 leading to non-efficient devices (Fig.6.14).

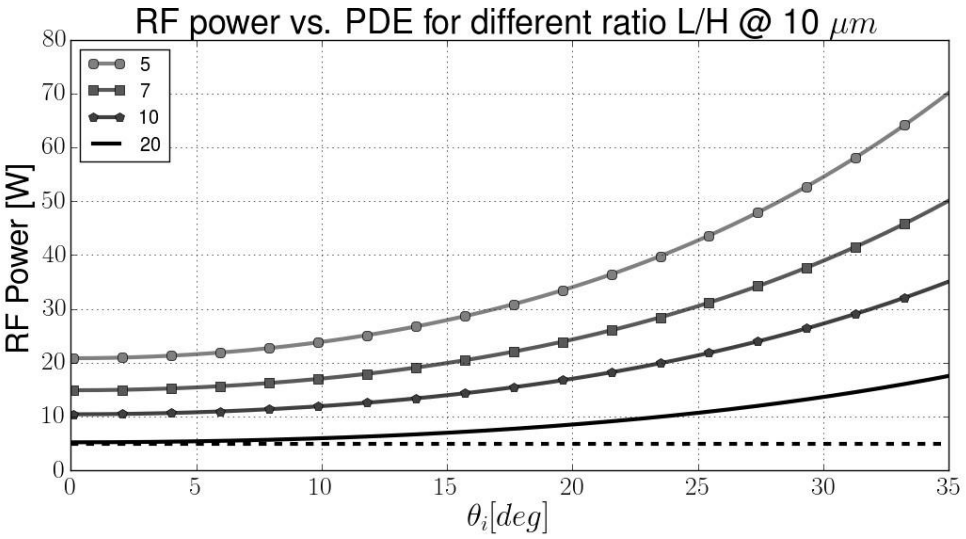

Figure 6.14: RF power for peak diffraction efficiency with different dimensional ratio of the transducer.

The effect of p_{44} on the AOTF's performance has not been considered in the previous analysis, in order to complete the feasibility study and optimize the AOTF design to maximize the performance the values of all the photoelastic constant should be known. The next section is dedicated to the missing photoelastic constant p_{44}, where its effect on the AOTF performance is theoretically estimated and an experiment is proposed to measure the value of p_{44}.

6.14 The Quasi-Collinear configuration

The non-collinear configuration is often used for a non-coherent source or in imaging system, the limited interaction length limits the diffraction efficiency achievable due to the practical limit imposed by the RF power. The RF power consumption could be reduced maximizing the ratio L_a/H obtained with the quasi-collinear configuration; this type of AO interaction requires a well collimated source with diffraction limited output, such as obtained from a supercontinuum source.

[1]It is reminded to the reader L_a is the interaction length, determined by the length of the electrode, and H is the height of the electrode.

The optimal configuration of the acousto-optic interaction is investigated by a dedicated routine developed in Matlab, which estimates θ_i for any direction of θ_a and the relative RF frequency required to satisfy the phase matching condition and M_2 for three different value of p_{44}.

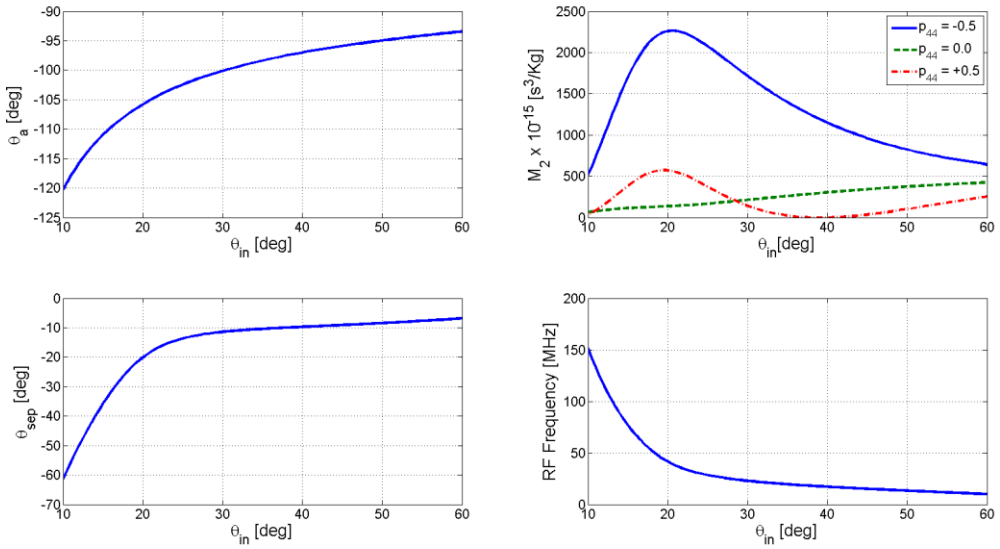

Figure 6.15: Relation between θ_i and θ_a(a). Different values of M_2 using different values for the missing photoelastic constants p_{44}(b). Internal separation angle versus θ_{in}(c). RF frequency to achieve phase-matching condition for different incident angles(d).

The acousto-optic figure of merit (M_2) is affected by the value of p_{44}, an improvement of M_2 is obtained independently of the p_{44} sign for $\theta_i < 28^\circ$, as shown in Fig.6.15(b) and in addition the RF frequency to achieve phase matching condition is above 25 MHz for $\lambda = 10\ \mu$m, where conventional transducers work more efficiently, leading to an optimal configuration for the AO cell independently of the value of p_{44}.

6.15 Calomel QC-AOTF

A first prototype was designed with $\theta_a = -96^\circ$, $\theta_i = 43.84^\circ$, H = 3.0 [mm], $L_a = 21$ [mm], and $p_{44} = 0$; the predicted performance is shown in Fig.6.16.

The diffraction efficiency is theoretically predicted with no attenuation introduced at the interface between TeO_2 and Hg_2Cl_2 as shown in Fig.6.16(e). A TeO_2 prism was designed to maximize the acoustic transmission between the two materials, not taking into account the effect of the bonding layer. The transducer face, perpendicular to θ_a has been tilted by angle of 5.0° in order to use a TeO_2 prism to avoid residual acoustic waves reflected backward creating standing waves, therefore a conventional TeO_2 shim with parallel faces should be avoided because the reflected acoustic wave will then be

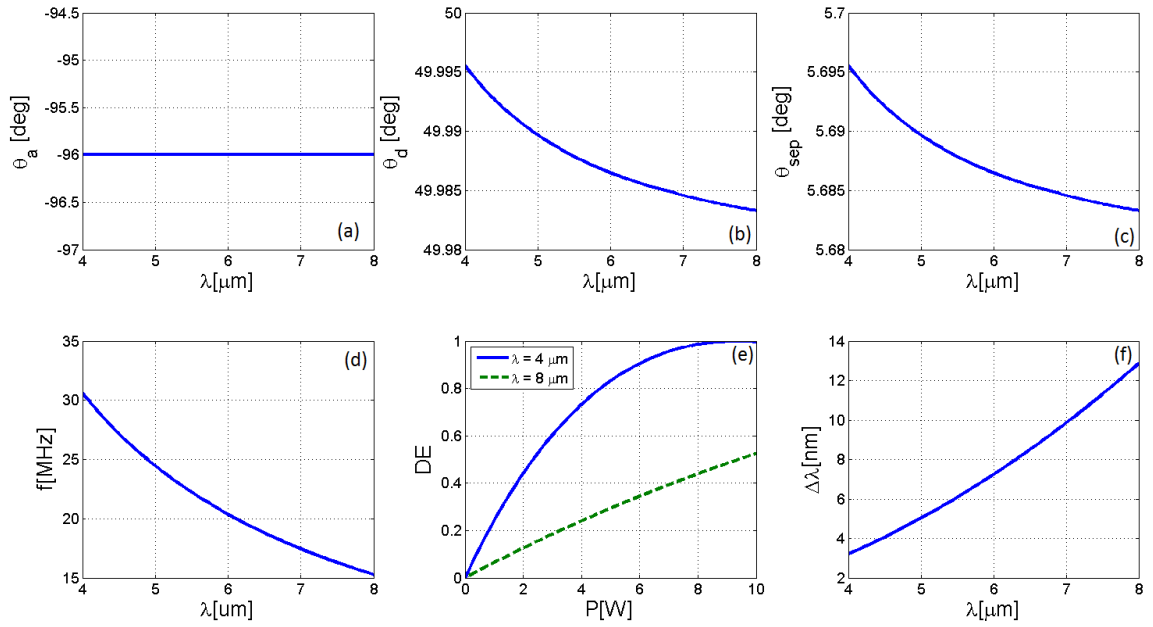

Figure 6.16: Acoustic velocity direction versus λ to achieve phase matching(a). θ_d versus wavelength (b). Separation angle between the 0^{th} and 1^{st} order (c). Tuning relation (d). Diffraction Efficiency (DE) versus RF power (e). Passband versus wavelength (f).

back-reflected the transducer with the same problem of a resonant AOTF. The angle of the prism have been estimated applying the Snell's law, with $\theta_a(IN) = 85.0^\circ$ (V = 634.38 [m/s]) in TeO_2 and $\theta_a(OUT) = 67.1^\circ$ (V = 529 [m/s]); θ_t is defined by the AO cell configuration and θ_{in} is determined solving by:

$$\theta_{in} = \arcsin\left(\frac{V_{TeO_2}}{V_{Hg_2Cl_2}}\sin\theta_t\right) \tag{6.9}$$

using Fig.6.17 as reference.

The AO cell has been configured with parallel faces between 'C' and 'D' faces (Fig.6.17(a), therefore the AOTF could be configured as a resonance or conventional AOTF. The conventional AOTF is realized adding acoustic dumping to 'D' face, otherwise if the former face is left polished with an interface between air/solid, then the acoustic wave is reflected back on the same creating a resonant cavity.

The resonance frequencies are difficult to be recorded due to the presence of the glue layer, which does not give a significant feedback signal at the transducer level, therefore resonant frequencies are difficult to track; in theory the diffraction efficiency should increase significantly when the resonant frequency is selected. The thermal gradients are significant due to the RF power level needed to achieve a reasonable diffraction efficiency (> 50% for polarized light).

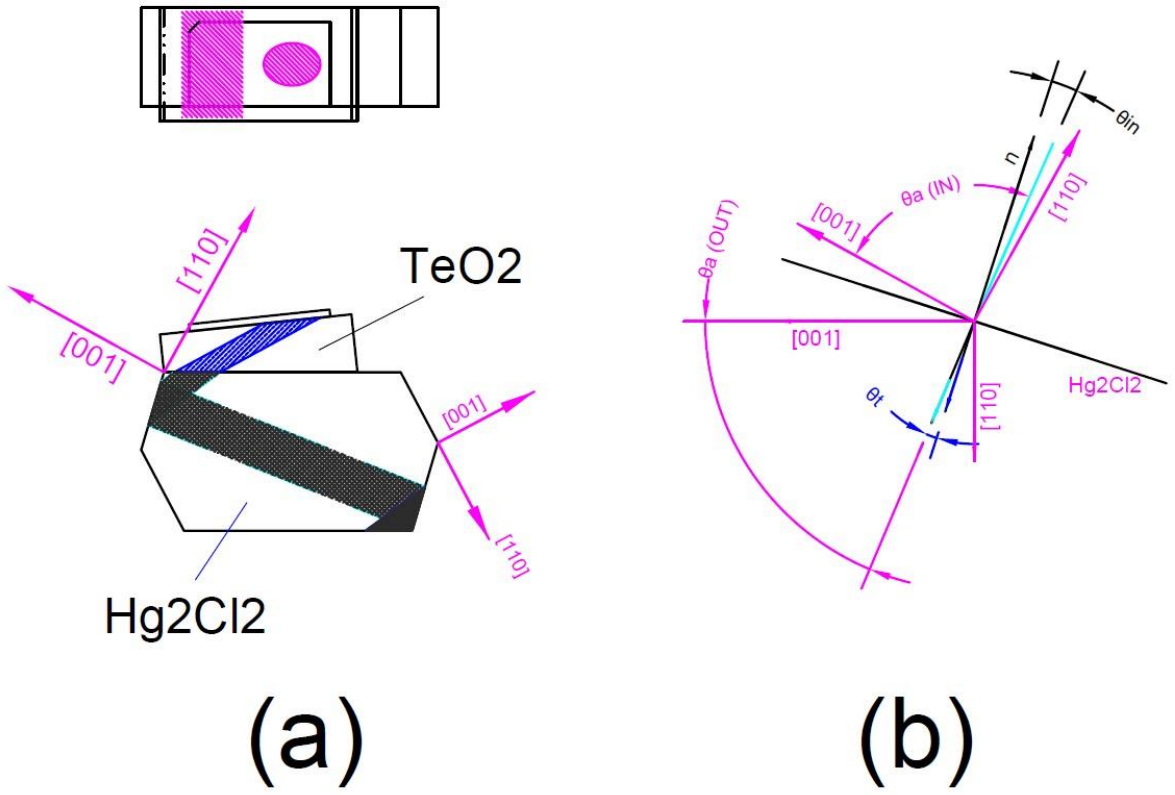

Figure 6.17: Quasi-collinear Calomel cell, top and lateral view(a), where the acoustic walk/off is marked by the shaded areas. Direction of the phase velocity inside the TeO_2 substrate and Calomel cell(b).

6.16 Calomel AOTF devices

AOTFs realised in Calomel and other crystals, which cannot be put in contact with non-noble metals, require particular attention in the design process of the housing, in order to remove the heat generated by acoustic waves. Temperature stabilization can be achieved by two different means: one is using double Peltier heat pump glued to the top and bottom faces, or using water cooling. The AO cell would be mounted on Pyrex glass in order to protect the cell and at the same time to improve the heat transfer to the metal base, a schematic of the AOTF is shown in Fig.6.18

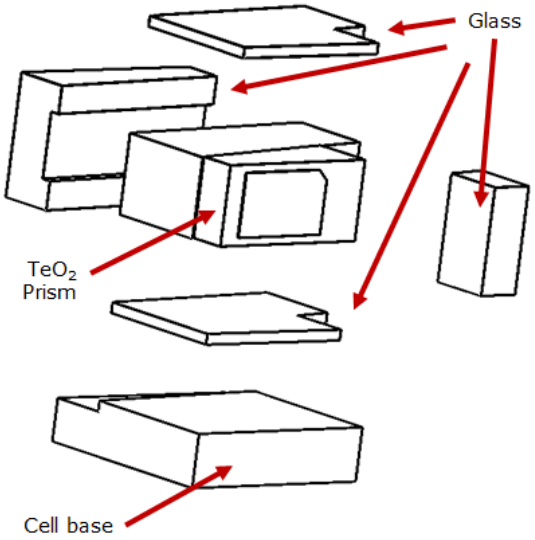

Figure 6.18: Proposed AOTF assembly to protect the Calomel single crystal from the cell base made of aluminium alloy.

The cell base is typically made of aluminium alloy, which cannot be used in contact with Calomel crystal. The glass mount can be easily fixed using Cyanoacrylate glues. If the solution using the Peltier is implemented then the two heat pumps can be bonded directly to the glass on the top and the bottom of the cell base.
The performance will be strongly dependent on the values of the missing photoelastic constant (p_{44}), the direct measurement is affected by the glue layer transmission coefficient, which is unknown. The effect of different values of p_{44} is theoretically studied in the next section and a technique to measure its value is proposed.

6.17 The effect on the AOTF performance of p_{44}

The effect of p_{44} has not been considered in the previous section, because no value is reported in the literature to the knowledge of the author in literature. One of the diffi-

culties in estimating p_{44} is caused by the necessity of developing non standard bonding processes, where the acoustic transmission coefficient of the bonding layer can not be estimated theoretically with sufficient accuracy.

The AOTF performance can be estimated for different values of p_{44}, which only affects the RF power versus diffraction efficiency. The peak diffraction efficiency is estimated theoretically for three different values of $p_{44} = [-0.5, 0.0, 0.5]$ (Fig.6.19), as it is possible to notice that the sign and the magnitude of p_{44} significantly affects the performance. If the unknown photoelastic constant has a negative sign, the RF power increases rapidly to an impractical level.

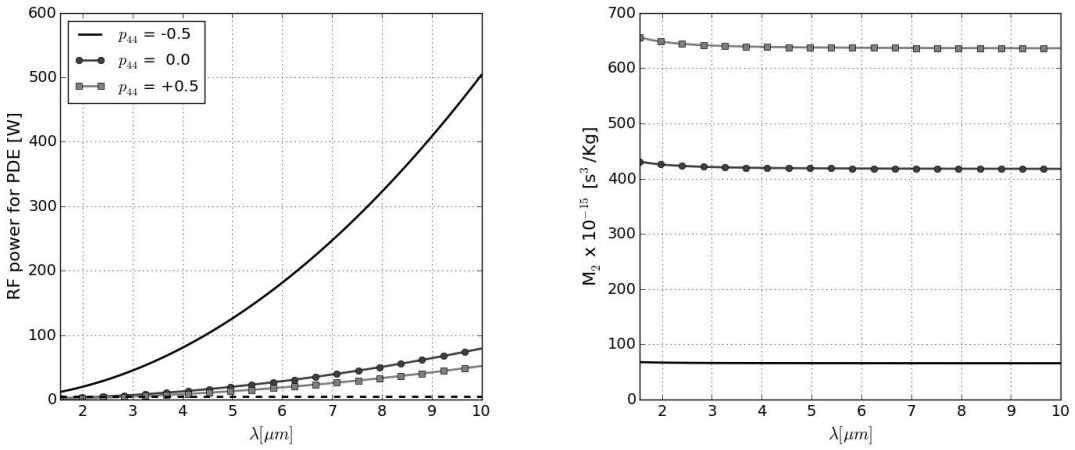

Figure 6.19: RF power for peak diffraction efficiency (PDE) versus wavelength for three different values of p_{44}(left). Acousto-Optic figure of merit versus wavelength for the three different values (right).

The estimation of p_{44} for Calomel is of major importance; a solution is proposed and theoretically could be extended to any other AO materials where a non-standard bonding technique is used. The methods described here allow one to eliminate uncertainties in acoustic coupling which would otherwise make this method indirect and hence inaccurate. The acoustic impedance mismatch between Hg_2Cl_2 and TeO_2 can be estimated theoretically by assuming direct contact between the two crystals, consequently for a given direction of the acoustic wave inside calomel, it is possible to determine the best orientation of the tellurium dioxide substrate. The acoustic impedance is defined as $Z(\theta_a) = \rho V(\theta_a)$, in case of TeO_2 the acoustic velocity is estimated from Eq.3.30 substituting $V_{110} = 616$ m/s and $V_{001} = 2104$ m/s and the density (ρ) is equal to 5990 Kg/m^3[17]. The reflection coefficient of the acoustic wave travelling from TeO_2 to Hg_2Cl_2 is determined by [17]:

$$T = \frac{Z_{TeO_2} - Z_{Hg_2Cl_2}}{Z_{TeO_2} + Z_{Hg_2Cl_2}} \tag{6.10}$$

where the acoustic impedance of each material depends on the direction of propagation of the acoustic wave, the general solution is shown in Fig.6.1(b), assuming the configuration in Fig.6.1(a).The maximum transmission coefficient achievable is equal to 90% not considering the effect of the bonding layer.

6.18 Evaluation of photoelastic constants

The photoelastic constants can be estimated by the diffraction efficiency (η) versus RF power applied to the ultrasonic transducer estimated by Eq.4.9, and reported below:

$$\eta = \sin^2 \sqrt{\frac{M_2 L_a P}{2\lambda H}}$$

where L_a is the interaction length and H is the height of the acoustic field. The values of M_2 (Eq.4.11) for a given wavelength, RF power, and H/L_a ratio can be obtained experimentally from Eq.4.9, hence the value of p_{eff} (Eq.4.30) is theoretically estimated.

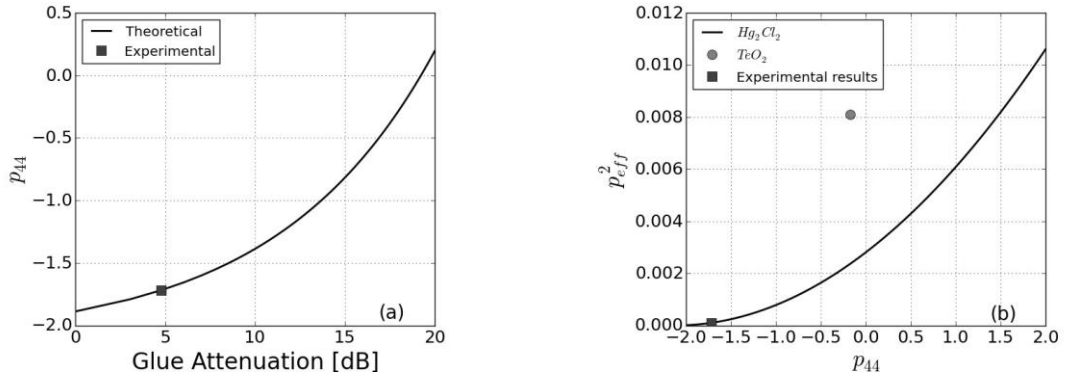

Figure 6.20: The estimated value of p_{44} versus the glue attenuation (a) and the value of p^2_{eff} versus p_{44} for Calomel and the value for TeO_2.

The missing photoelastic constant can be inferred by solving Eq.6.5 to estimate M_2

$$M_2 = \frac{2H\lambda^2}{L_a P \pi^2} \arcsin^2(\eta) \tag{6.11}$$

then p_{eff} is obtained solving Eq.4.11

$$p_{eff} = \sqrt{\frac{\rho V(\theta_a)^3}{n_i^3(\theta_i) n_d^3(\theta_d)} M_2} \tag{6.12}$$

and p_{44} is equal to

$$p_{44} = \frac{p_{eff} - p'_{66}\sin(\theta_a)\cos(\theta_d)}{\cos(\theta_a)\sin(\theta_d)} \tag{6.13}$$

using Eq.4.30. A possible value of p_{44} can be estimated from the measurement on the first prototype of the AOTF made of Calomel with θ_a = -85.0 [deg], θ_i = 15.13 [deg], where the glue layer attenuation and the acoustic impedance mismatch theoretically reduce the acoustic power between 0 dB 20 dB. The diffraction efficiency is considered fixed to 40 % for 1.8 W applied to the transducer in order to obtain comparable results. If a variation of the attenuation is introduced by the glue layer in the model then the acoustic power inside the AO cell is reduced and the efficiency of the AO interaction increases because D.E. level is achieved for lower acoustic power inside the AO cell, hence the p_{eff} increases as shown in Fig.6.20(a).

The experimental results of the first prototype with a bonded transducer to the 'D' face shows that the attenuation of the acoustic wave is about 6 dB, when crossing the interface between TeO_2 and Hg_2Cl_2; if it is assumed the same property are applied to the bond layer to the 'C' face, then the effective power inside the Calomel cell is equal to 0.6 [W] for a RF power level of 1.8 W giving a diffraction efficiency of 40 % at λ = 1.550 μm , and H/L = 0.625. The inferred p_{eff} = 0.010 from the experimental results and consequently p_{44} = -1.6 (Fig.6.20(b)). The negative value of p_{44} is affecting negatively the achievable performance in the long wavelength region (λ > 4.5 μm) as shown in Fig.6.19. The bond layer properties have been assumed the same, in reality the glue layer properties are strongly dependent on the bonding process, chemical composition , and environment effects, therefore repeatable results are not achieved at the current stage of development.

Due to the unknown transmission coefficient of the adhesive layer between TeO_2 and Hg_2Cl_2, it is not possible to directly estimate p_{44}, but the missing photoelastic constant can be estimated using a specially designed acoustic coupling prism with two transducers at different orientations, allowing exclusion from the measurements the coupling coefficient between this prism and the Hg_2Cl_2 crystal.

6.19 The AO interaction

The acousto-optic interaction has been theoretically estimated for two different acoustic directions. The acoustic wave directions have been selected to achieve the phase matching condition for a given direction of electromagnetic radiation. In the first interaction the acoustic wave propagates along the <110> and the transmission coefficient is estimated from the diffraction efficiency for a given RF power at a fixed wavelength,

because $\theta_a = \pi/2$ and $p_{eff} = (p_{11} - p_{12})/2$.

The second AO interaction is obtained for an acoustic wave propagating along a different direction, in order to maximize the acceptance angle, the phase matching condition between the acoustic wave and incoming electromagnetic radiations has been configured to satisfy the parallel tangent matching condition (Eq.4.6); the geometry of the AO interaction is shown in Fig.6.21, and estimated theoretically by a dedicated routine developed in Python.

The orientation of the transducers on the TeO_2 prism is determined applying the Snell's Law, at the interface Fig.6.22(a):

$$\frac{\sin \Theta_i}{V_{TeO_2}(\theta_i)} = \frac{\sin \Theta_t}{V_{Hg_2CL_2}(\theta_t)} \tag{6.14}$$

where θ_i and θ_t are the directions relatively to crystallographic orientation of the incident and transmitted elastic waves, and Θ_i and Θ_t are the directions to the normal of the interface. The solution of Eq.6.14 is found numerically, because the phase velocity change with direction inside the crystal due the anisotropic nature of the materials. Due to the anisotropy of the material the walk-off of the acoustic waves has been evaluated in order to determine the direction of the acoustic energy, in order to finalize the practical design.

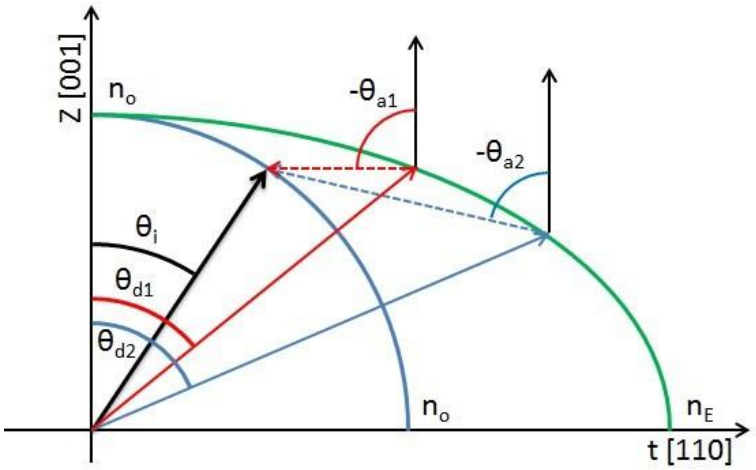

Figure 6.21: K-space diagram for the AO interactions with $\theta_{a1} = \pi/2$ and θ_{a2} arbitrary

6.20 Calomel cell configuration

The orientation of the input face is designed to satisfy the parallel tangent matching condition for a given direction of the acoustic wave ($-\theta_{a2}$), and the second transducer

is oriented along <110> direction to estimate the coupling coefficient.
The two AO interactions are configured in order to have the same input direction, but the RF frequency required to satisfy the phase matching condition should be the same in both case to have similar acoustic wavelength at the interface between TeO_2 prism and the Calomel cell. For this reason it is advisable to use two different wavelengths, because the phase matching condition in case of θ_{a1} is achieved for a RF frequency below 10 MHz, where the ultrasonic transducer made of $LiNbO_3$ does not work efficiently.
A particular case is proposed for illustrative purposes where the AO cell had been

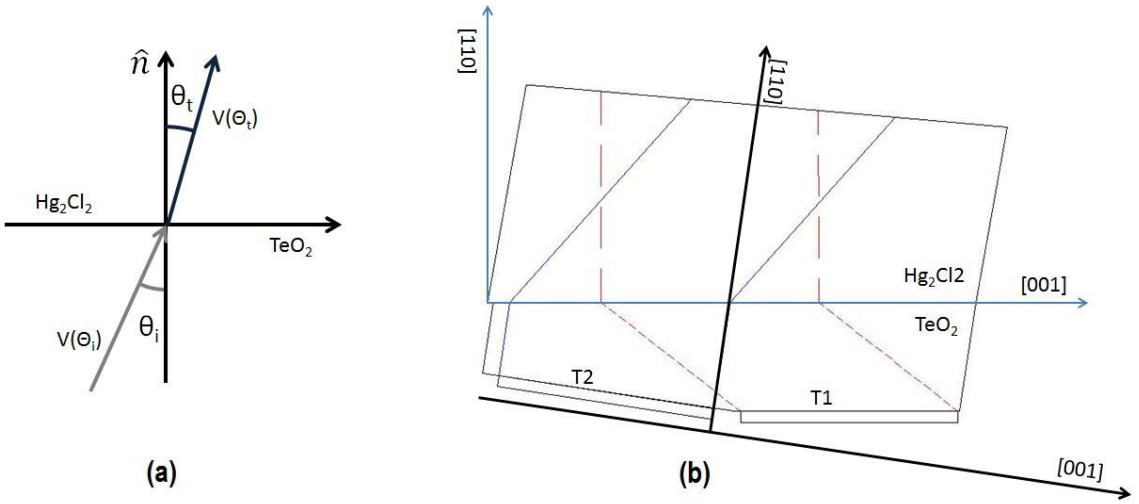

Figure 6.22: Schematic of acoustic transmission between two material(a), configuration of the AO cell made of Hg_2Cl_2 bonded with a TeO_2 substrate(b).

configured with an acoustic direction θ_{a2} = -80.5° and an input face of θ_i = 20.0° under parallel tangent matching condition. The expected RF frequency in the anisotropic AO interaction is approximately equal to 77 MHz for λ = 2000 nm for θ_a = -80.5°. For the acoustic wave propagating along <110> (for θ_a = - 90°) the expected RF frequency is too low for λ = 2000 nm, therefore another wavelength equal to λ = 632.8 nm has been chosen, where the theoretical RF frequency is equal to 29 MHz.
The bonding face of Calomel is parallel along the <001> direction and the prism has the following propagation direction θ_{a1} = -74.74° and θ_{a2} = -90° from the optical axis and the angle between the T2 plane and bonding face of Calomel is 15.26°. The direction of the first transducer has been configured between parallel faces, therefore two possible measurements can be carried over to increase the accuracy of the measurement of the transmission coefficient: one is using a pulse-echoes technique, and one is evaluating the diffraction efficiency for a given RF power at a specific wavelength.

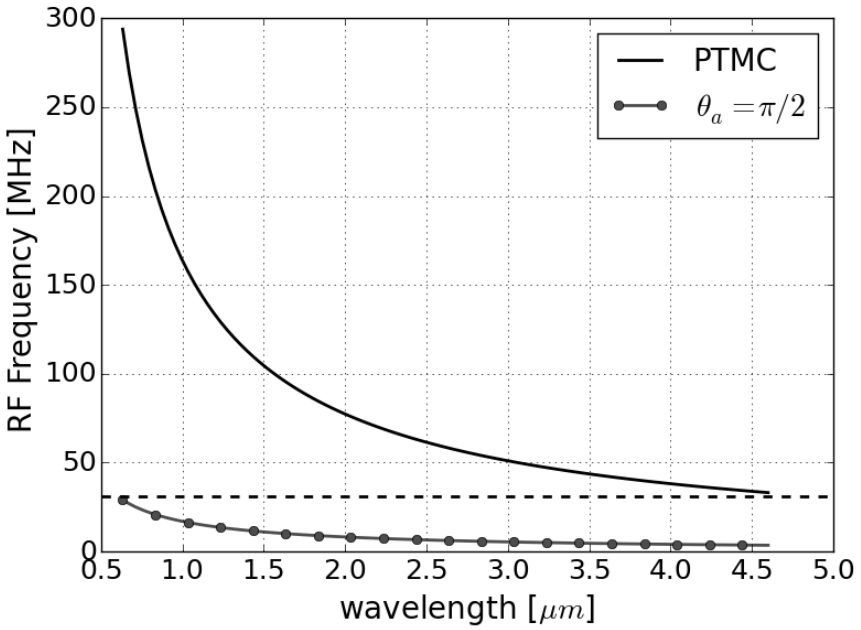

Figure 6.23: Tuning relation between the acoustic field from transducer T1, where the phase matching is satisfied under the parallel tangent matching condition, and the acoustic field from transducer T2.

6.21 Experimental setup and theoretical performance

The diffraction efficiency versus RF power for a given wavelength is measured by means of a standard laser line test, which consists of a laser source, RF synthesizer, RF power meter, and lock-in amplifier. The AOTF is aligned in order to achieve peak diffraction efficiency for both wavelengths using the lock-in amplifier with a sensor mounted on an integrating sphere (Fig.6.24).

The available source are an He-Ne laser at 632.8 nm and diode laser at 2000 nm, both vertically polarized corresponding to ordinary ray in the Hg_2Cl_2. A dichroic mirror is used to superimpose both lasers onto the same path,so they enter the Hg_2Cl_2 crystal at the same point and at the same θ_i. Due to the high refractive index and the absence of chromatic compensation at the output face, which is left parallel to the input face, the different wavelengths exit at different angles thus it is possible to separate them spatially. After the alignment is optimized, the RF power for peak diffraction efficiency will be recorded by relative measurement. Assuming a ratio L_a/H equal to 2 then the diffraction efficiency versus RF power is evaluated by Eq.4.9, for the first AO interaction the RF power for peak diffraction efficiency is estimated to be about 0.190 W. A margin of approximately 30% should be allowed due to the theoretical acoustic impedance mismatch between Hg_2Cl_2 and TeO_2 for the selected acoustic direction disregarding losses introduced by the glue layer. From the value recorded the effect of the glue layer may be estimated. From the second transducer, the theoretical diffraction

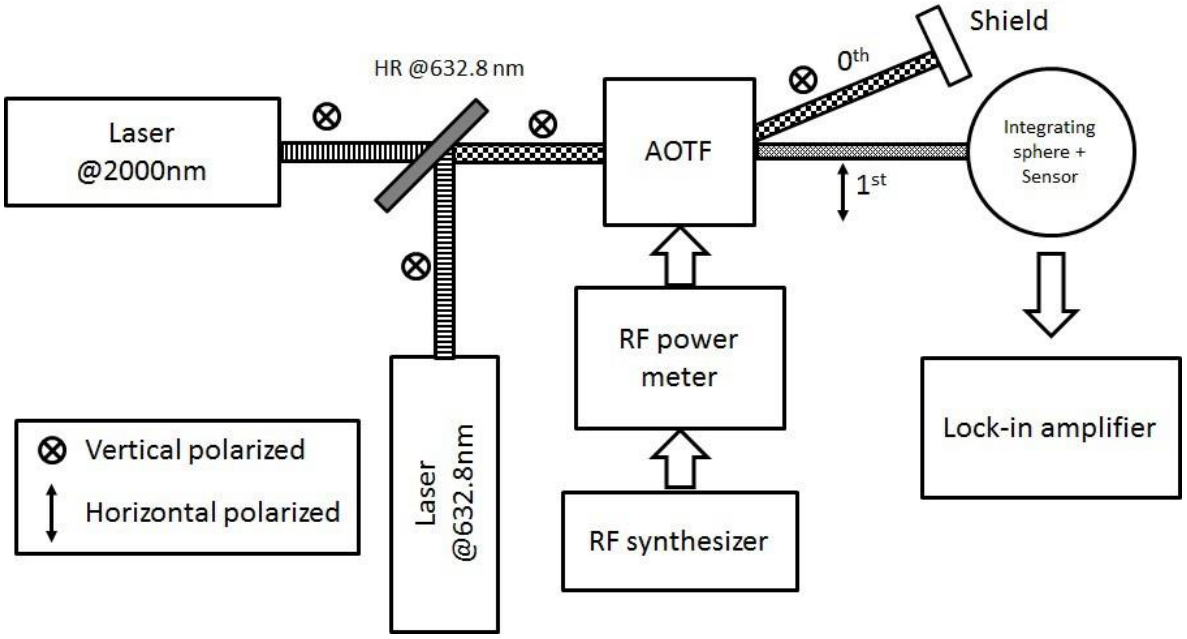

Figure 6.24: Laser line test setup to measure diffraction efficiency versus RF power.

efficiency versus RF power is estimated from Eq.4.9 with an allowance of 14% in practice due to acoustic impedance mismatch. The exact value of coupling coefficient is obtained from the measurement taken from the first transducer. Therefore the missing photoelastic constant (p_{44}) may be estimated using Eq.4.9 - Eq.8.10.

The method described would allow the determination of the missing photoelastic constant of Calomel. The solution proposed allows the removal of the uncertainty due to the transmission of the glue layer, which is affected by the thickness and its physical properties. Two experiments are planned to determine the accuracy of this method. The first one will be used to measure the actual coupling coefficient between the Hg_2Cl_2 cell and the substrate, and the second one will be to measure the values the missing photoelastic constant in Hg_2Cl_2. The method described cancels out the unknown glue coupling coefficient. It is envisaged that this method can be used as a general method to estimate the value of the photoelastic tensor components of new and difficult materials where one has to rely on an acoustic connection of unknown transmissivity between the test material and the acoustic transducer, and where transducer bonding techniques commonly used in the acousto-optics industry cannot be applied because of mechanical and/or chemical incompatibility.

6.22 Conclusion

A feasibility study of AOTFs using Calomel single crystals to extend the tunable range up to 10 μm was undertaken. There are several challenges to overcome in order to realise an efficient device which can be used in the system under development in the MINERVA project. From the theoretical point of view the value of M_2 in case of the slow shear interaction is lower than that of Tellurium Dioxide, and the limited birefringence, combined with long wavelength create design problems.

The limited birefringence leads to a low RF frequency reducing the wavelength range covered by a single device. A solution may be to increase θ_i at the expense of the M_2 increasing the RF power versus diffraction efficiency.

The limitation for wavelength above 3 μm has been described in the previous chapter, extending the wavelength range up to 10 μm leads to impractically high RF power required to achieve a suitable diffraction efficiency, leading to strong thermal gradients. These limitations, as explained in the chapter, are mainly due to the chemical and physical properties of Calomel single crystal, since a conventional efficient bonding technique cannot be used. A solution has been devised where the conventional bonding technique and subsequent transducer reduction to the correct thickness is realised on a buffer substrate of choice, where this process is well known. The material of choice for the substrate has been found to be Tellurium Dioxide, since it belongs to the same crystal class maintaining the continuity of the eigenvector between the two media, in addition the acoustic impedance between the two materials maximizing the acoustic transmission. The TeO_2 substrate with the ultrasonic transducer is bonded to the AO crystal by means of organic glue. The preliminary results shows agreement with the theoretical model developed, but the bonding technique is still in an early stage and the results obtained are not repeatable.

The first AOTF prototype configured in parallel tangent matching condition shows good agreement for the tuning relation but the RF power versus diffraction efficiency was low due mainly to the presence of the glue layer. The non-collinear AOTF was not tested before the end of the research period due to a commercial pressure.

In conclusion also if all the engineering challenge would be solved, the performance of the AOTF are limited by the AO properties of the Calomel Crystal. If the bonding technique is improved a resonant configuration may help to reduce the RF power consumption, but the longer wavelength is about $8\mu m$, above requires the use of a different ultrasonic transducer. The Calomel single crystal is an Acousto-Optic material with good performance using longitudinal wave [2]-[38]. In AO devices exploiting the slow shear interaction, the performance in Calomel is limited by the low value of M_2, which in turn appears to be limited by an ”unfortunate” value of p44 coefficient.

Chapter 7

Dual Polarization imaging AOTF

Imaging AOTFs are designed to satisfy the parallel tangent matching condition, where the AO interaction is optimized for one input polarization. In a conventional imaging AOTF, if the input is un-polarized broad band light then two orders are obtained as output. The source of the two orders is simply due to the phase matching condition satisfied for both polarization states, conventionally the two orders are defined as $+1^{st}$ for the vertical polarization input and -1^{st} for the horizontal input defined by the acoustic direction. The spectral composition of the centre wavelength for a given frequency is different for each diffracted order, which can be estimated theoretically by solving the AO interaction for a given θ_i for each input polarization. The k-space diagram for this particular case is shown in 7.1.

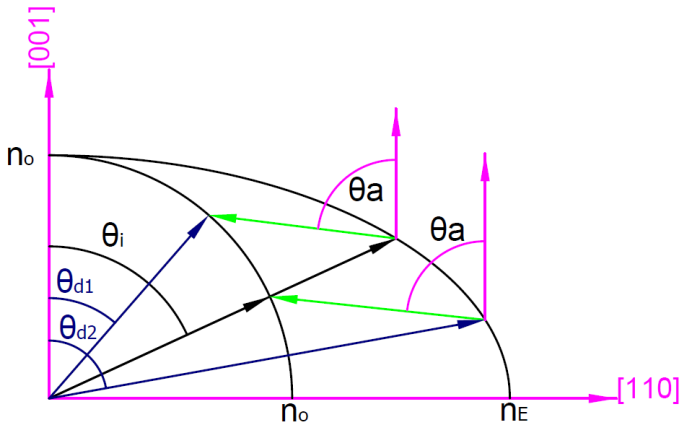

Figure 7.1: K-space diagram for the dual polarization solution.

It is well-known that the parallel tangent matching condition is simultaneously satisfied for both polarization for θ_a = -71.123° and consequently θ_i = 55.574° as shown in Fig.7.2.

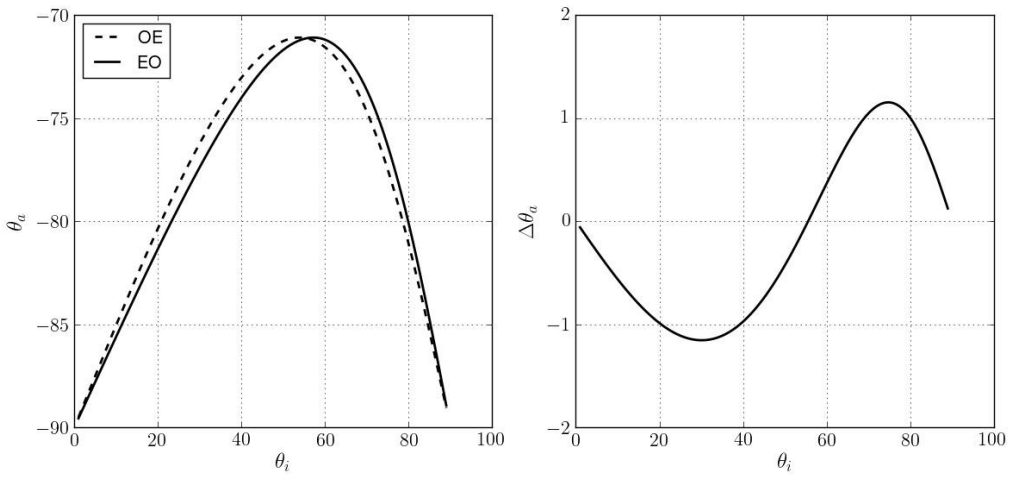

Figure 7.2: Relation between θ_a and θ_i for the two type of AO interaction under the parallel tangent matching conditions (right) and difference the between the two types of AO interactions versus θ_i (left)

This AO interaction has an inherently high frequency in the visible range, hence the acoustic attenuation restricts the aperture for practical devices. This limitation can be overcome by selecting a wavelength range above about 2 μm. The acoustic walk-off and the angle of the input face leads to a cell of large dimensions, where most of the material is not used (Fig.7.3), leading to a device that is wasteful of material and inherently expensive from the manufacturing and material point of view.

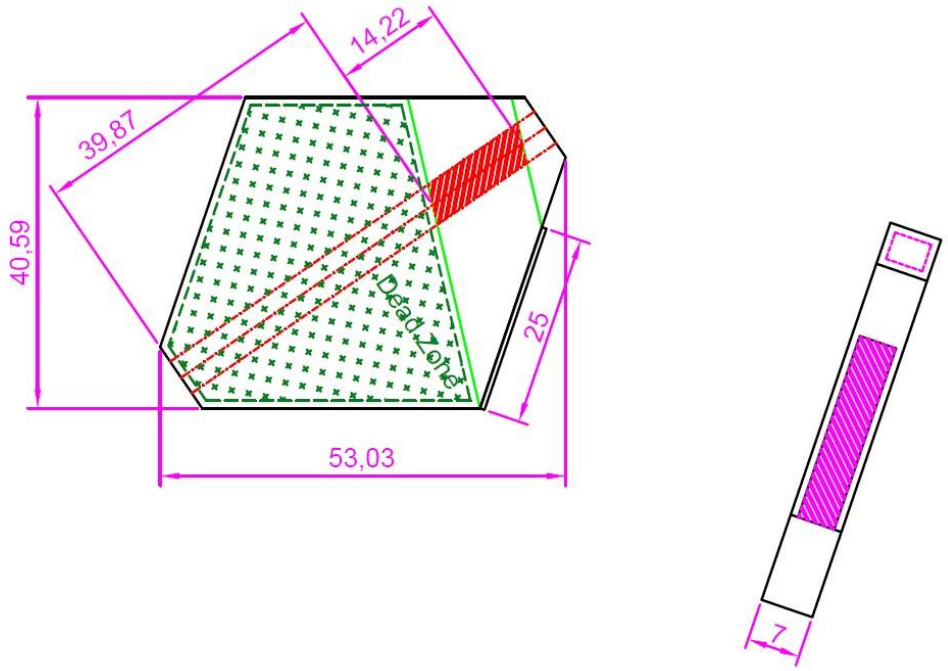

Figure 7.3: Proposed dual polarization AOTF design, where a "dead-zone" is marked and the actual interaction length is shown in red.

This particular configuration has several drawbacks in the UV - visible, for wavelength beyond 2 μm the centre frequency is typically below 70 MHz, therefore the acoustic attenuation does not dominate the diffraction efficiency across the aperture. The impracticality to build such device is the inefficient use of the crystal volume. A solution is therefore proposed to increase the interaction length by configuring the cell in order to reflect the sound in a controlled direction to increase the interaction length. This is obtained by orienting faces "E" and "F" parallel to the Z faces, the reflected acoustic wave direction and applying Snell's law is mirrored. The phase matching condition for the reflected wave is not satisfied and therefore no diffracted order is obtained, on the second reflection again the acoustic direction is directed again along θ_{a1} and the phase matching condition takes again place.

7.1 Theoretical Performance

The theoretical tuning curve of the dual polarization AOTF design is shown in Fig.7.4 for a wavelength range between 2 μm and 4.5 μm, θ_i is fixed, consequently due to the dispersion of the material the acoustic direction changes. The acoustic direction for both polarizations is not exactly the same for the given θ_i but the maximum error introduced is equal to 21.6 arc-second, which is below typical manufacturing tolerances (5 minutes).

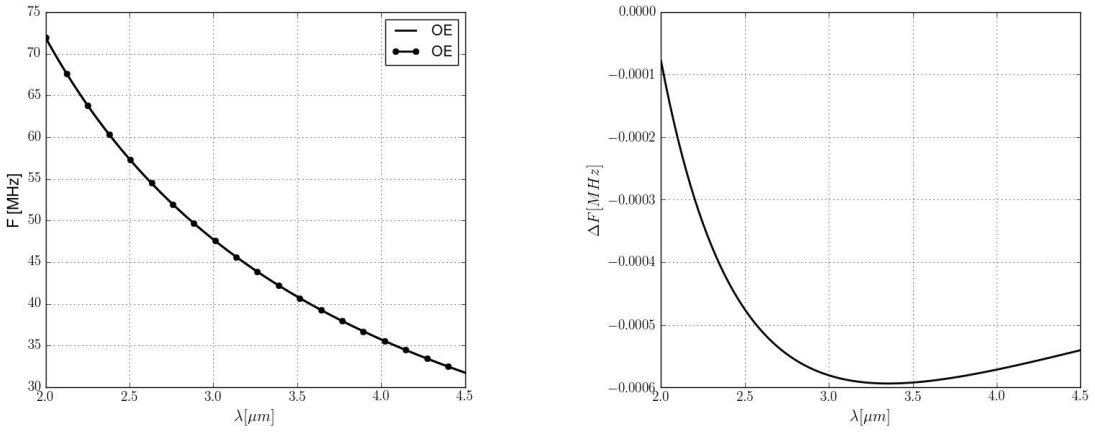

Figure 7.4: Tuning relation (left) and difference in frequency to between the two type of phase matching condition(right).

The RF power for peak diffraction efficiency is shown in Fig.7.5 assuming a transducer length equal to 25.0 mm and height of 5.0 mm, which gives an interaction length of 14.22 mm.

If a practical limit to the maximum RF power is limited to 5 W, as is the case of a

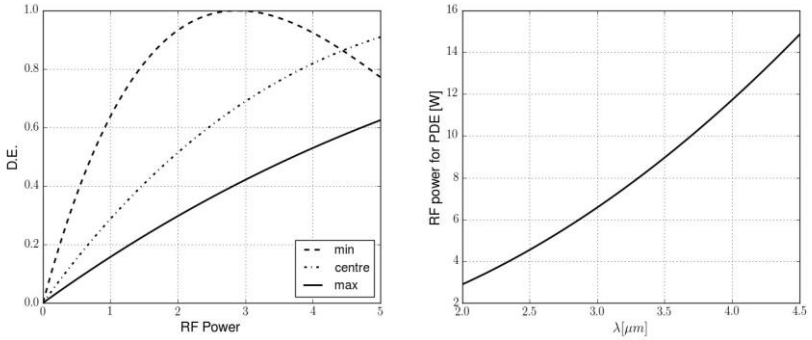

Figure 7.5: Diffraction efficiency of the dual polarization AOTF (left) and RF power to achieve peak diffraction efficiency (right).

conventional AOTF when the RF power for peak diffraction efficiency (D.E.) is above the limit. Hence the maximum D.E. for each polarization is below 65%. From Eq.8.11 it is clear that the only solution to reduce the RF power consumption is to increase the interaction length, but this is obtained at the expenses of larger AO cell, where the material limit dimension is easily reached without reaching any actual benefit on the RF power reduction.

The solution proposed in order to increase the interaction length is to reflect the acoustic wave in controlled direction inside the "dead zone" where the AO interaction can take place again. Increasing the interaction length depends on the dimension of the cell and on the acoustic attenuation. Practically the interaction length has been increased by a factor of two in order to limit the dimension of the AO cell, but theoretically it is possible to increase it up to four. The dimension of the cell becomes impractical for five times or more and the acoustic attenuation dominates the performance especially in the short wavelength region.

7.2 Dual polarization AOTF prototypes

The increase of the interaction length is obtained by configuring the faces "G" and "H" parallel to the [110] direction, hence the acoustic wave has an incident angle equal to θ_i is reflected along θ_r with same acoustic walk-off direction. The AO interaction does not take place for $\theta_a = \theta_r$, because the phase matching condition is not satisfied.

The reflected acoustic wave propagates along the same direction of θ_a, where the phase matching condition is satisfied, if the phase between the two AO region is correct then superimposition effect can applied and the interaction length is twice as large. This will produce efficient AO interaction with narrow bandwidth and lower RF power for peak diffraction efficiency. The predicted performance of the device shown in Fig.7.6 is shown in Fig.7.5 with dimension reduced by 50% compared to the cell used in a

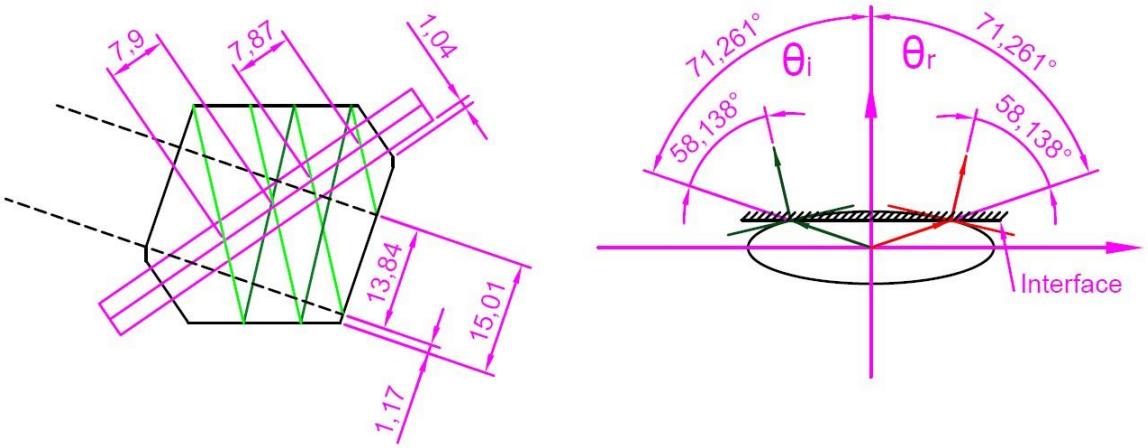

Figure 7.6: Dual polarization AOTF cell, with face C as transducer face, faces A and B input and output faces, and face G and H are the face reflecting the acoustic wave (left) and acoustic reflection diagram (right).

conventional AOTF.

In order to increase the number of acoustic columns in the AOTF, a second prototype was designed and built modifying the previous cell. In this case the faces "G" and "H" are not parallel to the < 110 > direction, but they are oriented 5,223° from it.

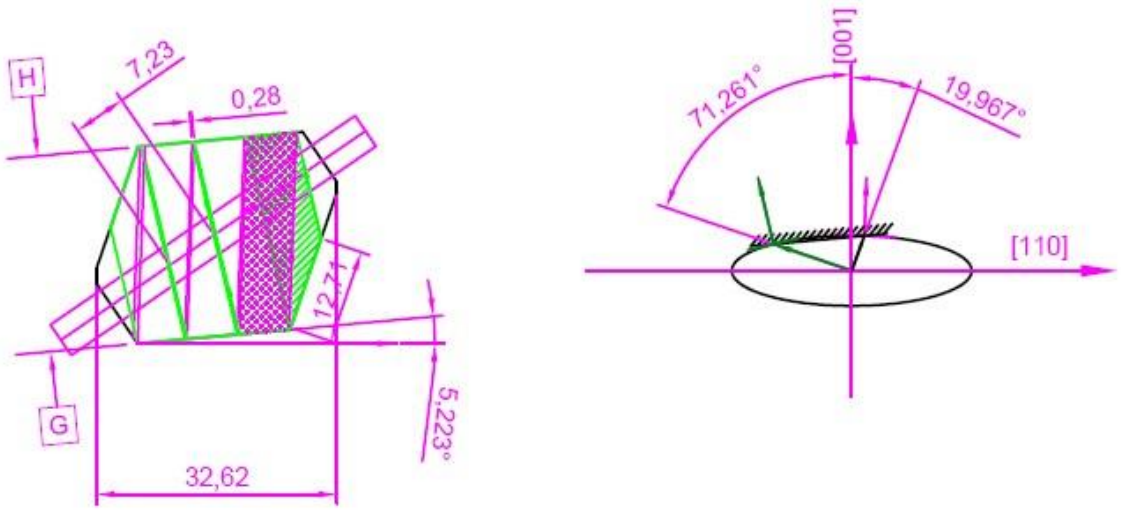

Figure 7.7: Dual polarization AOTF with angled faces to increase the numbers of acoustic reflection (right) and diagram of the acoustic reflection (left)

In this case the acoustic wave for the AO interaction and the reflected are spatially overlapped, but the phase velocity changes due to the different propagation directions and only the correct acoustic direction satisfy the phase matching condition.

The internal and external separation angles are determined theoretically by dedicated routine applying the Snell's law for each polarization and order and resume in Tab.7.1.

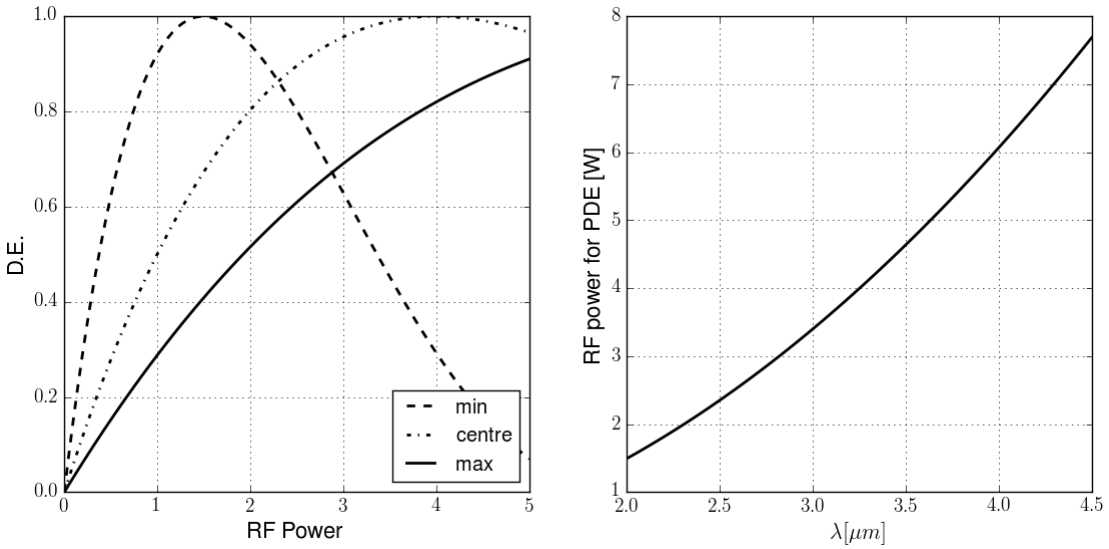

Figure 7.8: Predicted Diffraction Efficiency (D.E.) of the device shown in Fig.7.6 versus wavelength (left). RF power to achieve Peak Diffraction Efficency (PDE) versus wavelength (right).

Type	θ_{sep}	$\lambda = 2.5\ \mu$m	$\lambda = 4.5\ \mu$m
EO	internal	-3.363053°	-3.378121°
EO	external	-7.343862°	-7.397101°
OE	internal	3.230706°	3.216921°
OE	external	7.397235°	7.313907°

Table 7.1: Internal and external angle for both AO interaction in the dual polarization AOTF.

The maximum external deviation for the extraordinary polarization is equal to 0.0833° (~ 5') and for the ordinary polarization is equal to 0.0532° (~ 3'), and the full separation is obtained for 5 mm diameter input at 43.39 mm. The reflected acoustic wave, marked with crosses in Fig.7.7, is propagating close to the optical axis, hence the acoustic velocity is close to its maximum. M_2 is close to a minimum in combination with the input direction and the RF frequency applied. There is no efficient acousto-optic interaction in the wavelength range under consideration, therefore no spurious order are generated at the output.

The Pointing stability is applied to the non-diffracted order in this case and the two diffracted orders show beam steering, which can be compensated with additional external prisms. In the wavelength range under consideration the dispersion of the material

is relatively low, but it is still noticeable.

7.3 Dual polarization AOTF matching network

The AOTF cell was mounted on the AOTF prototype mount. The matching network to cover tuning range of interest is shown in Fig.7.9(a) and 7.9(c), and the VSWR of the device is shown Fig.7.9(b).

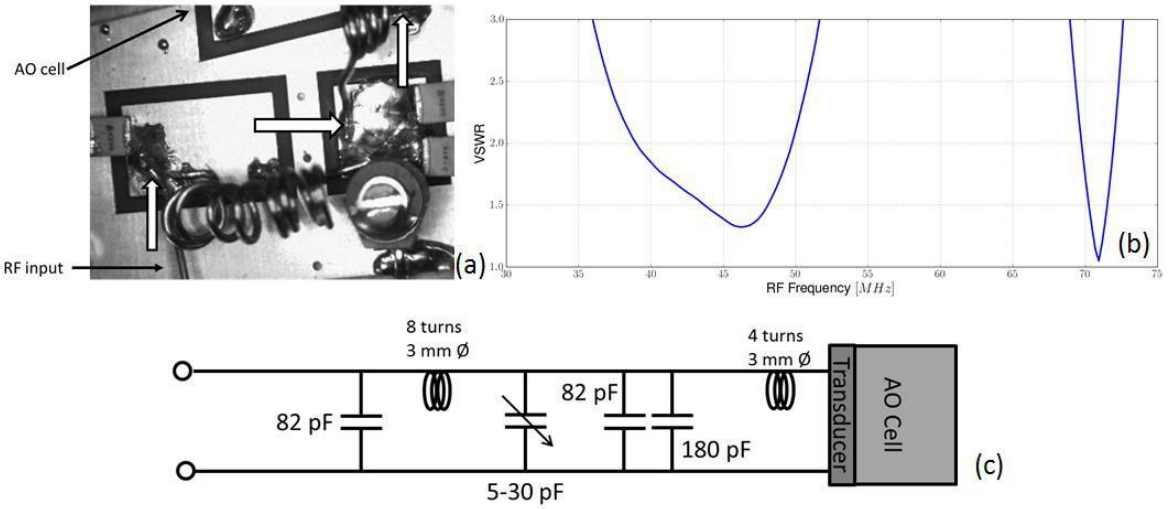

Figure 7.9: RF matching network for the dual polarization AOTF: photograph (a), measured VSWR (b), RF schematic (c).

The AO devices was matched to have a minimum VSWR at the two RF frequencies, where the phase matching condition is satisfied for $\lambda = 2\ \mu m$ and $\lambda = 3.390\ \mu m$, to coincide with the two available laser line.

7.3.1 Experimental results

The two dual polarization AOTFs described in the previous section have been tested using the laser line test with a laser source 3390 nm and RIG described in Appendix G.1. The laser source was rotated by 45° and a polariser used to select the vertical or horizontal polarization. The diffraction efficiency was measured equal to 20% for an RF power of 1.2 Watt for both polarization and the passband of the device is shown if Fig.7.10.

The passband shows a similar behaviour to the resonant AOTF, this is probably due to the phase difference between the different acoustic columns crossed by the light. In order to increase the diffraction efficiency, it would be required to have a phase locking

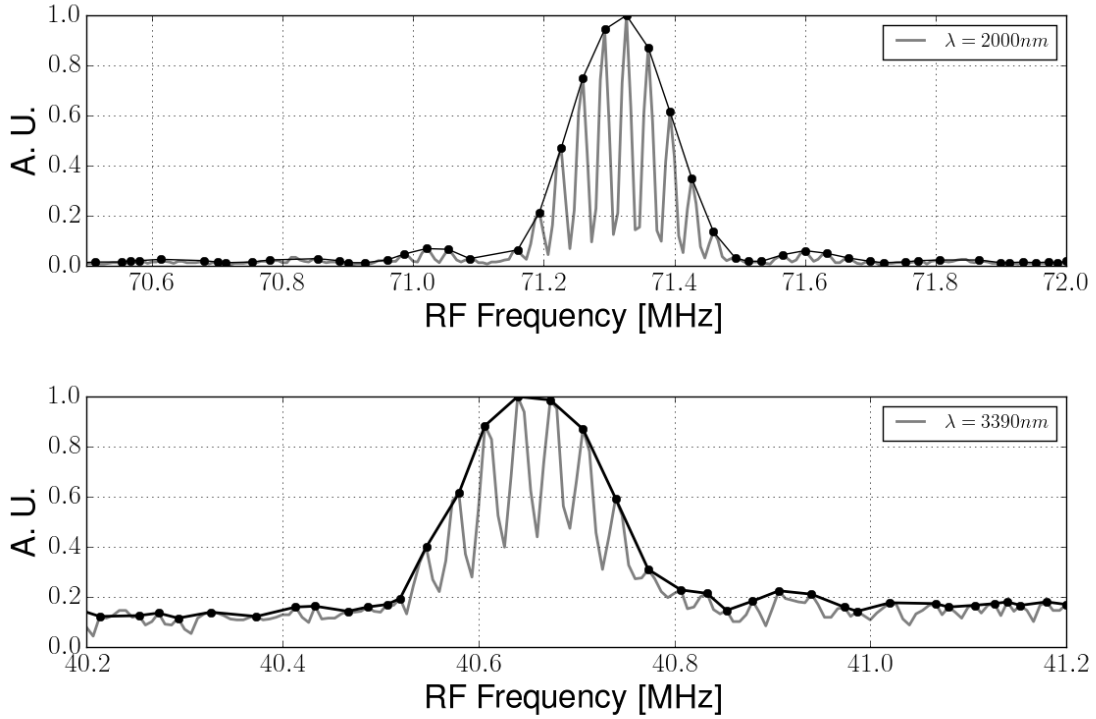

Figure 7.10: Experimental passband measurement obtained by the laser line test at two different wavelengths (grey line) and envelopes(dark line)

loop in order to control the phase between the different acoustic reflection in addition to a temperature tuning in order to maintain the device in "phase". This solution requires a special RF driver, which was out of the scope of the research activity.
Similar results were obtained with the device shown in Fig.7.7 with a diffraction efficiency of 12% at 1 Watt.
The tuning curve was planned to be recorded using the supercontinuum source developed by NKT inside the MINERVA project, with tuning range up to 5 μm, but due to testing schedule of other experiment was not possible the record of the full tuning curve, therefore only the tuning curve centred in $\lambda = 2\ \mu m$ is shown (Fig.7.11).
Fig.7.11 shows the centre wavelength for a given frequency is the same for both polarizations, confirming the prediction of the mathematical model and design routine developed, due to the limited resolution of the Optical spectrum analyser it is not possible to see the features visible by the laser line test with greater resolution.

7.4 Applications for the dual polarization AOTF

The dual polarization AOTF has been studied for a specific application, where a non coherent source is to be filtered by an AOTF in the infrared region. AOTFs are

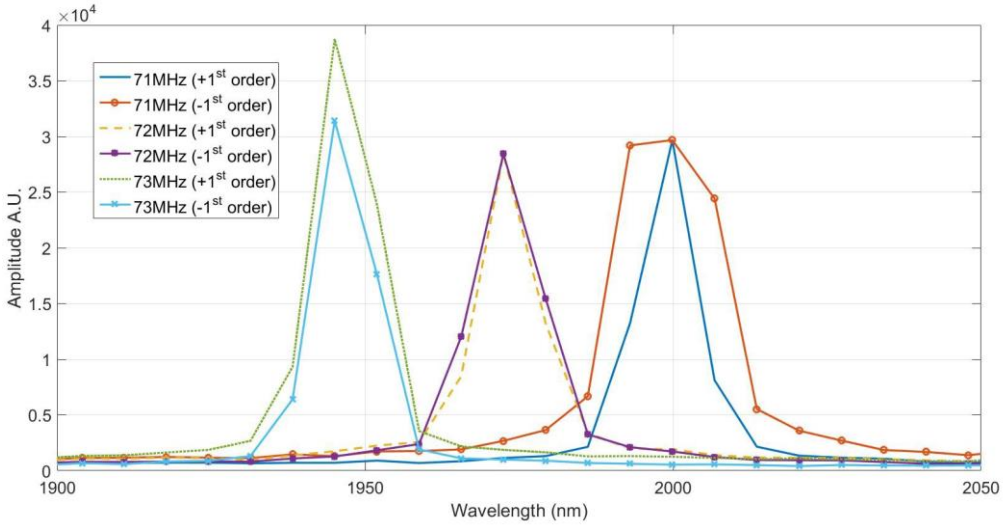

Figure 7.11: Optical spectrum recorded by an OSA from OceanOptics of the +1st and -1st order of the device in Fig.7.7

normally designed to be optimized to only one polarization, therefore in the case of non-polarized light, the diffraction efficiency is typically 47 %, and half of the optical power is not used. In order to use both polarization is possible to define a θ_a where the AO interaction for both polarization takes places for a given wavelength at the same RF frequency, but in this case the parallel tangent matching condition cannot be applied. In order to apply a large aperture AOTF the parallel tangent matching condition can be applied for both polarization only for a specific angle as shown in Fig.7.2. This case the efficiency is double and the passband for both orders will be centred to the same wavelength, but with different polarization, therefore this type of devices could be used for several application such as remote sensing, polarimetry imaging and optical spectrum analysers for the IR region.

7.4.1 The optical spectrum analyser in the wavelength range: 2 μm - 4.5 μm.

Optical spectrum analysers are conventionally used on several applications where the spectrograph of a target is relevant. Different suppliers already exist in the market for example Ocean Optics and Avantes, which produce spectrometer with passive components for wavelengths up to 2.5 μm. For a wavelength range above 2.5 μm other solutions are typically applied such as FTIR spectrometer with moving parts inside. These operate works up to 20 μm and are typicallysupplied by Thorlabs, Bristol Instrument and other suppliers. AO based spectrometer have been reported in the literature implemented with Quasi-Collinear AOTFs [42], which require diffraction limited light,

and full-collinear AOTF, also with a narrow field of view, and designed to work up to 3 μm. As an internal project of Gooch&Housego proposed by C. Pannell, where the author identified the potential for an AO based spectrometers aimed at the segment of the market shown in Fig.7.12

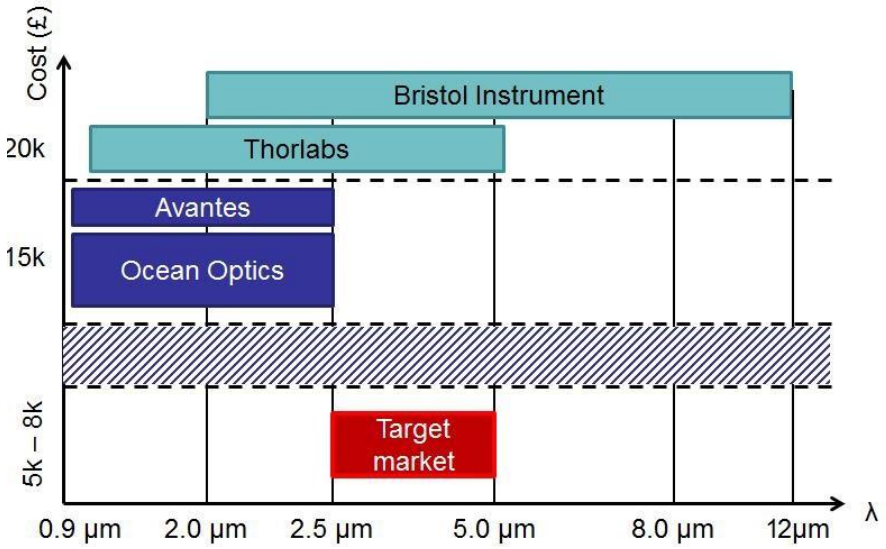

Figure 7.12: Market segmentation of Optical Spectrum Analyser.

The aim of the solutions developed is to create an OSA which could be benefit from the dual polarization configuration in the infrared region at a competitive price, but also with a additional features, which conventional OSA cannot offer. The OSAs currently on the market use fibre input for the passive components in the system and an additional port for a free space input in case of FTIR with collimated light with a maximum diameter of 5 mm. The AO solution could also have both inputs. Different configurations have been proposed depending on the final customer requirements.

The OSA structure shown in Fig.7.13 have two possible configurations. The first configuration is using a single concave mirror to focus the -1st order to a IR sensor, and +1st order exit, hence the spectrum of the source used for the experiment can be monitored in real time because the diffraction efficiency and the spectral component of both diffracted order is the same. The second configuration is implemented by introducing an additional concave mirror and IR sensor, in this case one sensor will record the vertical polarization of the input and the other one will record the horizontal polarization, the information could be used in polarimetric measurement.
For the case of an imaging application the mirrors and the IR sensors may be substituted by CCD cameras (single or dual), and additional optics, capable of giving in addition polarimetric information.
The performance of the system has been theoretically determined using a random

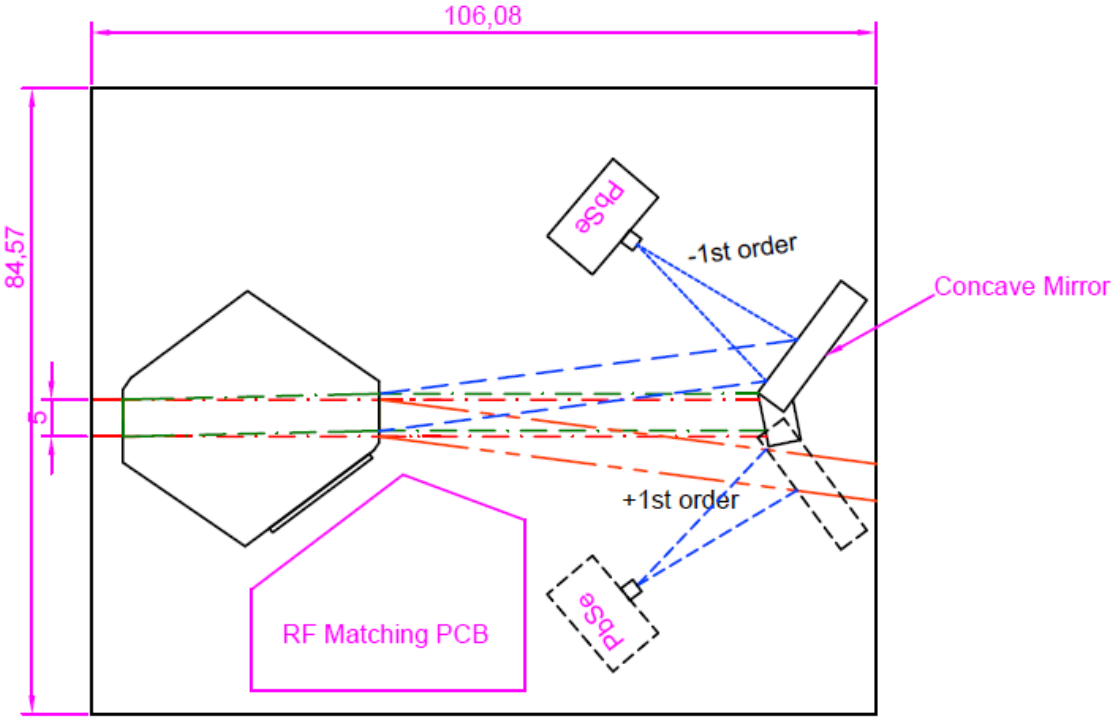

Figure 7.13: Outline of the system

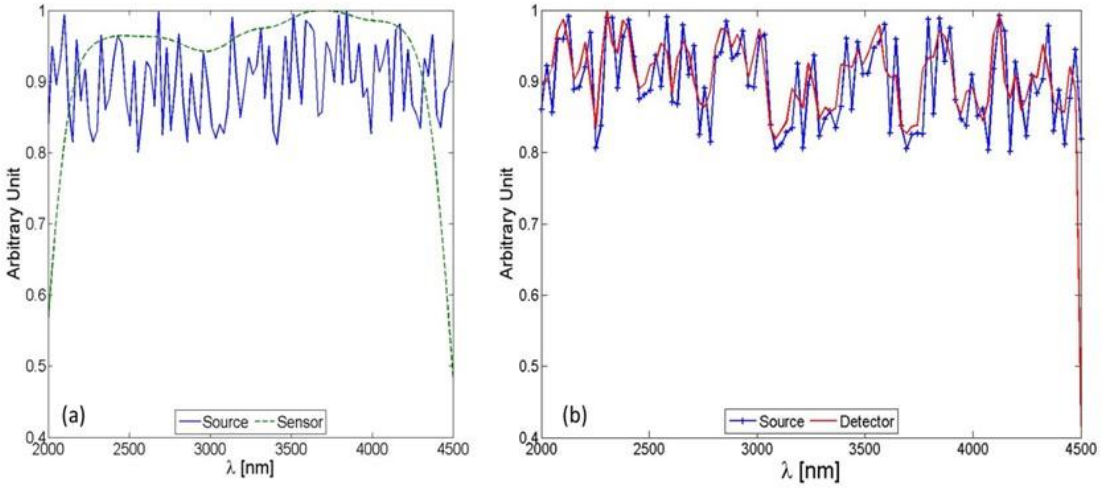

Figure 7.14: Simulated response of a dual polarization AOTF (dotted line) compared to a source with random fluctuation (continuous line) for a resolution of 10 nm (left)and 2 nm (right).

variable source and a tungsten lamp (HEP3965) supplied by Thorlabs. Two different passbands was considered for the case of a random variable source, to determine the possibility to record the variation of the spectrum intensity. In the case of a low resolution AOTF the actual intensity recorded by the sensor is flat as expected and therefore in specific application a narrow AOTF will be required, eventually in quasi-collinear configuration.

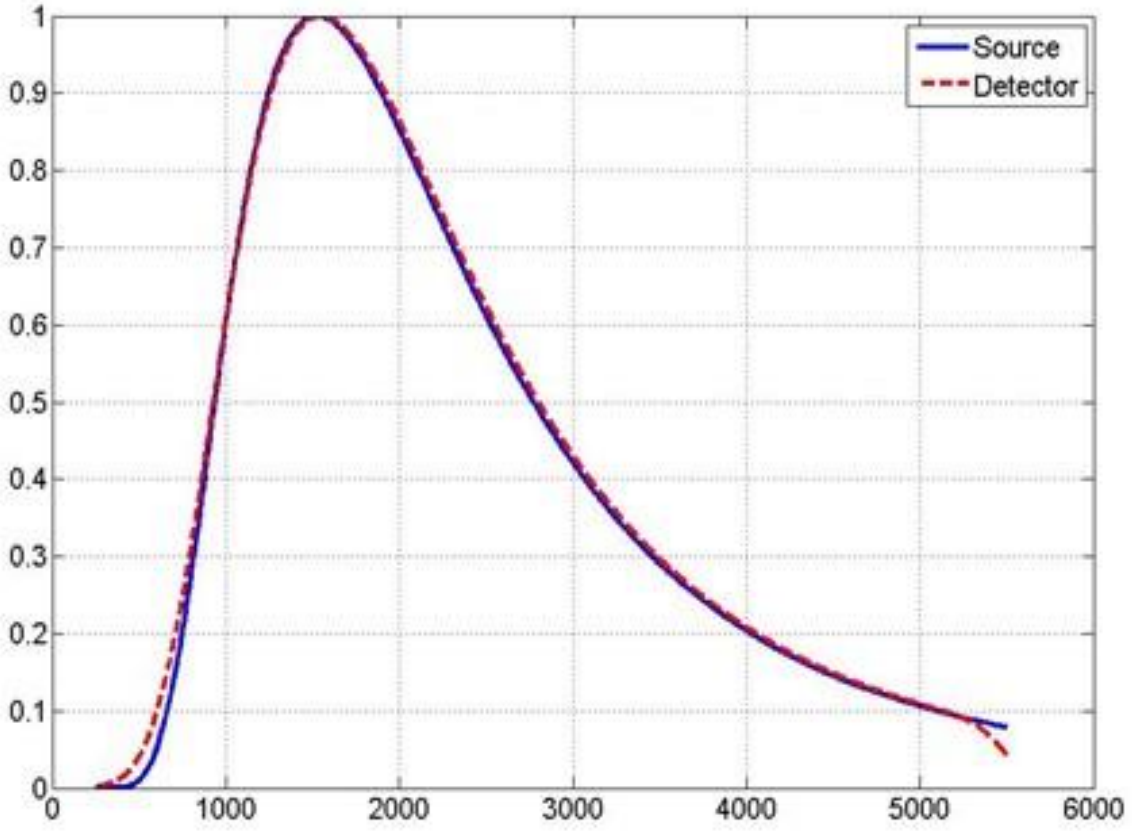

Figure 7.15: Simulation results of the signal from the detector versus source, which is HEP3695 from Thorlabs

The total cost of the additional components to build the first prototype has been estimated using off the shelf components and shown in Tab.7.2. The total cost of the components for the solution with single detector is ~ £ 700, without including the RF driver and the AOTF and approximately equal to £1000 for the dual sensors solution. This compares to a selling price of approximately £ 15000 for existing techonlogies.

7.5 Conclusions

The development of a dual polarization AOTF has been reported in this chapter, the device was developed in order to be used to build an Optical Spectrum Analyser (OSA)

Part number	Unit Cost	Quantity	Cost
MPD269-M01	£176	1	£176
SM2MP	£22	1	£22
KCB2/M	£117	1	£117
PDA20H-EC	£322	1	£322
LDS1212	£42	1	£42
PDA-C-72	£15	1	£15

Table 7.2: Additional components required to build the first prototype of the OSA.

in the wavelength range between 2.5 μm and 4.5 μm and targeted to sell at less than £10000. The limitation on the performance of the device is related to the dual polarization at the parallel tangent matching conditions, which is achieved at $\theta_i = 55.574^\circ$ (θ_a = -71.123°). The acoustic walk-off will dictate the size of the device leading to a "dead-zone" of unused material. A solution has been proposed to overcome this limitation and reduce the device size by half (and consequently reducing the cost), by reflecting the acoustic wave in a controlled direction in order to increase the interaction length and improve the diffraction efficiency versus RF power requirement.

Preliminary results show that the tuning relation for both polarizations, but the efficiency was less than predicted. One reason for that is the phase difference between the two acoustic "columns". If the phase is different then two columns act as two separate devices in series reconverting back to the zero order part of the diffracted orders. Experimentally it was seen that the laser line test shows different peaks around the centre frequency similar to a resonant device, confirming the phase issue.

In order to at least double the interaction length a possible solution using a dual transducer is likely to be a more effective approach, which will allow control of the phase between the two acoustic columns separately. An experiment with a dual channel AOTF with two transducers, where one was rematched to have an overlap with the first transducer, confirming if the phase between the two transducers is zero, then the diffraction efficiency is increased as expected. In literature a similar device was reported by Voloshinov and Gupta in [43].

Another possibility is to use a solution where the phase matching is achieved for both polarizations simultaneously, the solution of this interaction is between the two different solutions for the parallel tangent matching condition as shown in Fig.(7.2).

The OSA system was proposed to show how the AOTF might be exploited in different configurations (Fig.7.13). The device could use a single point detector, and thanks to the dual polarization AOTF, by removing one of the sensors it is possible to use the output for a different experiment and to monitor with another sensor the intensity of the spectral components in real time.

The possibility to build an OSA, which is modular, and with a competitive price compared to the equivalent on the market is of particular interest, for many potential applications.

Chapter 8

Effects of the acoustic attenuation in large aperture AOTF for wavelengths in the visible

8.1 Introduction

In the previous chapters, It was investigated several AOTFs to cover different wavelength ranges from UV to Mid-IR up to 10 μm. The acoustic attenuation typically does not affect the performance of devices working with low frequencies, but in some particular cases such as the device studied in this chapter, the performance are dictated by the acoustic attenuation.

An efficient birefringent AO interaction is obtained when the phase matching condition between the acoustic wave and the incoming electromagnetic radiation is satisfied:

$$\mathbf{k}_d = \mathbf{k}_i \pm \mathbf{K}_a \tag{8.1}$$

where

$$k_i = \frac{2\pi n_i(\lambda)}{\lambda}, \qquad k_d = \frac{2\pi n_d(\lambda)}{\lambda}, \qquad K_a = \frac{2\pi V}{f} \tag{8.2}$$

with V as the acoustic velocity in the AO material, λ as the diffracted wavelength, f as the RF frequency applied, n_i and n_d are the refractive indexes, where the values is determined by the AO interaction type [6], as described in the previous chapter. This is commonly defined as **EO**, if the incident polarization is an extraordinary ray and

the diffracted order consequently is an ordinary ray, vice versa **OE** identifies the AO interaction from ordinary to extraordinary polarization [44].

An infinite number of possible configurations exists where the phase matching condition is satisfied, therefore additional constrains are typically introduced depending on the application [29]. Imaging AOTF exploits the non-collinear interaction satisfying the parallel tangent matching condition and is characterized by a large acceptance angle, which is required when non-coherent light is used to illuminate an arbitrary target. The choice of the AO material depends on the wavelength range specified by the application; in the range between 380 nm and 4.5 μm the material of choice is Tellurium Dioxide (TeO_2) due its acoustic-optic properties and its availability in boules of large dimensions with good optical quality. However this material is characterized by strong acoustic attenuation which, in the case of large aperture devices, limits the achievable performance for wavelength below about 600 nm due to the high driven frequency. A solution conventionally implemented is to calibrate the AOTF response against a white screen at expenses of the dynamic range of the camera.

This chapter examines an AOTF configured to operate with input vertical polarization corresponding to an ordinary ray. The 1^{st} order is polarized horizontally as an extraordinary ray, therefore the refractive index value depends also on θ_d and is defined as:

$$n_d(\lambda,\ \theta_d) = \sqrt{\frac{n_o(\lambda)n_E(\lambda)}{n_o^2(\lambda)\sin^2\theta_d + n_E^2(\lambda)\cos^2\theta_d}} \tag{8.3}$$

The acousto-optic interaction takes place known as t[110]-Z[001] plane, and the phase velocity is given by Eq.3.30, which is reported below:

$$V(\theta_a) = \sqrt{V_t^2\sin^2\theta_a + V_z^2\cos^2\theta_a} \tag{8.4}$$

with $V_t = 616$ m/s and $V_Z = 2104$ m/s, and θ_a is estimated from the optical axis. Eq.8.4 is obtained by the eigenvalues of the Christoffel's equation solution introducing the elastic stiffness constant of the material in the plane where the AO interaction takes place, where the acoustic mode is determined by the eigenvectors direction. Therefore the phase velocity along the main axes is defined as

$$V_z = \sqrt{\frac{c_{44}}{\rho}} \tag{8.5}$$

$$V_t = \sqrt{\frac{c_{11} - c_{12}}{2\rho}} \tag{8.6}$$

where c_{ij} are the elastic stiffness constants of the material, and ρ is the density (equal to 5990 Kg/m^3). The acoustic attenuation is not introduced here, because the previous

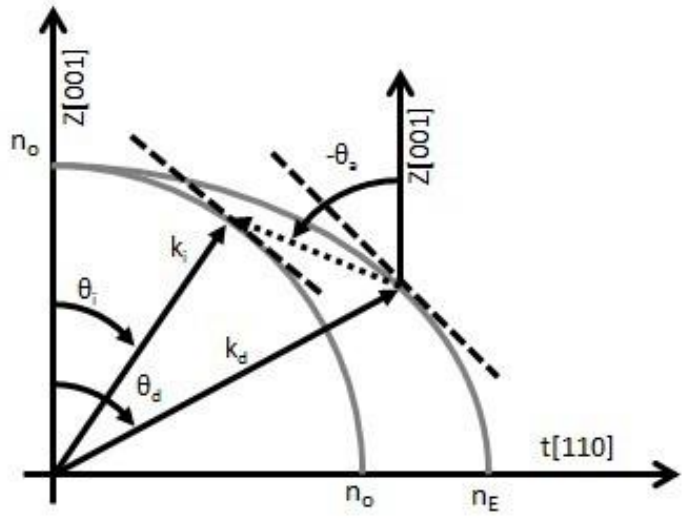

Figure 8.1: K-space diagram of the AO interaction OE under the parallel tangent matching condition. The tangent of the refractive index surfaces is shown as dotted lines. The acoustic vector (K_a) is shown as fine dotted line.

equations are used to determine the AO interaction configuration.

The parallel tangent matching condition is defined by Eq.4.6 [45] and reported below:

$$\tan\theta_d = \frac{n_d^2}{n_i^2}\tan\theta_i$$

where $n_d = n_E$ and $n_i = n_o$ and the angles are defined from the optical axis (Fig.8.1). This condition is satisfied when the tangents to the refractive index surfaces of the diffracted and incident beam are parallel.

Once the incident direction and consequently the diffracted order are defined by Eq.4.6 introducing Eq.8.3, then the acoustic direction is obtained by simple vector calculation with the help of the K-space diagram. When θ_i, θ_d and θ_a are defined then Eq.8.1 is solved for the desired wavelength range and the tuning relation, between frequency and wavelength of the 1^{st} order, is obtained :

$$f = \frac{V}{\lambda}\sqrt{n_i^2 + n_d^2 + 2n_i n_d \cos\theta_{sep}} \qquad (8.7)$$

where $\theta_{sep} = \theta_i - \theta_d$, all angles are all internal.

8.2 Diffraction Efficiency versus RF power

For a given AO interaction configuration, the diffraction efficiency is predicted by the RF power applied and estimated by [6]:

$$\eta = \sin^2 \sqrt{\frac{\pi^2 M_2 L_a}{2\lambda^2 H} P} \tag{8.8}$$

where P is the RF power applied, H is the height of the acoustic field, L_a is the interaction length, λ is the wavelength of the first order, and M_2 is the acousto-optic figure of Merit

$$M_2 = \frac{n_i^3 n_d^3 p_{eff}^2}{\rho V^3} \tag{8.9}$$

with p_{eff} as the effective photoelastic constant, $\rho = 5990$ Kg/m^3, V as the acoustic phase velocity defined by Eq.8.4, n_i and n_d are the refractive index of the 0^{th} and 1^{st} orders. The effective photoelastic constant for the slow shear interaction in the t-Z plane is equal to:

$$p_{eff} = -\frac{p_{11} - p_{12}}{2} \sin\theta_a \cos\theta_d + p_{44} \cos(\theta_a) \sin(\theta_d) \tag{8.10}$$

where the photoelastic constant components are equal to $p_{11} = 0.0074$, $p_{12} = 0.187$, $p_{44} = -0.17$ for a wavelength of 632.8 nm[46].
In the case of an AOTFs with an aperture of 20.0 mm × 20.0 mm and characterized by elevated high frequencies towards the shortest wavelength, the effect of the acoustic attenuation on the diffraction efficiency profile across the active aperture has to be taken to consideration.

8.3 Theoretical study of diffraction efficiency across the active aperture

An AOTF with a wavelength range between 450 nm and 900 nm has been considered to see the effect of the acoustic attenuation on the diffraction efficiency. The RF power for Peak Diffraction Efficiency (PDE) is estimated by Eq.4.10 proposed again here:

$$P_{PDE} = \frac{H\lambda^2}{2L_a M_2} \tag{8.11}$$

For H = 20.0 mm, and L_a = 8.0 mm, the $P_{P\,DE}$ in the wavelength range in consideration is shown in Fig.8.2.

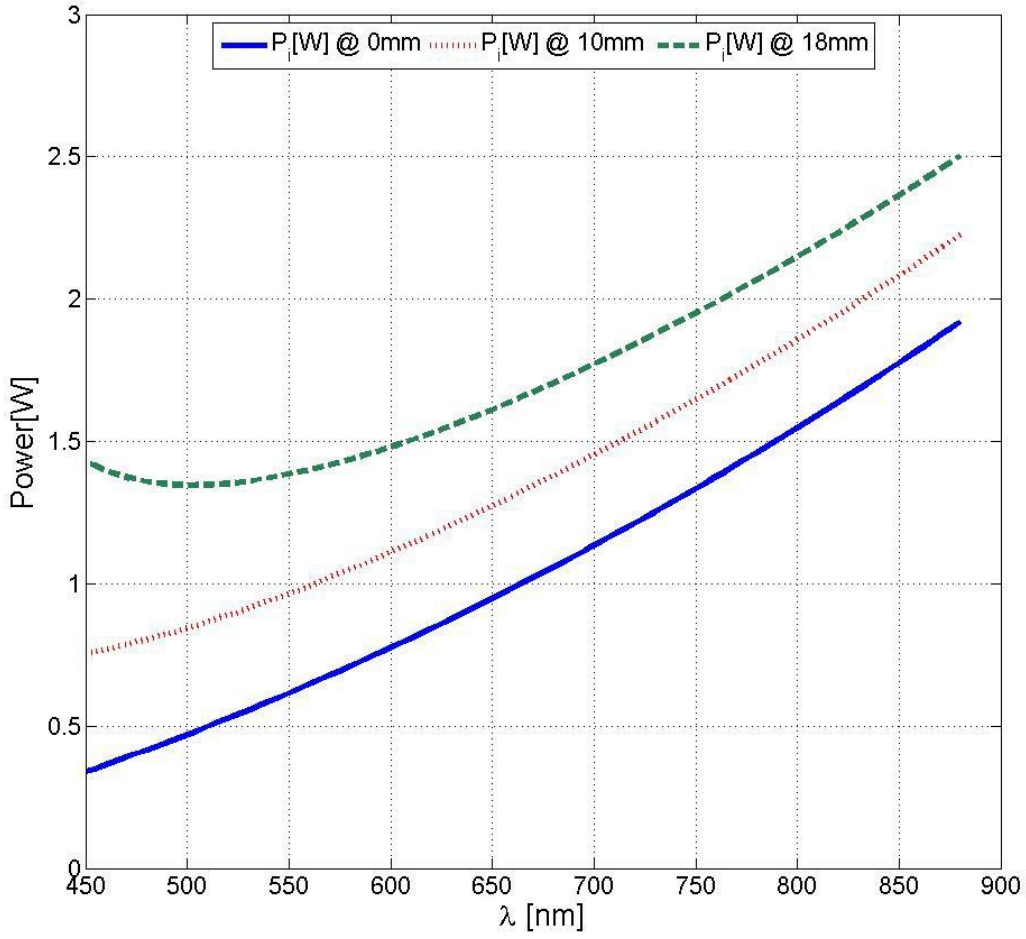

Figure 8.2: RF power for PDE at three different distance from the transducer.

The acoustic power required to achieve peak diffraction efficiency at 450 nm is approximately triple at the far end of the active aperture compared to the region close to the transducer. For an RF power of 1.5 Watt at a distance d = 3 mm from the transducer, the diffraction efficiency estimated by Eq.8.8 is shown in Fig.8.3. The RF power versus diffraction efficiency does not take in account the acoustic attenuation, which is introduced by considering the losses inside the material for a given RF frequency and adding them to the applied RF power.

When the diffraction efficiency is at a minimum in Fig.8.3, the out of band side-lobes increase. The pass-band of the AOTF has been recorded using a laser line test with a laser source at λ = 473 nm in a region close to the transducer at two RF power levels, one to achieve peak diffraction efficiency close to the transducer (0.485 W) and one to

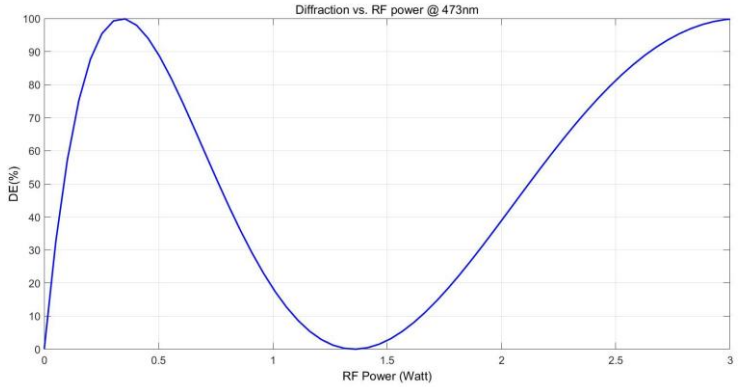

Figure 8.3: Diffraction efficiency versus RF power for $\lambda = 473$ nm.

achieve peak diffraction efficiency close to the opposite side of the active area (1.5 W) (Fig.8.4).

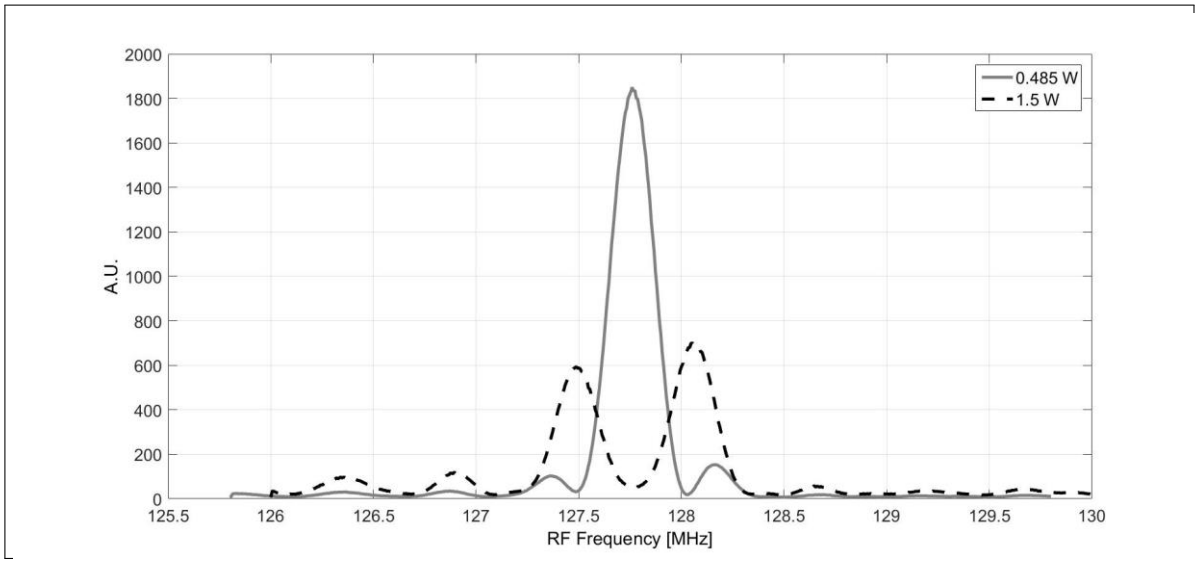

Figure 8.4: Experimental measurement of the pass-band and side-lobes level recorded at a position close to the transducer for two RF power levels.

As expected, the level of the out of band side-lobes drastically increase and this could be a source of errors in spectral response measurements, for example on remote sensing and spectroscopy analysis, so care must be taken to allow for this effect.

In practice the RF power is usually adjusted to achieve peak diffraction efficiency in the centre of the active area, then the change of the diffraction efficiency is not so severe across the aperture but the effects of the acoustic attenuation limits the achievable performance.

8.4 AOTF performance in the wavelength range 450 nm < λ < 850nm

In order to predict the diffraction efficiency across the active aperture, three regions have been identified: one close to the transducer area, one in the centre and one close to the opposite side of the transducer. The RF power has been set to achieve peak diffraction efficiency in the centre of the three regions. For the AOTF being considered, which has an active aperture of 20.0 mm, the peak diffraction efficiency was achieved at three distances: d_1 = 3.3 mm, d_2 = 10.0 mm, d_3 = 16.6 mm. As predicted the acoustic attenuation effects are more noticeable for λ < 600 nm, therefore the diffraction efficiency has been recorded using a laser source at the shorter wavelength.

8.4.1 Experimental set-up and results

The set-up shown in Fig.8.5 has been used to record the diffraction efficiency across the aperture of the AOTF, using a laser source at 473 nm. The AOTF was been mounted on a motorized stage controlled via computer, which allows to scan the active aperture of the device.

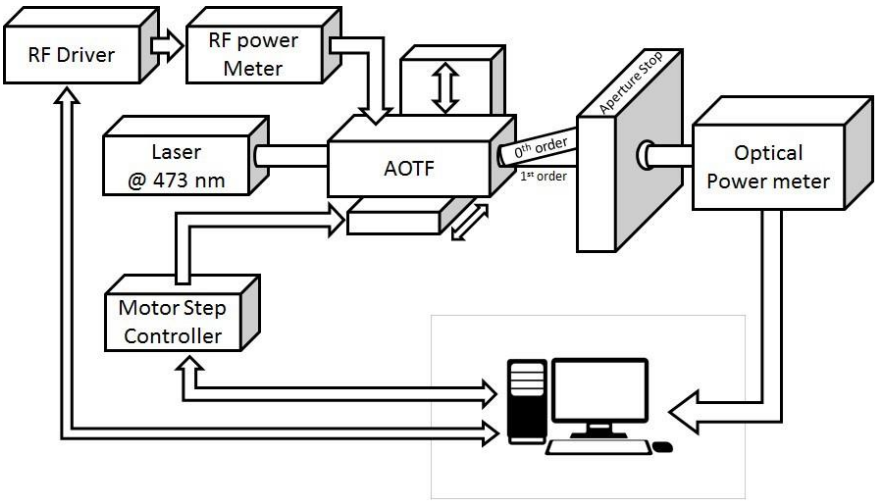

Figure 8.5: Set-up to record the diffraction efficiency across the aperture.

The diffraction efficiency was recorded with an optical power meter placed after an aperture stop, which blocked the 0^{th} order. The laser spot diameter was about 1.0 mm, but additional optics have been added to reduce this to a suitable size.

The RF power was set to achieve PDE close to the transducer and the change of diffraction efficiency across the aperture is shown in Fig.8.6, where a reduction of the efficiency of the first order to 50% is visible after 15 mm. The inhomogeneity along

the Y direction is due to the apodized electrode; the distance, at which the efficiency is recorded, is in the near field of the acoustic wave.
The mathematical model developed considers the acoustic profile in the far field, therefore in order to compare the experimental results with the predicted performance, the diffraction efficiency has been averaged along the X direction for 2 mm < Y < 18 mm, showing a good agreement with the experimental results (Fig.8.7). The diffraction efficiency in Fig.8.7 is normalized and obtained for vertical polarized light, typically the diffraction efficiency is over 95% for each polarization. The theoretical curve is obtained from a Matlab routine developed to estimate the diffraction efficiency for a given wavelength across the aperture.

8.5 Imaging system configuration

In an imaging system, the AOTF is usually placed in front a CCD camera recording the diffracted order, which is compensated in order to reduce the shift, known as "scene-shift" in the plane of diffraction. The intensity profile is not constant so a calibration process is required to take in account the variation of the acoustic intensity (e.g. recording a white background while tuning the AOTF) at the expenses of a

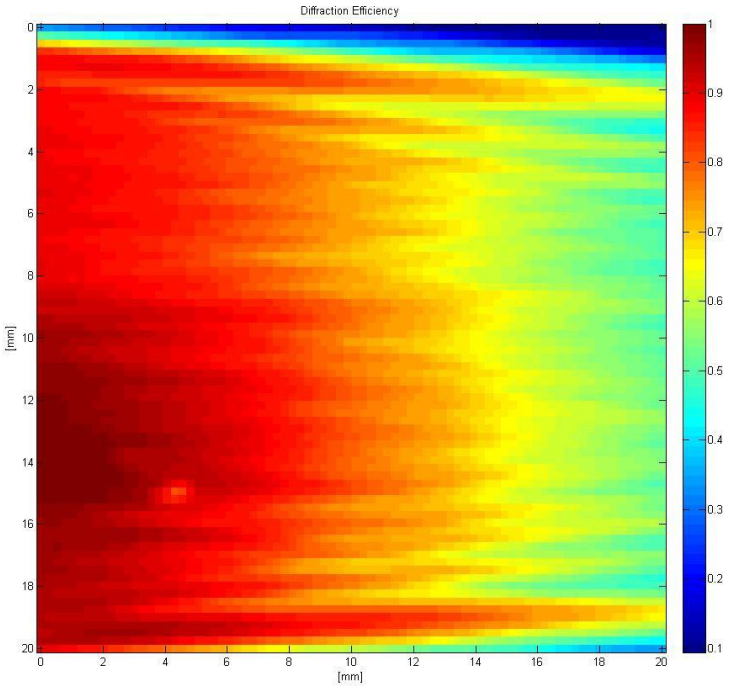

Figure 8.6: Measurement of the diffraction efficiency across the active aperture of the AOTF at $\lambda = 473$ nm.

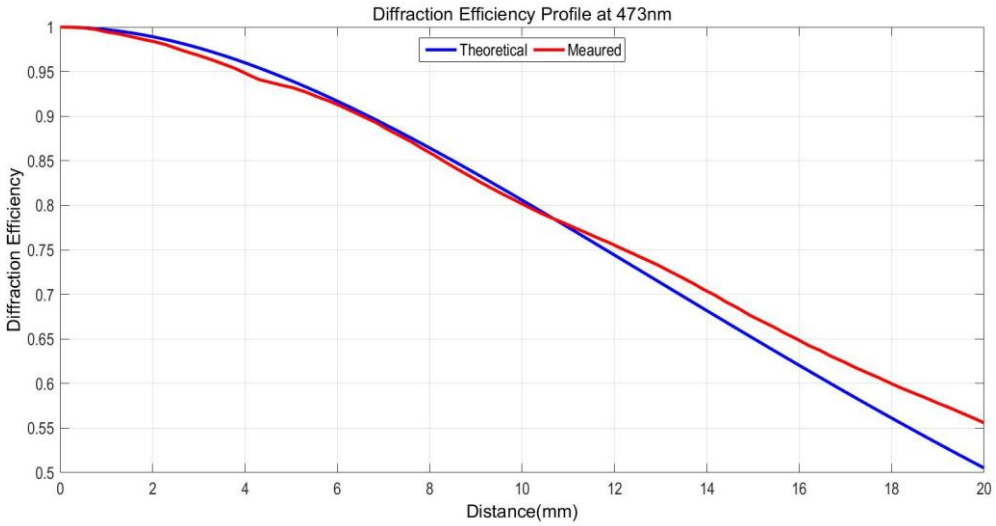

Figure 8.7: Normalize diffraction efficiency across the active aperture of the AOTF.

reduced dynamic range of the system. The AOTF enables capture of a data cube of a sample scanning the RF frequency, where each pixel has the spectral information of each wavelength. For each wavelength the correct RF power has to be selected in order

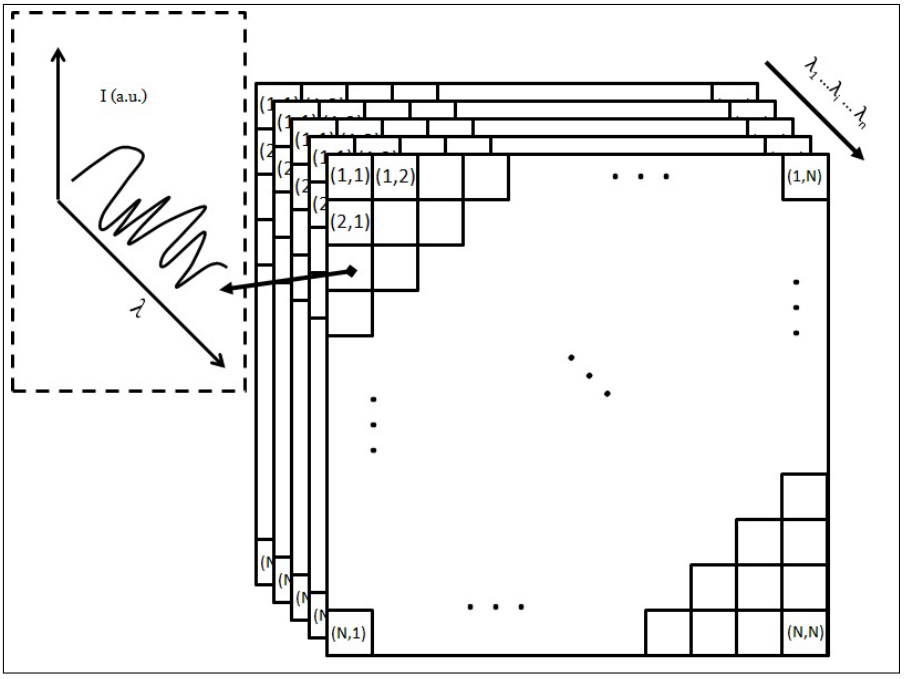

Figure 8.8: Reflectivity of the sample for a given wavelength.

to maximize the diffraction efficiency, and achieve the best SNR by the system, but the acoustic attenuation will limit the performance of the system.

The ideal performance of an imaging system has been simulated using a generic sample randomly generated by a Matlab routine, where the performance is not affected by the optical components before and after the AOTF, and by the lens of the camera.

The generated sample is composed by a random distribution of particles which reflects an incident light with a Gaussian profile perpendicular to the plane. The position and the scattered intensity are generated by a random function, and an example is shown Fig.8.9 for a given wavelength.

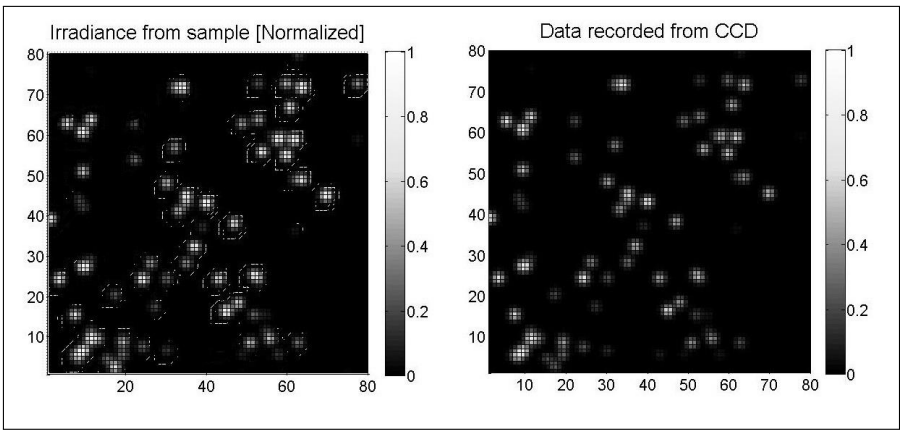

Figure 8.9: Reflectivity of the sample for a given wavelength.

If the peak diffraction efficiency is set to a region close to the transducer area, then the intensity of the first order is not constant as shown in Fig.8.6. Considering a wavelength equal to 473 nm, then it is possible to use the diffraction efficiency shown in Fig.8.6 to estimate the effect of the acoustic attenuation on the system performance. The intensity recorded by the CCD camera is the radiance of the sample multiplied by the diffraction efficiency across the aperture, assuming no degradation from the optical system. Fig.8.9 shows the data recorded of the sample by an ideal CCD matrix. The variation of the diffraction efficiency across the aperture leads to a reduction of the dynamic range especially at the far end of the optical aperture, because the luminosity of the sample subtracted from the information obtained from the CCD camera shows a discrepancy on the intensity profile, which is highlighted in Fig.8.10.

Part of the information for $X > 10$ mm is lost, leading to a wrong assessment of the sample radiance. If the RF power is set to achieve peak diffraction efficiency at the centre of the active aperture, then the RF power in the region close to the transducer is too high, and the diffraction efficiency and passband are both affected.

The diffraction efficiency across an aperture of 20.0 mm has been estimate theoretically for three different region: one close to the transducer (Fig.8.11(a)), one in the centre of the active area (Fig.8.11(b)), and one close to the end of the active area (Fig.8.11(c)) by mean of Matlab routine developed by the author. This routine could be used to estimate the performance of an arbitrary AOTF configuration for any wavelength. The variation of the diffraction efficiency across the aperture is more severe at short wavelengths, which is expected due to the high frequencies involved, thus the imaging system performance is relatively unaffected for wavelength above 700 nm.

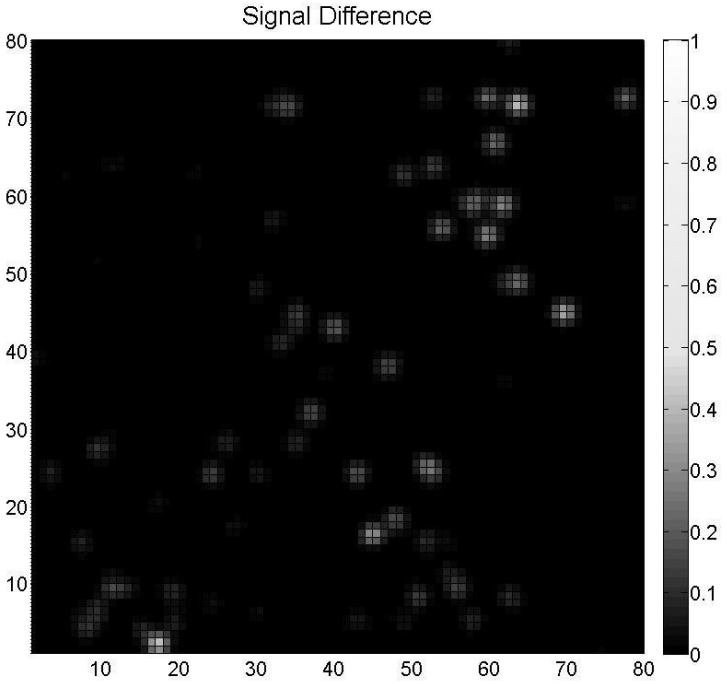

Figure 8.10: Difference between the recorded signal by the CCD camera and the radiance from the simulated sample.

8.5.1 Proposed solution

A technique to increase the signal to noise ratio when the RF power is not optimized to achieve peak diffraction efficiency is proposed. The CCD matrix is vertically segmented in to an arbitrary number of sub-matrix, then the RF power is set to achieve peak diffraction efficiency in the centre of each region and only the ”optimized” information is stored.

A diagram of the configuration proposed is shown in Fig.8.12, where the CCD matrix is split in to 2 region and the RF power level is set to achieve peak diffraction efficiency on each section for a given wavelength, this information is obtained from the mathematical simulation and corrected with a calibration procedure, which is stored inside the controller (e.g. by means of look-ups table). Two set of data are to be recorded for each wavelength, the first set corresponding to the first section where the RF power is set to achieve diffraction efficiency at the centre. The other set corresponds to the data in the second section where the RF power is set to higher level in order to compensate the acoustic attenuation and achieve peak diffraction efficiency in the centre of the region of interest.

In the post process operations the two data set are merged together, where the area with non optimal configuration is not stored. The merging operation is obtained using

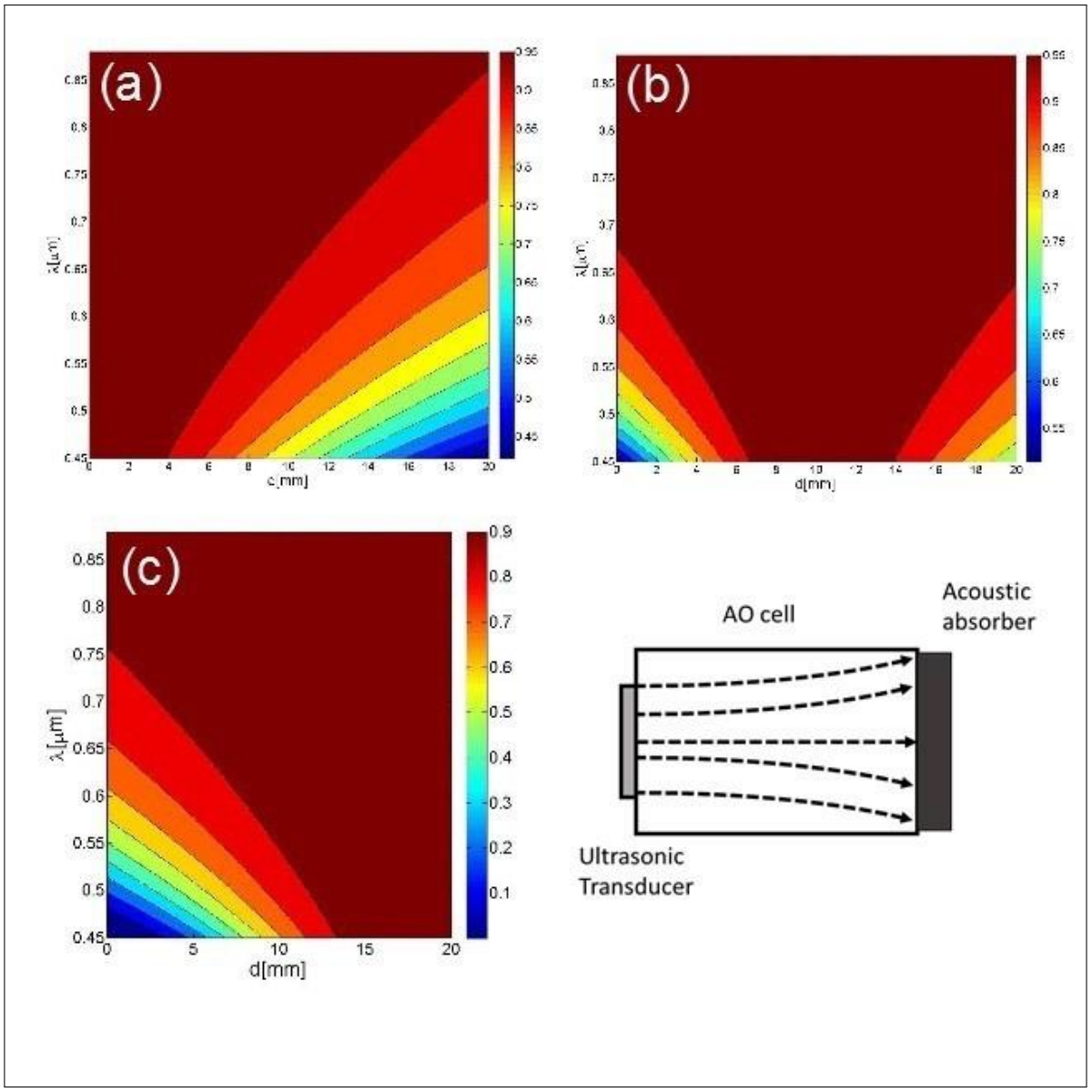

Figure 8.11: Diffraction efficiency across the aperture for the wavelength range between 450 nm and 900 nm with RF power optimized in the region close to the transducer (a), in the centre of the optical aperture (b), and in the opposite region of the transducer (c).

simple data analysis software or python routine, which convert the information from the CCD camera into matrix form.

8.5.2 Scanning time consideration

The performance improvement is obtained at the expense of the scanning time, which increases with the number of sections. For this reason segmenting the CCD camera in more than two sections, will increase drastically the scanning time to record the data

cube, which is determined by several factors such as: frame rate of the camera and its data transfer, the time required to merge the two sets of data, RF driver speed on adjusting the RF power and frequency to correct values, also the switching time dictate by the AOTF.

The AOTF switching time is determined by the time required by the acoustic wave to cross the active aperture (20 mm), which for the AOTF being examined is approximately equal to 29 μs. The total scan time is determined by the number of point in the wavelength range of interest. The data cube is formed by 200 scans for a wavelength range between $\lambda_{min} = 450$ nm and $\lambda_{max} = 850$ nm with a step of 2 nm, thus the total time to record the full scan is equal to 5.8 ms, which is twice the case of set-up in Fig.8.12. The maximum frame rate of a conventional CCD camera with 8 mega-pixels of resolution is 17.1 fps, thus two frame will take 116 ms to be stored, which for 200 scans required will require a total time of approximate 24 s. In conclusion the total time required to create a data cube 3296 × 2472 × 200 will be approximately equal to 26 s considering the additional delay from the electronic side. The limitation, in this case, is the camera speed, fast CCD camera are commercially available, with a typical resolution of 640px × 480px and a frame rates of about 200 fps, reducing the time for single frame to approximately 5 ms, therefore the total time for complete scan could be reduced to ~1.2 s,if additional delays are not introduced by the computational process of merging the two data sets.

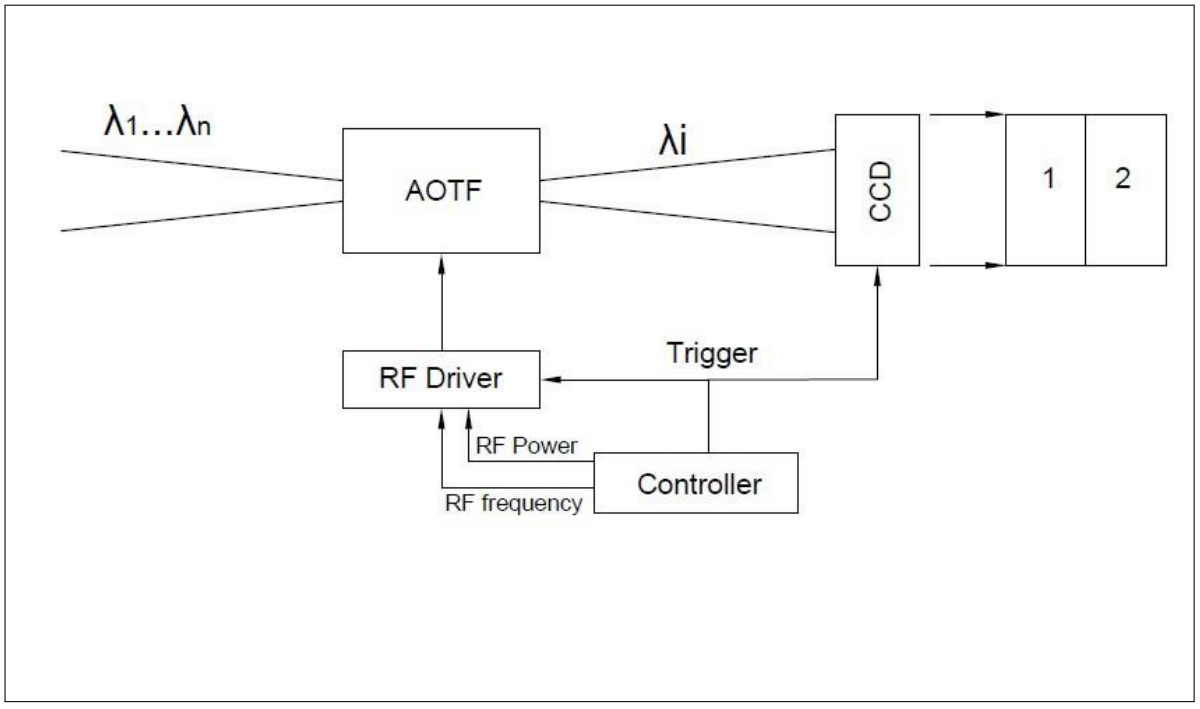

Figure 8.12: Schematic of a confocal system implementing an AOTF as tunable filter element.

8.6 Conclusion

The performance of an AOTF for imaging application with large aperture ($> 15.0mm$) has been examined. The diffraction efficiency across the active aperture is not constant as predicted from the mathematical model and confirmed by experimental results. This effect is due to the acoustic attenuation, which depends on the square of the RF signal. In tellurium dioxide, the wavelength range where this effects is more visible is between 450 nm and 650 nm, due to high frequency required to satisfy the phase matching condition.

Reduction of the diffraction efficiency across the aperture affects the performance of imaging systems especially in confocal systems. In order to obtain a more homogeneous diffraction efficiency across the aperture, the CCD camera is vertically sectioned and two data set are recorded with RF power level set to achieve peak diffraction efficiency at the centre of each section. The two data sets are then merged in to one where only the correct information is stored. The proposed solution is to increase the signal to noise ratio but at the expenses of scanning time, which will increase with the number of section created in the CCD matrix. Experimental results shows that is possible to optimize the imaging system performance segmenting the CCD into two sections, a greater number will increase drastically the scanning time without an actual improve on the system. In the case of smaller aperture ($< 10.0mm$) the diffraction efficiency across the aperture does not change significantly, and good practice is to set the RF power to achieve peak diffraction efficiency in the centre of the active area.

In conclusion, imaging system performance when implementing a large aperture AOTF in telecentric configuration is limited by the acoustic attenuation, so that the diffraction efficiency is not constant across the aperture for frequencies above 100MHz. In order to have a more homogeneous diffraction efficiency across the aperture, it is possible to vertically segment the CCD camera and store the part of the data with the optimal diffraction efficiency selecting the correct RF power, which is confirmed by theoretical model developed to estimate the performance of AOTF in imaging systems.

Chapter 9

Conclusions

The study of high efficiency AOTF was the topic of this dissertation, where different aspects were investigated. The wavelength range from the UV up to MIR has been explored and AOTFs based on different crystals were designed. The use of resonant acoustic cavities was introduced when the RF power to achieve peak diffraction efficiency was exceeding 5 W. This arbitrary limits was introduced to reduce detrimental thermal effects affecting the performances of AOTFs, because all crystal properties are temperature dependent and of difficult prediction, especially in the case of inhomogeneous temperature rises, the result is a device having poor performance.

Tellurium dioxide was firstly studied because it is most common material used in AOTF in the wavelength range between 380 nm and 4.5 μm. The industrial processes of polishing and bonding is well established in Gooch & Housego Ltd. (UK), allowing to obtain high accuracy on each step. One of the limitation encountered in TeO_2 is the RF power to achieve peak diffraction efficiency in case of non-collinear AOTF in parallel tangent matching condition which is above 5 W for $\lambda > 2$ μm. The use of acoustic resonant cavities in AOTFs allow to reduce the RF power required to achieve peak diffraction efficiency and it has been demonstrated that the advantage factor achieved in TeO_2 is about 5 times. The presence of travelling in both direction has two effects on the devices performance: first is the non-continuity of the tuning range because the device is in resonance only for specific frequency, second is the requirement of specialised RF driver to track the resonant frequencies.

The concept of acoustic resonant device are reported briefly in literature by Chang, the solution proposed to lock te device was to reduce the temperature down in order to stabilize the device. An opposite solution was proposed in this thesis, where the device is heat up in order to achieve thermal stabilization, experimentally this approach show the possibility to actively lock the device. The advantage factors achieved in TeO_2 was

about 5. Two prototypes were built in order to verify the accuracy of the mathematical model developed, the first prototype operating in the wavelength range between 1 μm and 2 μm, and the second prototype instead was designed to work between 2.5 μm and 4.5μm. Both prototypes demonstrated the accuracy of the mathematical model was below 0.5 %.

The investigation for AOTF in the wavelength between 4.5μm and 10 μm was carried over thank to MINERVA Project (FP-7) using calomel single crystal. Several challenges were faced in the design and production process, mainly due to the limited acousto-optic figure of merit and to the physical properties, which are not suitable for conventional manufacturing processes. A technique was proposed to use a buffer material, where conventional bonding process could be used, and to bond with glue to the AO cell. The identification of the buffer material and the proper glue to be used in the bonding technique allowed to excite slow shear waves inside the AO cell. The buffer material identified was TeO_2 and the glue was araldite 2020. A non collinear AOTF made of Calomel single crystal showed the possibility to build a functional device with low efficiency due to the bonding process which was on a preliminary stage. It has to be pointed out that even improving the bonding process it is not possible to optimize a design because the limited M_2 will lead to high RF power for wavelength above 4 μm and the use of resonant cavities is not a feasible solution since no feedback signal is obtained at transducer level. Another limiting factors is the modest birefringence leading to RF frequency too low to use a conventional ultrasonic transducer made of $LiNbO_3$.

Other crystals can be used to build AOTF in the wavelength range between 4.5 μm and 10 μm, single crystal tellurium shows interesting performance thanks to elevated M_2 and large birefringence [47]. Some technical challenges has to be solved such as the bonding technique and the large optical activity of the crystal. Another issue is the crystal supplier, which are the moment are mainly university driven and with small quantity. The technology to grow single crystal tellurium is not too different from growing TeO_2 , and the production of single crystal tellurium can start in a year according the Gooch and Housego's crystal grower.

The UV range below 450 nm was investigated in order to realize an AOTF, to possible candidate were considered KDP and Crystal Quartz. The former showed promising performance in resonant configuration due to the low acoustic attenuation leading to a high advantage factor. Due to the low crystal symmetry, one of the problem encountered was the correct orientation of crystal quartz, a technique was devised using a specific piezoelectric plane (AT plane) to identify the correct quadrant inside crystal quartz when using slow shear acoustic waves. Acoustic experiments demonstrated the correctness of this technique. Two different prototypes of non-collinear AOTF were

designed and build one conventional, and one resonant in order to compare the performances and the measure the advantage factors experimentally. Theoretically the advantage factors was expected to be about 11, but the acoustic divergence and optical activity of the crystal, which are not considered in the design routing developed in Matlab by the author, affected the accuracy of the prediction leading to an advantage factor of about 6-7. Crystal quartz has very good thermal properties therefore the lock-in process did not require any active components, and only a software controlling the driver can be used to drive this device.

The dual polarization interaction under the parallel tangent matching condition has been investigated to develop an AOTF to be used in an optical spectrum analyser based on acousto-optic technology. The aim of the study was to develop an OSA in the wavelength range between 2.5 μm and 4.5 μm with a price below £ 5000. The configuration requires a low θ_i leading to a large angle of the acoustic walk-off, consequently the crystal dimension is large and most of the materials is to used for the AO interaction. A solution to reduce the dimension of the crystal was proposed where acoustic waves are reflected in order to increase the interaction length and reduce the crystal dimension, leading to a more efficient use of the crystal volume. The prototype showed good agreement in the tuning range, but the performance were below the prediction, the issue was the phase relation between the different acoustic columns. A solution to optimize this device is to have a phase control feedback system allowing to control the phase of the different acoustic reflections. The last chapter was dedicated to the effects of the acoustic attenuation on larger aperture imaging AOTF, the experimental results show good agreement with the model developed. The results obtained show that particular attention has to be paid when using AOTF with optical aperture larger than 10 mm along the acoustic direction. The effect of the acoustic attenuation affects the performance of the system especially on the pass band which changes with position, in order to correct the error introduced a solution is proposed at the end of the chapter. In conclusion the AOTF performance were improved by different techniques: resonant cavities, and acoustic reflections. The most effective enhancement was achieved by means of acoustic resonant cavities, but this solution can be applied on both type of AOTF: quasi-collinear and non-collinear configuration. A special case where acoustic resonant cavities cannot be applied is the dual polarization AOTF due to the AO cell configuration. In theses years of research activity on AOTF only some the possible AO materials were explored mainly due to their availability, additional research activities can be carried over to increase the understanding of well-known AO material such as single crystal Tellurium. Another research path is development of "smart" driver to optimize the control of the resonant AOTFs, and some example have been reported in the thesis. The research activities of AOTF is far to be exhausted and new efforts to

develop new devices for spectral imaging system and other applications where a fast random access wavelength filter is the best choice.

Appendix A

Sellmeier constant values for AO material

In this section are reported the values used Sellmeier equation constant used on the AO material in exam in Sec.2.4-2.6.

	Ordinary	Extraordinary
A	1.28604141	1.28851804
B	1.07044083	1.09509924
C	1.00585997E-2	1.02101864E-2
D	1.10202242	1.15662475
E	100	100

Table A.1: Constant values used in the Sellmeier's equation for crystal quartz.

A	4.47442	4.7163	4.7363	4.7762	3.71789	2.5848
B	0.1234	0.1350	0.1257	0.1130	0.19619	0.1342
C	0.05814	0.04839	0.05653	0.06482	0.07544	1.1568
D	0	0	0	0.01692	4.61169	0.2638
REF	[REF1]	[REF2]	[REF3]	[REF4]	[REF5]	[REF6]
REF	[14]	[48]	[15]	[15]	[16]	[16]
Eq.	(2.16)	(2.16)	(2.16)	(2.16)	(2.17)	(2.17)

Table A.2: Oscillator values for the ordinary refractive index in TeO_2

A	5.3678	5.331	5.3580	5.4013	4.33449	2.82338
B	0.1358	0.1683	0.1567	0.1430	0.02424	0.1342
C	0.05938	0.04952	0.05774	0.06484	0.14739	1.5402
D	0	0	0	0.02035	4.93667	0.2638
REF	[REF1]	[REF2]	[REF3]	[REF4]	[REF5]	[REF6]
REF	[14]	[48]	[15]	[15]	[16]	[16]
Eq.	(2.16)	(2.16)	(2.16)	(2.16)	(2.17)	(2.17)

Table A.3: Oscillator values for the extraordinary refractive index in TeO_2

A.1 Coordinates transformation

The coordinate transformation is obtained by $M_{x,y,z}$. In this case only two transformations are required: the rotation about the Y and Z axis. The rotation about X is

obtained by:

$$M_x = \begin{bmatrix} 1 & 0 & 0 & 0 & 0 & 0 \\ 0 & \cos(\psi)^2 & \sin(\psi)^2 & \sin(2\psi) & 0 & 0 \\ 0 & \sin(\psi)^2 & \cos(\psi)^2 & -\sin(2\psi) & 0 & 0 \\ 0 & -\frac{\sin(2\psi)}{2} & \frac{\sin(2\psi)}{2} & \cos(2\psi) & 0 & 0 \\ 0 & 0 & 0 & 0 & \cos(\psi) & -\sin(\psi) \\ 0 & 0 & 0 & 0 & \sin(\psi) & \cos(\psi) \end{bmatrix} \quad \text{(A.1)}$$

where ψ is the rotation angle with the X axis as a pivot.

The rotation about Y is obtained by:

$$M_y = \begin{bmatrix} \cos(\phi)^2 & 0 & \sin(\phi)^2 & 0 & -\sin(2\phi) & 0 \\ 0 & 1 & 0 & 0 & 0 & 0 \\ \sin(\phi)^2 & 0 & \cos(\phi)^2 & 0 & \sin(2\phi) & 0 \\ 0 & 0 & 0 & \cos(\phi) & 0 & \sin(\phi) \\ \frac{\sin(2\phi)}{2} & 0 & -\frac{\sin(2\phi)}{2} & 0 & \cos(2\phi) & 0 \\ 0 & 0 & 0 & -\sin(\phi) & 0 & \cos(\phi) \end{bmatrix} \quad \text{(A.2)}$$

where ϕ is the rotation angle with the Y axis as a pivot.

The Rotation about Z[001] is obtained by

$$M_z = \begin{bmatrix} \cos(\theta)^2 & \sin(\theta)^2 & 0 & 0 & 0 & \sin(2\theta) \\ \sin(\theta)^2 & \cos(\theta)^2 & 0 & 0 & 0 & -\sin(2\theta) \\ 0 & 0 & 1 & 0 & 0 & 0 \\ 0 & 0 & 0 & \cos(\theta) & -\sin(\theta) & 0 \\ 0 & 0 & 0 & \sin(\theta) & \cos(\theta) & 0 \\ -\frac{\sin(2\theta)}{2} & \frac{\sin(2\theta)}{2} & 0 & 0 & 0 & \cos(2t) \end{bmatrix} \quad \text{(A.3)}$$

where θ is the rotation angle with the Z axis as a pivot.

Appendix B

Solving the Christoffel's equation with Matlab and Python

The solution of the Christoffel's equation is cumbersome especially when the analytical solution applied to a general direction in the plane of the acousto-optic interaction. Hence the eigenvalues and correspondent eigenvectors of Eq.3.1 are obtained with the help of computer routines developed in Matlab and Python, which solve the system for any acoustic direction. Each acoustic mode is identified by a specific eigenvectors, therefore each solution should track the correct acoustic mode, therefore particular attention has to be paid when using mathematical solver to solve Eq.3.1.

This problem has been partially solved sorting the eigenvector by magnitude and adding an degeneracy detector, which swap the eigenvalues when they cross. A more elegant solution developed to study the acoustic waves in anisotropic materials is to calculate with the help of a symbolic calculus software the expression of $[\Gamma_{ij} - \rho V^2 \delta_{ij}]$ of Eq.3.1 and expressed as

$$\begin{bmatrix} A-\rho V^2 & \sigma_1 & \sigma_3 \\ \sigma_1 & B-\rho V^2 & \sigma_2 \\ \sigma_3 & \sigma_2 & C-\rho V^2 \end{bmatrix} \begin{bmatrix} v_i \\ v_j \\ v_k \end{bmatrix} = 0 \qquad \text{(B.1)}$$

where σ_1, σ_2, σ_3, A, B, C are material and orientation dependent, and $v_{i,j,k}$ is relative to the reference axes system.

Particular attention has to be paid in case of degeneracy of the phase velocity, which is typically present in many-fold symmetric crystals, because the eigenvalues are sorted by magnitude, thus the acoustic mode is not correctly tracked by the solver. For example in trigonal system two of the acoustic modes are degenerate and crosses each other,

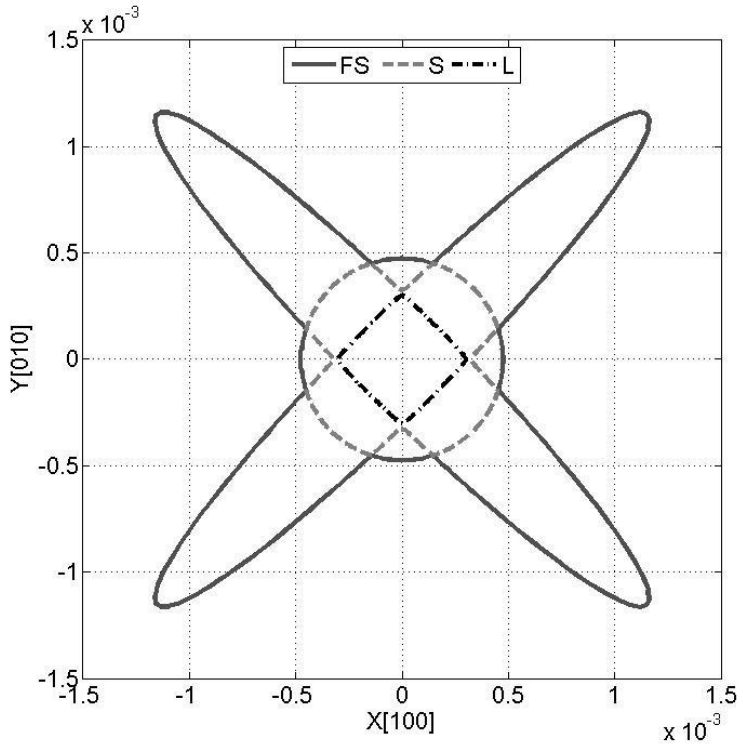

Figure B.1: Slowness curve of the three acoustic wave mode in TeO_2 in [100]-[010] plane.

thus the first eigenvalue does not correspond to the slow shear mode in any direction, this could lead to gross error during the design process. The same problem occurs in case of tetragonal system, but in this case the degeneracy in the typical plane of the AO interaction occurs along the optical axis, where the two shear modes cross in the same point, but in the XY plane the crossing point occurs in different position.

Appendix C

Slow Shear Transducer

Historically piezoelectric transducer were realized using crystal Quartz, but now the common material of choice for AO application is Lithium Niobate ($LiNbO_3$) due its properties. In order to excite a pure acoustic mode particular cut of the crystal are used: for longitudinal wave is used 36° Y-cut, and for shear modes two possible cut could be used one is 163° Y-cut and one is 41° X cut.[6]

The two slow shear cut are characterized by similar properties from the point of view of the piezoelectric effects. In case of the Y-cut the rotation selected is 163°-Y because the polarization direction of the acoustic wave is close to one of the main axis and no longitudinal is excited inside the crystal. The electro-mechanical coupling is equal to 0.61 and a longitudinal component equal to 0.0015, the velocity of the acoustic wave inside the transducer is equal to 4528 m/s. In case of the 41X-cut the electromechanical coupling of the mode is equal to 0.6837 and 0.0984 for the shear and longitudinal mode respectively, where the acoustic velocity is equal to 4079 m/s for the shear mode.

The direction of the polarization of the slow shear acoustic wave is perpendicular to the plane in case of the tZ plane in TeO_2 [1], therefore the slow shear wave is excited efficiently inside the AO crystal when the eigenvector of the shear mode inside the transducer matches the eigenvector of the slow shear inside the AO crystal. In Fig.C.1 the dotted arrows show the direction of the eigenvectors inside the AO crystal, and the solid lines is the polarization of the shear wave inside the ultrasonic transducer. If the eigenvectors direction is not matched then the acoustic mode is not excited efficiently and spurious acoustic mode could be generated inside the AO crystal. The presence of spurious acoustic wave generates unwanted effects which affects the signal to noise ratio. A more detailed analysis is reported in the appendix. The ultrasonic transducer is bonded to the AO crystal by means of standard bonding technique with interlayer

[1] Refer to the previous section

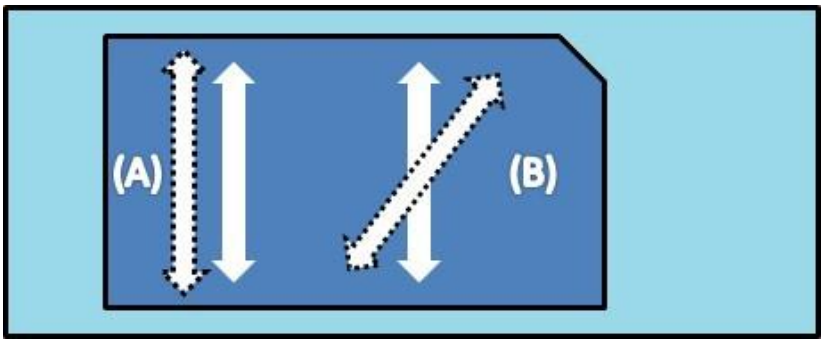

Figure C.1: Diagram of the a shear transducer bonded to an AO crystal, with perfect matching of the acoustic mode (A), when the eigenvectors not match (B)

of indium-gold and high pressure. The thickness of the bond layer is important when designed AOTF, the thickness depends on the centre RF frequency of the device and it is of major importance during the electrical matching process, which is explained in details in the following chapter.

Appendix D

Industrial and design procedure

AOTFs described in this thesis are designed using routine developed by the author using Matlab and Python. Once the AO material has been identified then the routines to study the acoustic property of the material are used in order to determine the plane where the AO interaction takes place, verifying the polarization direction of the acoustic waves taking in account the symmetry of the material. Once the AO interaction plane is identified, another routine is used to determine the geometry of the AO interaction defining the wavelength range, the acoustic direction or the electromagnetic wave propagation of the input and introducing constrain to the AO interaction like parallel tangent matching condition or quasi-collinear interaction. In general the RF power versus diffraction efficiency and the RF frequency range are the properties, which need to considered carefully, in case of broad band matching the frequency range is determine by the centre frequency of the ultrasonic transducer. In general the transducer cannot matched over an octave without practical complication and the matching is less critical for low frequency ($< 80MHz$).

Once the optimised AO interaction has been identified the cell dimension is minimised using a CAD software (such as DrafSight or AutoCAD). From the optimized cell design three different drawings are produced identified by internal codes: the polishing drawing (GH15), the bonding drawing (GH16) and final cell(GH19). The GH19 drawing is then introduced inside 3D model software (e.g. SolidWorks) to generate the three dimensional model used to design the housing and additional metalworks to mount the device, and also in some case the PCB for the matching networks.

Once all the required drawing are generated, a BOM structure is created where the components and industrial process are introduced and all the additional information required are inserted in order to produce a job card, which is required in the production site to create the device. Before the job card could be raised,it is required to obtain

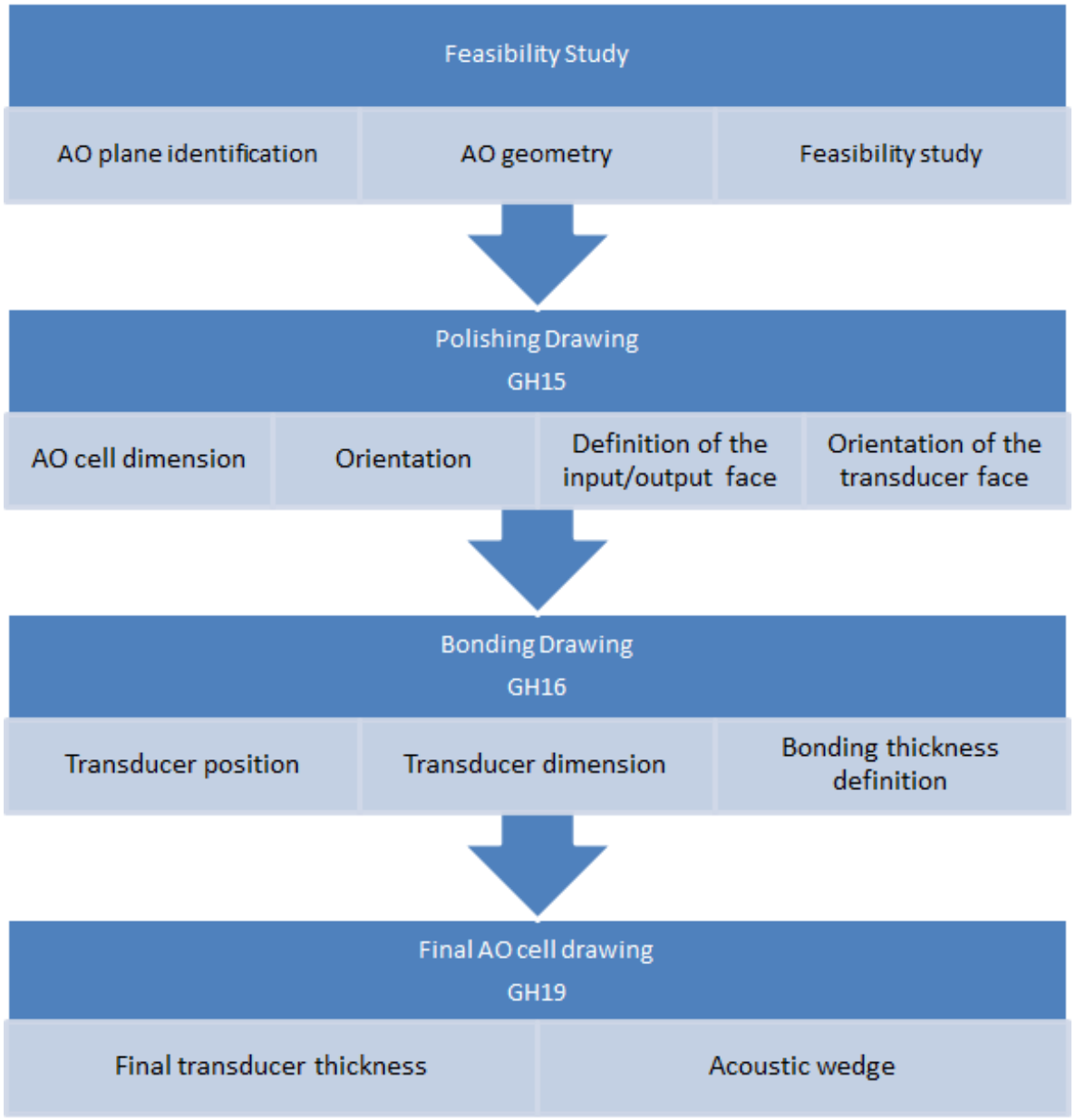

Figure D.1: FLowchart of the industrial and design procedure.

the approval from the different supervisor of each area where the device is worked in order to receive the feedback on the process described on the job cards.This procedure is applied to any devices built in the factory from the prototypes to the commercial devices.

Once the AO cell of the prototypes is completed, then the device is RF matched and tested inside the R&D laboratory, using the laser line test and white light test, and an automatic is generated by the control software.

Appendix E

Derivation of the acoustic attenuation in anisotropic material

The acoustic attenuation depends on the direction of propagation, an expression has been determined for tetragonal and trigonal crystal class. If the acoustic attenuation is defined as:

$$\alpha_{ij} = \frac{\omega^2}{2}\sqrt{\frac{\rho}{c_{ij}}}\,\eta_{ij} \tag{E.1}$$

where $\omega = 2\pi f$, ρ is the density of material, c_{ij} is the elastic stiffness constant of the material, and η_{ij} is the viscosity of the material.

The acoustic velocity $V_{ij} = \rho/c_{ij}$ then it is possible to write the expression of the acoustic velocity in TeO_2 in the t-Z plane:

$$V(\theta_a) = \frac{\sqrt{c_{44}^2\cos^2\theta_a + c_{66}'\sin^2\theta_a}}{\rho} \tag{E.2}$$

the viscosity of the material similarly could be expressed as:

$$\eta(\theta_a) = \sqrt{\eta_{44}^2\cos^2\theta_a + \eta_{66}'\sin^2\theta_a} \tag{E.3}$$

The acoustic attenuation can be written as:

$$\alpha(\theta_a) = \frac{\omega^2\,\rho^2}{2\,V^3}\sqrt{\eta_{44}^2\cos^2\theta_a + \eta_{66}'\sin^2\theta_a} \tag{E.4}$$

The acoustic attenuation is known for specific direction therefore it is useful to define $\alpha(\theta_a)$ for $\theta_a = 0$

$$\alpha_{[110]} = \frac{\omega^2 \ \rho^2}{2 \ V_{110}^3} \eta_{66} \tag{E.5}$$

and for $\theta_a = \pi/2$

$$\alpha_{[001]} = \frac{\omega^2 \ \rho^2}{2 \ V_{001}^3} \eta_{44} \tag{E.6}$$

Introducing in Eq.E.4 the expression of Eq.E.5 - Eq.E.6 it is obtained

$$\alpha(\theta_a) = \sqrt{\alpha_{001}^2 \cos^2\theta_a + \alpha_{110}^2 \sin^2\theta_a} \tag{E.7}$$

for a tetragonal crystal. In case of crystal quartz a similar expression can be obtained by introducing the correct viscosity components and velocity expression.

Appendix F

Phase velocity measurement by means of Pulse Echo RIG

The phase velocity in anisotropic material can be measured by different means, one of the most efficient in sample where a bonded ultrasonic transducer is used to generate elastic waves, is the pulse-echo measurement. The set-up is shown in Fig.F.1, where the ultrasonic transducer is used as source and receiver. In this experiment is only possible to detect the acoustic mode where the piezoelectric effect is maximize, which correspond to the acoustic mode excited by the ultrasonic transducer when used as a generator.

It is possible to measure the time of flight of different acoustic mode if transducer with different orientation are used as source/receiver.

The pulse-echo is realised using an RF signal generator, which is gated by a switch controlled by a pulse generator. After a 20 dB coupler had been added, to measure the reference peak and the RF power used, a second 10 dB coupler is used to collect the feedback signal coming from the device under test, which is connected by a low loss delay line cable long 10 m. The signal obtained by the echo, is coupled in second directional coupler, which is connected to an RF amplifier and a power detector, ultimately connected to a scope.

The RF power detector show a negative peak which is proportional to the RF power measured F.1, no temperature control has been added because it is not the amplitude of the negative peaks but the distance between them, which is relevant in the measurement of the acoustic phase velocity.

The echo is only measured if the active area of the transducer defined by the electrode, therefore the parallelism between opposite faces is of particular importance.

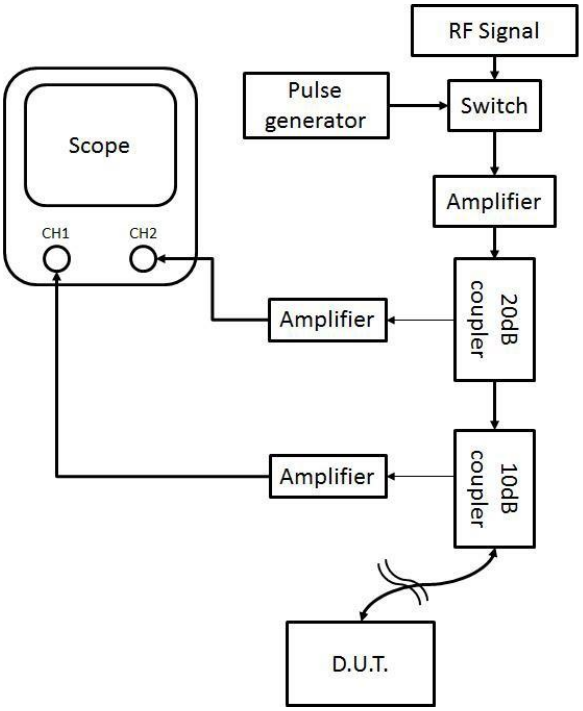

*Figure F.1: Schematic of Pulse-Echoes **RIG** to measure echoes of a resonant cavity.*

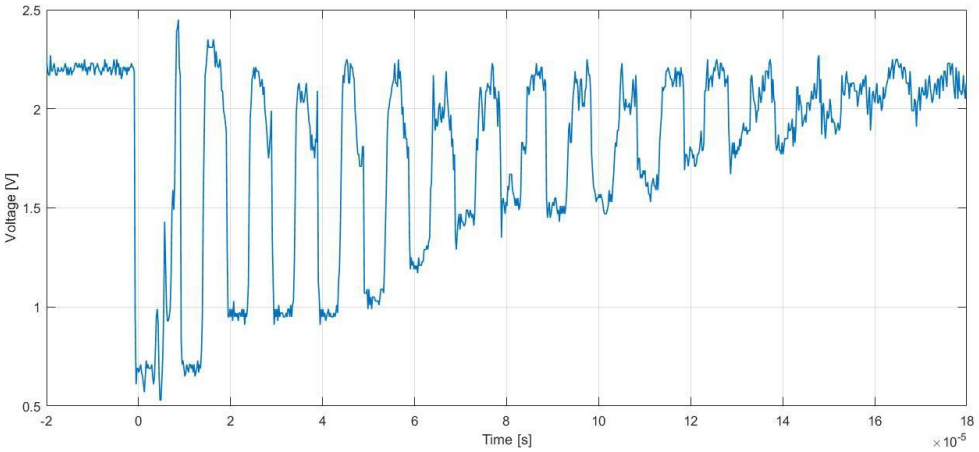

*Figure F.2: Signal obtained by the RF power detector testing the quartz resonant **AOTF**.*

The theoretical phase velocity of the slow shear wave in the TZ plane shows a discrepancy between the values obtained by solving Eq.3.1 introducing the elastic stiffness constant reported by Xu and Stroud in [6] and experimental results. Therefore the acoustic velocities of the slow shear mode in TeO_2 was measured by means of the pulse echo Rig using two samples with different orientation and same thickness were, one with the acoustic propagation along the 110 direction and one along the 001 direction. The experimental results shown a good agreement with the acoustic velocity along the $< 001 >$ direction, which is equal to 2104.0 ± 0.5 [m/s]. The slow shear velocity is instead equal to 616 ± 1 [m/s], which close to the value conventionally used in Eq.3.30 which is 616 [m/s].

Appendix G

AOTF Testing RIG

G.1 Laser line test

The diffraction efficiency versus RF power for a given wavelength is measured by means of a standard laser line test, which consists of a laser source, RF synthesizer, RF power meter, and lock-in amplifier. The AOTF is aligned in order to achieve peak diffraction efficiency for both wavelength using the lock-in amplifier with a sensor mounted on an integrating sphere (Fig.G.1).

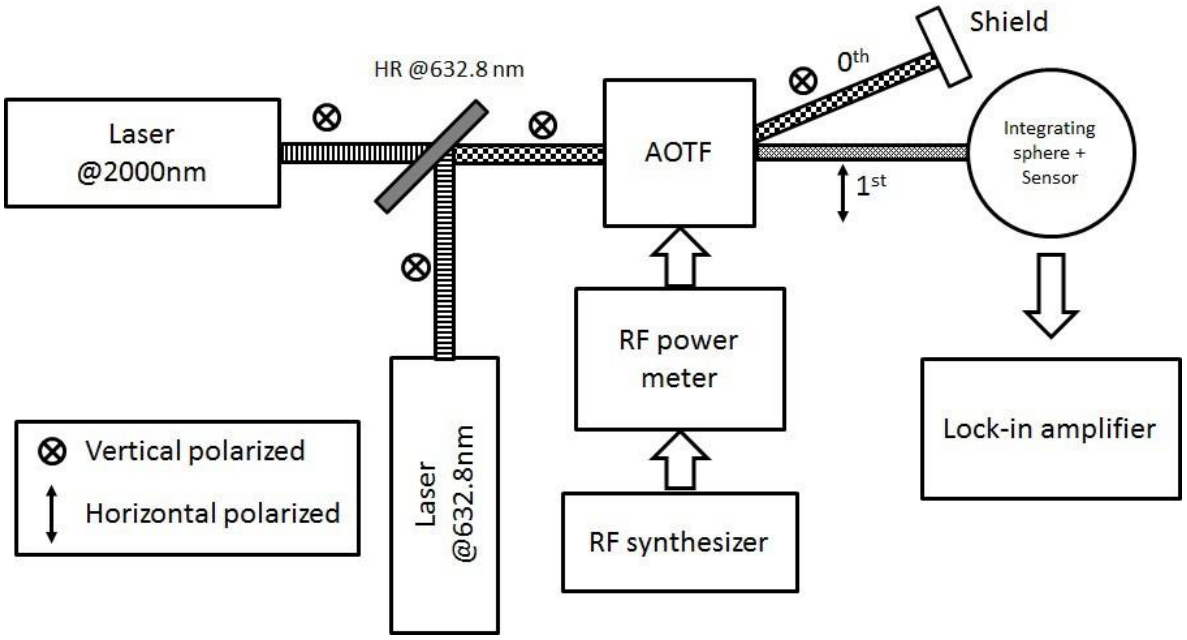

Figure G.1: Laser line test setup to measure diffraction efficiency versus RF power.

The two lasers used are an HeNe at 632.8 nm and diode laser fibre coupled at 2000

nm, both vertically polarized corresponding to ordinary ray for AOTF cells. A dichroic mirror is used to superimpose both lasers onto the same path,so they enter the crystal at the same point and at the same θ_i. Other laser are used in place of the 2000 nm source depending on the wavelength determined by the frequency range of the AOTF, other sources are He-Ne at 3390 nm and the 1550 nm.
A Labview interface used to control and collect data from the Lock-in amplifier, from the RF power meter, and RF synthesizer.

G.2 White Light test

The tuning relation is measure by means of optical spectrum analysers (OSAs) and a supercontinuum source from Fianium, with a spectrum from 400 nm up to 2000 nm. The system is show in Fig.G.2.

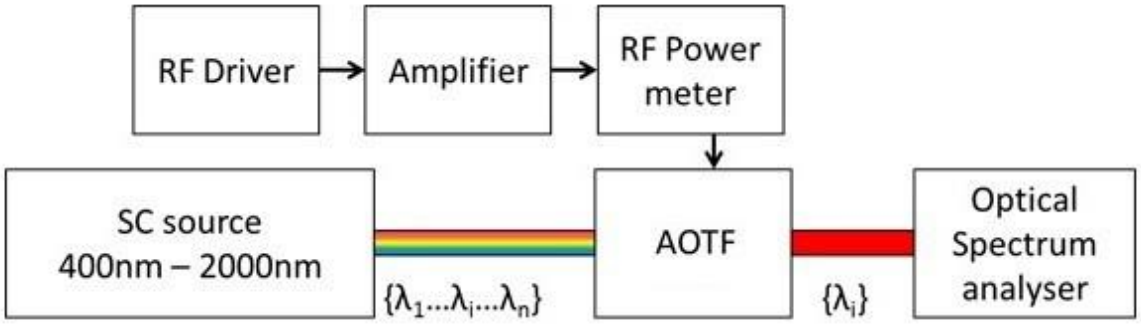

Figure G.2: Laser line test setup to measure diffraction efficiency versus RF power.

A Labview interface to run automatic tests was developed in G&H previously and the author optimized the performance in order to increase its robustness and speed up to 80%.

Appendix H

List of pubblication

Conference pubblication

1. S. Valle, J. Ward, C. Pannell, N. Johnson, Imaging AOTFs with low RF power in deep-UV and Mid-IR, inPhysics Procedia 70 – May 2015, Conference: 2015 International Congress on Ultrasonic, At Metz, France.
   DOI: 10.1016/j.phpro.2015.08.096

2. S. Valle, J. Ward, C. Pannell, N. Johnson, Acousto-optic tunable filter for imaging application with high performance in the IR region inProceedings of SPIE - The International Society for Optical Engineering 9359 – February 2015
   DOI: 10.1117/12.2077610 Conference: SPIE 2015 - Optical Components and Materials XII

3. S. Valle, J. Ward, C. Pannell, N. Johnson, Acousto-Optic Tunable Filters (AOTFs) Optimised for Operation in the 2-4m region inJournal of Physics Conference Series 619(1) – July 2014, Conference: ICOOPMA 2014, At Leeds, Volume: 61
   DOI: 10.1088/1742-6596/619/1/012054

4. S. Valle, J. Ward, C. Pannell, N. Johnson, Mid infra-red hyper-spectral imaging with bright super continuum source and fast acousto-optic tuneable filter for cytological applications inJournal of Physics Conference Series 619(1) Conference: ICOOPMA 2014, At Leeds, Volume: 619 July 2014
   DOI: 10.1088/1742-6596/619/1/012032

5. M. Farries, J. Ward, J. Ward, et al. , Acousto-Optic Tunable Filters for Imaging Applications in the 2-4 m with Low RF Drive PowerinActa Physica Polonica Series a 127(1) – June 2014with23 Reads

DOI: 10.12693/APhysPolA.127.58 Conference: 12th School on Acousto-Optics and Application

6. P. Shardlow, J. Ward, C. Pannell, S. Valle, W. A. Clarkson. Null-frequency-shift acousto-optic tunable filter for wavelength tuning of a Tm fibre laser. ũ June 2015 Conference: CLEO/Europe-EQEC 2015

Patent

1. S. Valle, J. Ward, C. Pannell, Acoustic Absorber having a Roughened Surface for AO Devices Patent ũ April 2016 Patent: US9310631B1

References

[1] Berg NJ, Pellegrino JM, editors. Acousto-optic signal processing: theory and implementation. 2nd ed. No. 51 in Optical engineering. New York: M. Dekker; 1996.

[2] Barta, Trnka J. New Types of Polarizers Made from Crystals of the Calomel Group. Crystal Research and Technology. 1982;17(4):431–438. Available from: http://onlinelibrary.wiley.com/doi/10.1002/crat.2170170407/abstract.

[3] Gupta N. Materials for imaging acousto-optic tunable filters. vol. 9100; 2014. p. 91000C–91000C–10. Available from: http://dx.doi.org/10.1117/12.2054050.

[4] Gupta N, Voloshinov VB, Knyazev GA, Kulakova LA. Optical transmission of single crystal tellurium for application in acousto-optic cells. Journal of Optics. 2011 May;13(5):055702. Available from: http://stacks.iop.org/2040-8986/13/i=5/a=055702?key=crossref.35d6a636d5aad3a04279752524dee6bb.

[5] Gupta N, Voloshinov VB, Knyazev GA, Kulakova LA. Tunable wide-angle acousto-optic filter in single-crystal tellurium. Journal of Optics. 2012 Mar;14(3):035502. Available from: http://stacks.iop.org/2040-8986/14/i=3/a=035502?key=crossref.43960e4ab585a7e79333c7c32c4e9fc8.

[6] Xu J, Stroud R. Acousto-optic devices: principles, design, and applications. Wiley series in pure and applied optics. Wiley; 1992. Available from: http://books.google.co.uk/books?id=DGYbAQAAIAAJ.

[7] Goutzoulis AP, Gottlieb M, Singh NB. Mercurous Chloride Acousto-Optic Bragg Cells: A New Class Of Long Delay Devices. In: OE LASE'87 and EO Imaging Symp (January 1987, Los Angeles). International Society for Optics and Photonics; 1987. p. 29–36. Available from: http://proceedings.spiedigitallibrary.org/proceeding.aspx?articleid=1246979.

[8] Nye JF. Physical properties of crystals: their representation by tensors and matrices. 1st ed. Oxford [Oxfordshire] : New York: Clarendon Press ; Oxford University Press; 1984.

[9] Bagan VA, Davydov BL, Samartsev IE. Characteristics of Cornu depolarisers made from quartz and paratellurite optically active crystals. Quantum Electronics. 2009 Jan;39(1):73–78. Available from: http://stacks.iop.org/1063-7818/39/i=1/a=A13?key=crossref.1e8dc8a22162a4b3964094ea7b78be5d.

[10] Kaminsky W, Hartmann E. Anisotropy of optical activity and Faraday effect in TeO2. Zeitschrift für Physik B Condensed Matter. 1993;90(1):47–50. Available from: http://link.springer.com/article/10.1007/BF01321031.

[11] Simon HJ, Bloembergen N. Second-Harmonic Light Generation in Crystals with Natural Optical Activity. Physical Review. 1968 Jul;171(3):1104–1114. Available from: http://link.aps.org/doi/10.1103/PhysRev.171.1104.

[12] Ghosh G. Dispersion-equation coefficients for the refractive index and birefringence of calcite and quartz crystals. Optics communications. 1999;163(1):95–102. Available from: http://www.sciencedirect.com/science/article/pii/S0030401899000917.

[13] Arteaga O, Canillas A, Jellison GE Jr. Determination of the components of the gyration tensor of quartz by oblique incidence transmission two-modulator generalized ellipsometry. Applied Optics. 2009 Oct;48(28):5307. Available from: http://www.opticsinfobase.org/abstract.cfm?URI=ao-48-28-5307.

[14] Uchida N. Optical Properties of Single-Crystal Paratellurite (Te O 2). Physical Review B. 1971;4(10):3736. Available from: http://journals.aps.org/prb/abstract/10.1103/PhysRevB.4.3736.

[15] Berny JG, Bourgoin JP, Ayrault B. Dispersion des indices de refraction du molybdate de plomb (PbMoO 4) et de la paratellurite (TeO 2). Optics Communications. 1972;6(4):383–387. Available from: http://www.sciencedirect.com/science/article/pii/0030401872901629.

[16] Georgiev G, Glenar DA, Hillman JJ. Spectral characterization of acousto-optic filters used in imaging spectroscopy. Applied optics. 2002;41(1):209–217. Available from: http://www.osapublishing.org/abstract.cfm?uri=ao-41-1-209.

[17] Auld BA. Acoustic fields and waves in solids. ;. Available from: https://books.google.co.uk/books?id=_2MWAwAAQBAJ.

[18] Polikarpova NV, Voloshinov VB. Intensity of reflected acoustic waves in acousto-optic crystal tellurium dioxide; 2005. p. 25–36. Available from: http://proceedings.spiedigitallibrary.org/proceeding.aspx?articleid=1326856.

[19] Uchida N. Acoustic Attenuation in TeO2. Journal of Applied Physics. 1972;43(6):2915. Available from: http://scitation.aip.org/content/aip/journal/jap/43/6/10.1063/1.1661627.

[20] Kim JS, Trivedi SB, Soos J, Gupta N, Palosz W. Development of mercurous halide crystals for acousto-optic devices. vol. 6661; 2007. p. 66610B–66610B–12. Available from: http://dx.doi.org/10.1117/12.734102.

[21] Gass PA, Sambles JR. Accurate design of a noncollinear acousto-optic tunable filter. Optics Letters. 1991 Mar;16(6):429. Available from: http://www.opticsinfobase.org/ol/abstract.cfm?uri=ol-16-6-429.

[22] Chang IC. Tunable Acousto-Optic Filters: An Overview. vol. 0090; 1976. p. 12–22. Available from: http://dx.doi.org/10.1117/12.955046.

[23] Voloshinov VB. Close to collinear acousto-optical interaction in TeO2 single crystal. In: Acousto-optics and Applications. International Society for Optics and Photonics; 1992. p. 162–176. Available from: http://proceedings.spiedigitallibrary.org/proceeding.aspx?articleid=1005022.

[24] Ward J, Farries M, Pannell C, Wachman E. An acousto-optic based hyperspectral imaging camera for security and defence applications; 2010. p. 78350U–78350U–9. Available from: http://proceedings.spiedigitallibrary.org/proceeding.aspx?articleid=1347890.

[25] Chang IC. Noncollinear acousto-optic filter with large angular aperture. Applied Physics Letters. 1974;25(7):370. Available from: http://scitation.aip.org/content/aip/journal/apl/25/7/10.1063/1.1655512.

[26] Dekemper E, Fussen D, Pieroux D, Vanhamel J, Van Opstal B, Vanhellemont F, et al. ALTIUS: a spaceborne AOTF-based UV-VIS-NIR hyperspectral imager for atmospheric remote sensing; 2014. p. 92410L. Available from: http://proceedings.spiedigitallibrary.org/proceeding.aspx?doi=10.1117/12.2063937.

[27] Ward J, Farries M, Pannell C, Wachman E. Acousto-Optic Tunable Filters and Their Applications to Hyperspectral Imaging;.

[28] Valle S, Ward JD, Pannell C, Johnson NP. Acousto-Optic Tunable Filters for Imaging Applications in the 2-4˜m with Low RF Drive Power. Acta Physica Polonica A. 2015 Jan;127(1):58–59. Available from: http://przyrbwn.icm.edu.pl/APP/PDF/127/a127z1p13.pdf.

[29] Ward JD, Valle S, Pannell C, Johnson NP. Acousto-Optic Tunable Filters (AOTFs) Optimised for Operation in the 2-4m region. J Phys: Conf Ser. 2015 Jun;619(1):012054. Available from: http://iopscience.iop.org/1742-6596/619/1/012054.

[30] Keller U, Weingarten KJ, Gerstenberger DC, Li KD, Khuri-Yakub BT, Bloom DM. High-frequency acousto-optic mode locker for picosecond pulse generation. Opt Lett. 1990 Jan;15(1):45–47. Available from: http://ol.osa.org/abstract.cfm?URI=ol-15-1-45.

[31] Hui-juan Dong, Jian Wu, Guang-yu Zhang, Han-fu Wu. An improved phase-locked loop method for automatic resonance frequency tracing based on static capacitance broadband compensation for a high-power ultrasonic transducer. IEEE Transactions on Ultrasonics, Ferroelectrics, and Frequency Control. 2012 Feb;59(2):205–210. Available from: http://ieeexplore.ieee.org/lpdocs/epic03/wrapper.htm?arnumber=6156822.

[32] Ward JD, Pannell CN. Matched Pair of AOTFs with Net Zero Frequency-shift. Physics Procedia. 2015;70:914–917. Available from: http://linkinghub.elsevier.com/retrieve/pii/S187538921500930X.

[33] Lindsay ID, Valle S, Ward J, Stevens G, Farries M, Huot L, et al. Towards supercontinuum-driven hyperspectral microscopy in the mid-infrared; 2016. p. 970304. Available from: http://proceedings.spiedigitallibrary.org/proceeding.aspx?doi=10.1117/12.2210836.

[34] Gupta N. Acousto-optic tunable filters for infrared imaging. vol. 5953; 2005. p. 595300–595300–10. Available from: http://dx.doi.org/10.1117/12.641081.

[35] Knuteson DJ. Crystal growth, fabrication, and design of mercurous bromide acousto-optic tunable filters. Optical Engineering. 2007 Jun;46(6):064001. Available from: http://opticalengineering.spiedigitallibrary.org/article.aspx?doi=10.1117/1.2744369.

[36] Gottlieb M, Goutzoulis AP, Singh NB. Fabrication and characterization of mercurous chloride acoustooptic devices. Applied Optics. 1987 Nov;26(21):4681. Available from: https://www.osapublishing.org/ao/abstract.cfm?uri=ao-26-21-4681.

[37] Gupta N. Investigation of a mercurous chloride acousto-optic cell based on longitudinal acoustic mode. Applied optics. 2009;48(7):C151–C158. Available from: http://www.osapublishing.org/ao/fulltext.cfm?uri=ao-48-7-C151.

[38] Barta, Broek V, others. Properties of Surface Layers in Single Crystals of Calomel. Crystal Research and Technology. 1982;17(4):439–448. Available from: http://onlinelibrary.wiley.com/doi/10.1002/crat.2170170408/abstract.

[39] Gupta N, Dahmani R, Choy S. Acousto-optic tunable filter based visible-to near-infrared spectropolarimetric imager. Optical Engineering. 2002;41(5):1033–1038. Available from: http://opticalengineering.spiedigitallibrary.org/article.aspx?articleid=1098876.

[40] Voloshinov VB. Acousto-optic filters on potassium dihydrogen phosphate with optimal angle aperture and maximum beam deflection. Optical Engineering. 2008 Jul;47(7):073201. Available from: http://opticalengineering.spiedigitallibrary.org/article.aspx?doi=10.1117/1.2955760.

[41] Gupta N, Voloshinov V. Hyperspectral Imager, from Ultraviolet to Visible, with a KDP Acousto-Optic Tunable Filter. Applied Optics. 2004;43(13):2752. Available from: http://www.opticsinfobase.org/abstract.cfm?URI=AO-43-13-2752.

[42] Gupta N. Fiber-coupled AOTF spectrometers; 2006. p. 60830U–60830U–12. Available from: http://proceedings.spiedigitallibrary.org/proceeding.aspx?articleid=1273864.

[43] Gupta N, Voloshinov VB. Development and characterization of two-transducer imaging acousto-optic tunable filters with extended tuning range. Appl Opt. 2007 Mar;46(7):1081–1088. Available from: http://ao.osa.org/abstract.cfm?URI=ao-46-7-1081.

[44] Voloshinov VB, Tchernyatin AY, Blomme E, Leroy OJ. A dozen Bragg effects in tellurium dioxide single crystal. In: Acousto-Optics and Applications III. International Society for Optics and Photonics; 1998. p. 141–152. Available from: http://proceedings.spiedigitallibrary.org/proceeding.aspx?articleid=974771.

[45] Chang IC. Analysis of the noncollinear acousto-optic filter. Electronics Letters. 1975;11(25):617–618. Available from: http://digital-library.theiet.org/content/journals/10.1049/el_19750470.

[46] Uchida N, Ohmachi Y. Elastic and Photoelastic Properties of TeO2 Single Crystal. Journal of Applied Physics. 1969 Nov;40(12):4692–4695. Available from: http://scitation.aip.org/content/aip/journal/jap/40/12/10.1063/1.1657275.

[47] Voloshinov VB, Balakshy VI, Kulakova LA, Gupta N. Acousto-optic properties of tellurium that are useful in anisotropic diffraction. Journal of Optics A: Pure and Applied Optics. 2008 Sep;10(9):095002. Available from: http://stacks.iop.org/1464-4258/10/i=9/a=095002?key=crossref.b578235759b92b44f6db812bdfe179cd.

[48] Singh NB, Gottlieb M, Mazelsky R, Duval WM. The optical quality of mercurous halide crystals. Journal of crystal growth. 1993;128(1):1053–1058. Available from: http://www.sciencedirect.com/science/article/pii/S0022024807800960.